Microseismic observations in the Ceres-Tulbagh aftershock zone, Western Cape, South Africa, and their tectonic implications

Louis Smit

a thesis submitted for the degree of

Master of Science

at the University of Cape Town, Cape Town,

South Africa.

2013

Abstract

South Africa is considered a stable continental region where earthquakes from a tectonic source are usually of small to moderate magnitude. In September 1969 a local magnitude (M_L) 6.3 sinistral strike-slip earthquake occurred near the towns of Ceres and Tulbagh in the Western Cape, South Africa. This is still the largest earthquake in instrumental history in South Africa.

During 2012, a temporary seismic array of 15 surface stations was deployed for a 3 month period in the aftershock zone of the 1969 Ceres earthquake. A total of 168 microseismic events could be located within the boundaries of the array, roughly 30 km x 40 km. Travel times of these events were used for coupled hypocenter-velocity inversion to produce a one dimensional velocity model with station corrections. The hypocenters of recorded events were relocated using the velocity model and local magnitude was empirically derived for all 168 events.

P- and S-wave velocity ranges from 4.9 km/s to 6.4 km/s and 2.8 km/s to 4.7 km/s, respectively, from the surface down to 12 km depth. The magnitude of the microseisms ranges from -2.2 $< M_L <$ 1.6 with a magnitude of completeness of M_c -1.5, and follow a Gutenberg-Richter distribution with a b-value of 0.9. The microseismic events occurred down to a depth of 15 km within a sub-vertical fault zone roughly 4 km wide, striking SE-NW and passing below the towns of Ceres and Tulbagh. Seismic events appear to occur in two clusters ranging from 0 to 5 km and 8 to 12 km depth, respectively, separated by a 4 km along-strike discontinuity in seismic activity.

There is good agreement between the orientations of the strike of the surface trace of the 1969 aftershock plane and the strike of the surface trace of the microseismic plane. Microseismic activity is attributed to the reactivation in basement structures of either the Malmesbury Group, or the Namaqua Natal Metamorphic

complex from far field stress transfer from the Southwest Indian Ridge. It is proposed, albeit on speculation, that the presence of microseismic activity along the vertically oriented fault zone could be the manifestation of an incipient plate boundary formation.

Acknowledgements

I would like to thank the following:

Inkaba yeAfrica for funding for this project and for student funding. The NRF for student funding. Marius Weber and the GFZ in Potsdam, Germany, who hosted me as a visiting scientist for 2 months. The Geophysical Instruments Pool Potsdam (GIPP) for supplying the instruments used during the experiment. Particular thanks to the following people at the GFZ; Jacek Stankiewicz, Ben Braeuer, Christian Haberland, Ariane Sieber, Matthius Wanjek and Bob Trumbull who all helped to make this project possible. All the farmers in the study area who courteously allowed the installation of our equipment on their farms. My supervisor, Åke Fagereng, for countless revisions, comments and advice.

Contents

List of Figures

Chapter 1

Introduction

The aim of this thesis is to investigate the current level of microseismic activity in an intraplate setting known to have exhibited seismic activity in the past. The study area, Ceres, lies within a stable continental region (SCR) (Saunders *et al.*, 2013) thousands of kilometers away from the nearest plate boundary. The Ceres region (Fig. 5.1), located in the Western Cape Province of South Africa, is host to the largest recorded earthquake in instrumental history in South Africa (Green and Bloch, 1971; Singh *et al.*, 2009).

In general, the majority of seismic activity in South Africa is a direct result of deep underground mining in the platinum and gold fields of the North West, Gauteng and Freestate provinces (Saunders, 2005). However, the largest seismic event in recorded history was due to a tectonic source and occurred near the towns of Ceres and Tulbagh in the form of a local magnitude (M_L) 6.3 earthquake on 29 September, 1969 (Green and Bloch, 1971). At this time there were only a few permanent seismic monitoring stations in South Africa. A temporary seismic array was deployed by Green and Bloch (1971) to record the aftershocks of the Ceres earthquake. The hypocenter locations of the aftershocks plotted on a fault plane that did not match to any previously mapped faults and there was no surface rupture during the main shock (Green and Bloch, 1971).

The South African National Seismograph Network (SANSN), operating under the Council for Geoscience (CGS), started permanent monitoring of seismic events shortly after the 1969 Ceres earthquake (Saunders *et al.*, 2008). The network (Fig. 1.1) currently consist of 21

stations consisting of 5 broadband and 16 short period seismometers (Saunders, 2005). One of the stations operated by the SANSN is located in Ceres.

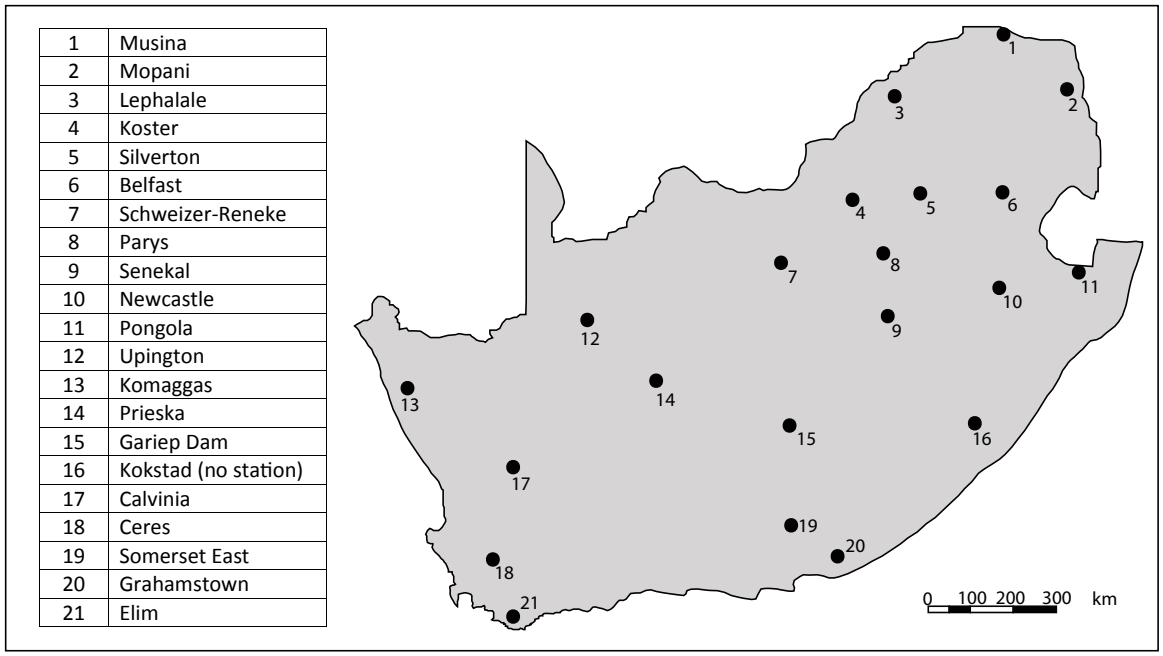

Figure 1.1: The locations of the 21 seismic stations operated by the South African National Seismograph network. Adapted from Brandt *et al.* (2005).

For this study, a temporary seismic array consisting of fifteen stations was deployed from 22 February to 25 May, 2012 to record micro-seismic activity in the Ceres and Tulbagh region. All data were manually processed for 1) arrival time of P- and S-waves to obtain hypocenter locations; 2) coupled hypocenter-velocity inversion to produce a one dimensional (1D) velocity model for the region; 3) hypocenter relocation with the calculated velocity model; 4) empirically derived local magnitudes for the seismic events. The location of the seismic events from this study is compared to, and shows good correlation with, the distribution of aftershocks following the M_L 6.3 Ceres earthquake of 1969.

Chapter 2

Seismology

2.1 Earthquake seismology

The majority of seismic events on Earth occur along active plate boundaries, i.e. interplate seismicity (Romanowicz, 2008). Seismic activity also occur in plate interiors and can be triggered by events other than earthquakes, such as explosions, rock falls and volcanic eruptions. The causes of intraplate seismicity that are not related to volcanism or mass movement are not as obvious as on plate boundaries. Previous research proposed that intraplate seismicity is concentrated on weak zones in the crust (Sykes, 1978) or on localised stress concentrations, for example near intrusions (Campbell, 1978). According to Sibson (1983), displacement along faults in continental crust seems to occur on a network of existing fault zones rather than creating new structures.

Failure along a fault occurs when the shear stress acting on the fault plane exceeds the frictional strength. This usually takes place along new or preexisting structures by stick-slip mechanism (Brace and Byerlee, 1966). If the law of effective stress (Hubbert and Rubey, 1959) holds, the effective normal stress ($\sigma_n^{'}$) can be expressed as

$$\sigma_n^{'} = \sigma_n - P = \sigma_n - \lambda_v \sigma_v \tag{2.1}$$

where σ_n is the applied normal stress, σ_v is the vertical stress (assumed to be the lithostatic pressure), P is fluid pressure and λ_v is the pore fluid factor (Sibson, 1983). The frictional strength (τ_f) on a cohesion-less plane in the middle to upper crust can then be described by the relation

$$\tau_f = \mu\sigma_n^{'} \tag{2.2}$$

where μ is the coefficient of static friction with μ typically ranging from 0.6 to 0.85 for common rock-forming minerals (Byerlee, 1978).

Major earthquakes can be explained by the elastic rebound theory (Reid, 1911) in which tectonic stress built up from the relative movement of rocks on either side of a fault is suddenly released (Kanamori, 1973). The energy is converted into frictional heat on the fault plane, displacement of rock, and seismic waves (Kanamori and Rivera, 2006). The shaking associated with an earthquake is caused by seismic waves radiating outward from the fault rupture (Mussett and Kahn, 2000).

Various forms of seismic waves are generated including compressional (P), shear (S), Love and Rayleigh waves. For the purposes of this study only P- and S-waves will be considered. P-waves travel the faster and are thus easier to pick because they are not obscured by the interference of any later phases. Theoretically, velocities can be derived from physical properties of the medium. For rocks, P- and S-wave velocity are defined as

$$V_p = \sqrt{[(K + \frac{4}{3}G)/\rho]} \tag{2.3}$$

and

$$V_s = \sqrt{(G/\rho)} \tag{2.4}$$

respectively, where K is the bulk modulus, G is the shear modulus and ρ is the rock density (Mussett and Kahn, 2000; Shearer, 2009).

Hypocenter location of earthquakes are derived by inverting the difference between the arrival time of P- and S-waves (Havskov and Ottemöller, 2010). Inversion is common in many fields of science and is used to infer parameter values based on observations (Tarantola, 2006). The inversion for hypocenter locations can also involves a simultaneous inversion for a velocity model on which the relocation of hypocenter locations is based (Kissling, 1995). According to Havskov and Ottemöller (2010) it is not uncommon for seismic events to have location errors of the order of tens of kilometers.

Locating earthquakes depends strongly on the velocity structure of the underlying geology and accurate measurements of the arrival time of incident seismic waves at stations of known location. If the velocity structure of the underlying geology is unknown then errors in location can be much larger. Also, errors in location influence the velocity model on which the final model for event location is based. Inversion solutions are not unique (Tarantola, 2006) and thus the inversion with the lowest time residuals (difference in observed versus calculated travel times) and lowest root mean square (RMS) values in location errors is chosen as the solution as long as it represents a realistic scenario.

The velocity structure of a region can be estimated by field observations of the various rock types and the structures that govern their outcrop and how it will continue at depth, together with boreholes and seismic profiles. When using only the surface outcrops and extrapolating to depth, one needs to know the properties of the rocks in question as a function of depth and there is a high uncertainty involved. Boreholes and seismic profiles allow velocity structures that extend more accurately to greater depth.

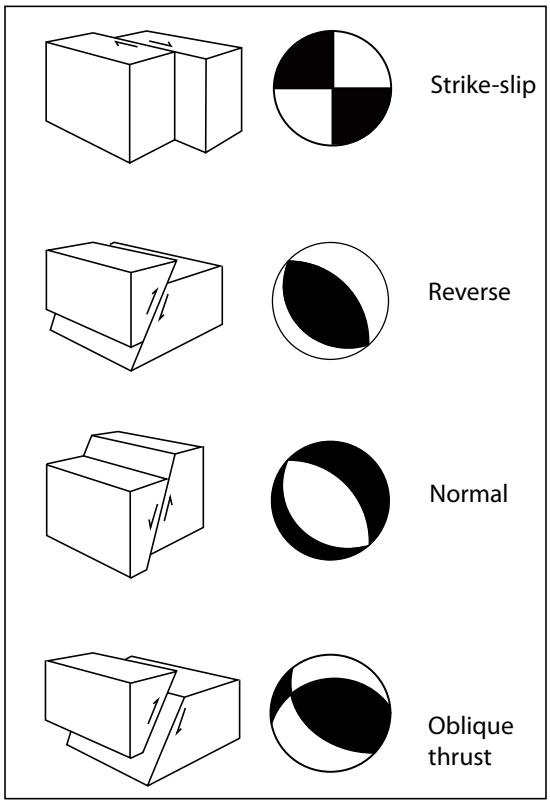

Figure 2.1: Graphical representation of the mechanism of faulting.

The first motion polarity of P-waves on a seismogram, i.e. up or down, of the same event will differ from one station to another due movement in either the pressure or tension axis of the focal sphere (Havskov and Ottemöller, 2010). The polarity and station locations can be plotted on an equal-area spherical projection to produce a focal mechanism of the rupture. The white and balck areas of the focal spheres (Fig. 2.1) represents areas of tension and compression, respectively, as the seismic wave front passes a point on the surface of the Earth. These graphical representations of the mechanism of faulting may yield information on the local stress field surrounded by the seismic array, i.e. extension or compression. Failure along existing faults will preferentially take place along suitably oriented structures (Brace and Byerlee, 1966; Sibson, 1985).

Apart from the orientation of existing structures, reactivation also depends strongly on the prevailing stress field and the mode of deformation (Hand and Sandiford, 1999). For a plane oriented such that its normal lies within the plane of σ_1-σ_3, and oriented at θ to σ_1, the

reactivation criteria can be described by

$$R = (\sigma_1/\sigma_3) = (1 + \mu \cot \theta)/(1 - \mu \tan \theta) \tag{2.5}$$

where σ_1 and σ_3 are the highest and lowest effective principle stresses, respectively and θ is the angle of reactivation (Sibson, 1985). However, it is possible for a fault to remain inactive despite being suitably oriented for reactivation. This may be due the failure shear stress (τ) acting on the fault not exceeding the shear strength of the fault (τ_f) (Sibson, 1983). Suitably oriented faults may contribute significantly to intraplate earthquakes and are thus important in considering the source of intraplate seismicity (Hand and Sandiford, 1999; Li *et al.*, 2009)

2.1.1 Magnitude

The magnitude (M) of an earthquake is a measure the size of an earthquake, independent of where it occurredLee *et al.* (2003). As originally defined by Gutenberg and Richter (1944) the magnitude is proportional to the maximum recorded amplitude on a seismogram located 100 km from the epicenter. Local magnitude (M_L) is the most cited measure of energy release during a rupture (Kanamori and Anderson, 1975; Abercrombie, 1995; Choy *et al.*, 2009), can be derived from amplitude measurements on seismograms and is expressed as follows

$$M_L = \log(A) + x \log(r) + y(r) + z \tag{2.6}$$

where A is amplitude, x is geometrical spreading, r is epicentral distance, y is an attenuation correction factor and z is a base level correction factor (Havskov and Ottemöller, 2010). The base level correction factor relates the amplitude of the recorded event to the amplitude of an event of known magnitude so as to calibrate local events. M_L is not the best magnitude scale for comparing earthquakes in different parts of the world, as the M_L scale is relative to a reference amplitude and region-specific correction factors. However, as it is a comparison of amplitude values it is useful for local networks operating regions with relatively homogeneous attenuation and geometrical spreading values.

Various magnitude scales exist (Kanamori, 1977) to communicate the size of an earthquake and, in general, .

The seismic moment (M_o) of an earthquake is proportional to the amount of slip on a given rupture area and is defined as

$$M_o = GS\bar{D} \tag{2.7}$$

where G is the shear modulus of the rock involved in Pa, S is the rupture area on the fault in m^2, and $\bar{D}$ is the average slip distance in m and M_o is in Nm (**?**).

Moment magnitude (M_w) can be defined as

$$M_w = 2/3 * \log M_o - 10.7 \tag{2.8}$$

(Hanks and Kanamori, 1979). M_w is useful to relate magnitudes of earthquakes in different parts of the world as it is proportional to physical parameters of displacement.

Based on the spectral properties of S-waves recorded on torsion seismographs, M_L can be empirically related to M_o by

$$\log M_o = 1.5M_L + 16.0 \tag{2.9}$$

(Thatcher and Hanks, 1973). Because no source parameters of the microseisms could be obtained, only M_L will be considered during this study .

The frequency-magnitude distribution of earthquakes follow the Gutenberg-Richter relation of

$$\log N = a + bM \tag{2.10}$$

where N is the cumulative number of earthquakes larger than magnitude M, a is a measure

of seismic activity, and $b \approx 1$ (Gutenberg and Richter, 1944; Wesnousky, 1999). Both a and b are empirically derived region-specific constants.

The scaling together with the frequency distribution of earthquakes have been thought to deviate from predicted values at the low and high end of the magnitude spectrum (Gutenberg and Richter, 1944; Aki, 1967). Also, the M_L scale suffers saturation with large earthquakes (Hanks and Kanamori, 1979). However, Abercrombie (1995) argues that this may be due to strong attenuation of seismic waves near the Earth's surface as no breakdown in scaling for stress drop were observed over a magnitude range of -1 $< M_L <$ 5.5 during the Cajun Pass scientific experiment.

Microseismic events are small earthquakes (-2 $<$ M $<$ 1) that are usually not detected by conventional seismic monitoring stations due to their low magnitude (Warpinski, 2009). Microseisms are commonly used in the petroleum industry to obtain location information of the subsurface drill-head. The magnitude of completeness (M_c) can be defined as the magnitude above which 90% of events can be fitted to a power law frequency-magnitude function (Eqn. 2.10) (Wiemer and Wyss, 2000). It is an essential part of seismology (Mignan, 2012) since an erroneous M_c value can lead to incorrect b values and thus inaccurate prediction of recurrence of earthquakes of a given magnitude.

Seismic waves attenuate as they travel through the Earth with the total attenuation due to a number of mechanisms such as frictional dissipation, thermoelastic relaxation, atomic diffusion, and dislocation (Walsh, 1966; Jackson and Anderson, 1970). Attenuation is believed to be stronger in rock with pore fluid than dry rock (Toksöz *et al.*, 1979).

According to Warpinski (2009), seismic waves tend to decay at a rate of $1/r$ imposing a detection limit on the possible seismic events an instrument can record based on the distance from the source. It follows that the larger the magnitude of an earthquake, the greater the detection limit of the instrument and, importantly, to detect small events, instruments have to be near to the source.

2.1.2 Intensity

The Modified Mercalli Intensity (MMI) scale is a non-mathematical scale that qualifies the effect of an earthquake in terms of ground motion (Wood and Neumann, 1931). It is compiled from observed effects such as objects shaking and damage to buildings but can also be estimated from landslides, rockfalls and structural damage (USGS, 2013).Peak ground dispacements are larger on alluvium than on bedrock (Trifunac and Brady, 1975) and the epicenter roughly coincides with the location of the highest intensity recorded for a particular event. It is designated Roman numerals and contains 12 classes.

Chapter 3

Seismicity in South Africa

3.1 The South African National Seismograph Network

The Geological Survey (now the Council for Geoscience (CGS)) initiated the South African National Seismograph Network (SANSN), which started permanent recording of seismic events in 1972 following the destructive earthquakes of 1969 and 1970 in the Ceres and Tulbagh region of the Western Cape (Saunders *et al.*, 2008). Initially seven stations were set up which was increased to 27 stations by 1997 of which currently there are 21 stations in operation (Saunders *et al.*, 2008). An estimated total of 73 documented earthquakes occurred in South Africa from 1620 to 1971 of which 15 exceeded M_L 4.5 (Theron, 1974). Singh *et al.* (2009) estimate that there were over 27 000 earthquakes ranging from $0.2 < M_L < 6.3$ from 1620 to 2008.

3.2 Seismicity in South Africa

Generally, seismic activity in and around Southern Africa can be classified as typical of an intraplate region with most of the natural seismicity occurring along the plate boundaries of the Mid-Atlantic and Southwest Indian oceanic ridges (Saunders *et al.*, 2008; Delvaux and Barth, 2010). Earthquake locations in South Africa tend to be clustered in space (Fig. 3.1) and the events are largely of moderate magnitude, from a shallow source and are difficult to

correlate with known geological structures (Saunders *et al.*, 2008; Singh *et al.*, 2009). The only area in Southern Africa that might deviate from the intraplate regime is where seismic activity may be attributed to the southward propagation of the East African Rift System (EARS) into southern Mozambique (Fig. 3.2 (Saunders *et al.*, 2008; Brandt and Saunders, 2011; Malservisi *et al.*, 2013). Stress field estimations in the EARS is made possible by numerous focal mechanisms from a tectonic source (Delvaux and Barth, 2010). Due to the intraplate setting, data are fewer in South Africa relative to the EARS and therefore focal mechanisms and stress field estimations are also few.

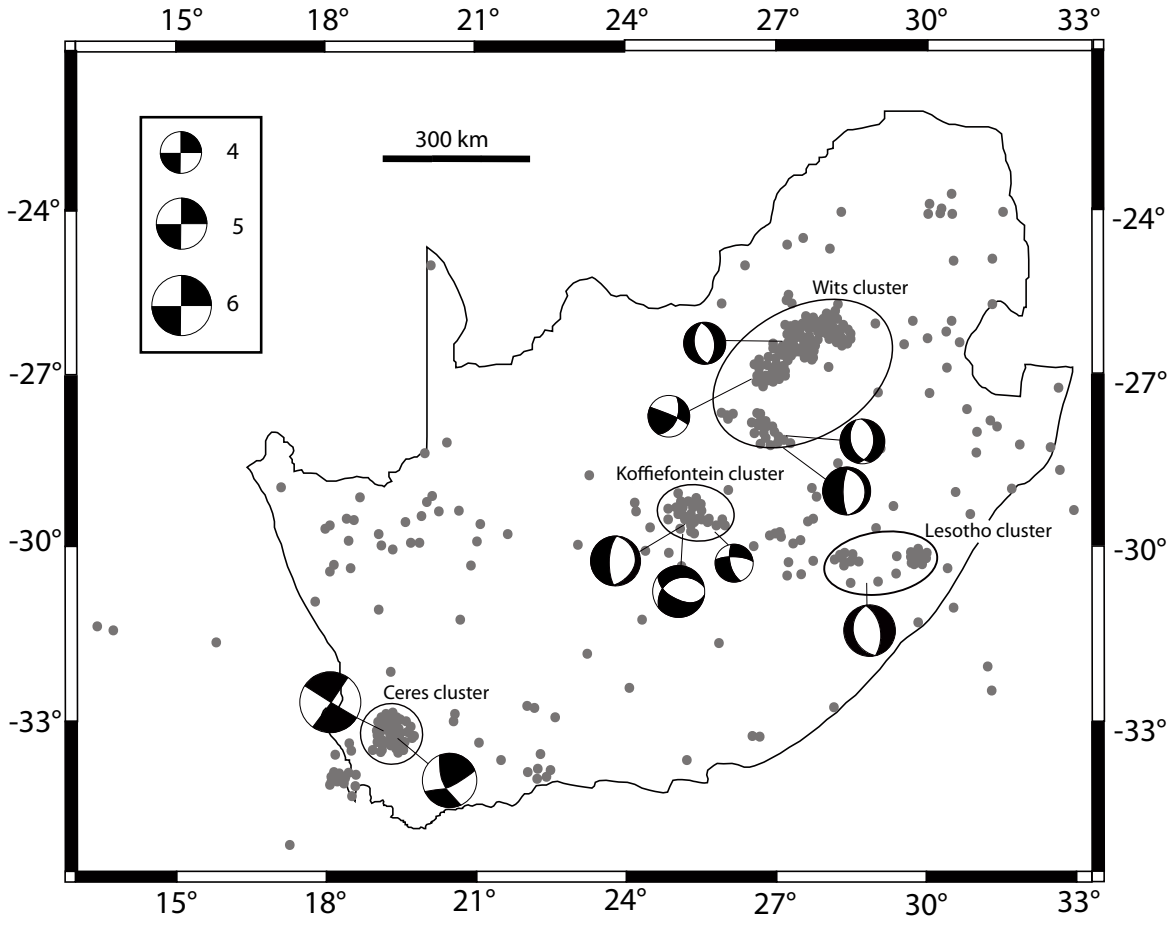

Figure 3.1: The distribution of seismic activity in South Africa is clustered spatially. Focal mechanisms from the Koffiefontein, Wits and Lesotho clusters predominantly indicate normal faulting. The Ceres cluster contains the largest recorded earthquake in South African history and is characterised by strike slip faulting and the highest rate of tectonic seismicity in South Africa. Adapted from Brandt and Saunders (2011) and Singh *et al.* (2009).

The bulk of recorded seismicity in South Africa results from underground mining activity in the gold and platinum fields of Gauteng, North West and Free State Provinces (Saunders *et al.*, 2008; Singh *et al.*, 2009). Focal mechanisms located in the Kaapvaal tectonic province (Fig. 4.2) and the interior of the country exhibits a normal faulting regime (Brandt and Saunders, 2011) accommodating extension. Seismic activity of tectonic source is most pronounced in the Western Cape (Kijko *et al.*, 2002) with only two focal mechanisms available for this region, both of which illustrate sinistral strike slip movement (Green and McGarr, 1972; Brandt and Saunders, 2011).

The mechanisms of faulting (Fig. 2.1) are a function of the prevailing local or regional stress fields acting on the lithosphere with first order stress patterns related to plate boundary forces (Pavoni, 1992). The lithospheric stress state can contribute to the understanding of tectonic forces acting on plates (Richardson *et al.*, 1979). The African plate is almost entirely surrounded by spreading ridges (Fig. 3.2). Thus one would expect the whole African plate to be under a compressive regime due to ridge push forces (Delvaux and Barth, 2010). Although the stress field in South Africa is not well constrained due to very few focal mechanisms from natural sources relative to, for example, the EARS (Delvaux and Barth, 2010), focal mechanism inversion combined with over-coring from mining boreholes show that, in general, South Africa is experiencing a normal faulting stress regime with a vertical σ_1 accommodating E-W extension in the upper crust (Delvaux and Barth, 2010). This is supported by a geodetic measurements from Malservisi *et al.* (2013) who also found that the Cape Town region exhibits higher than average strain rates with plate velocities indicating movement to the north-west.

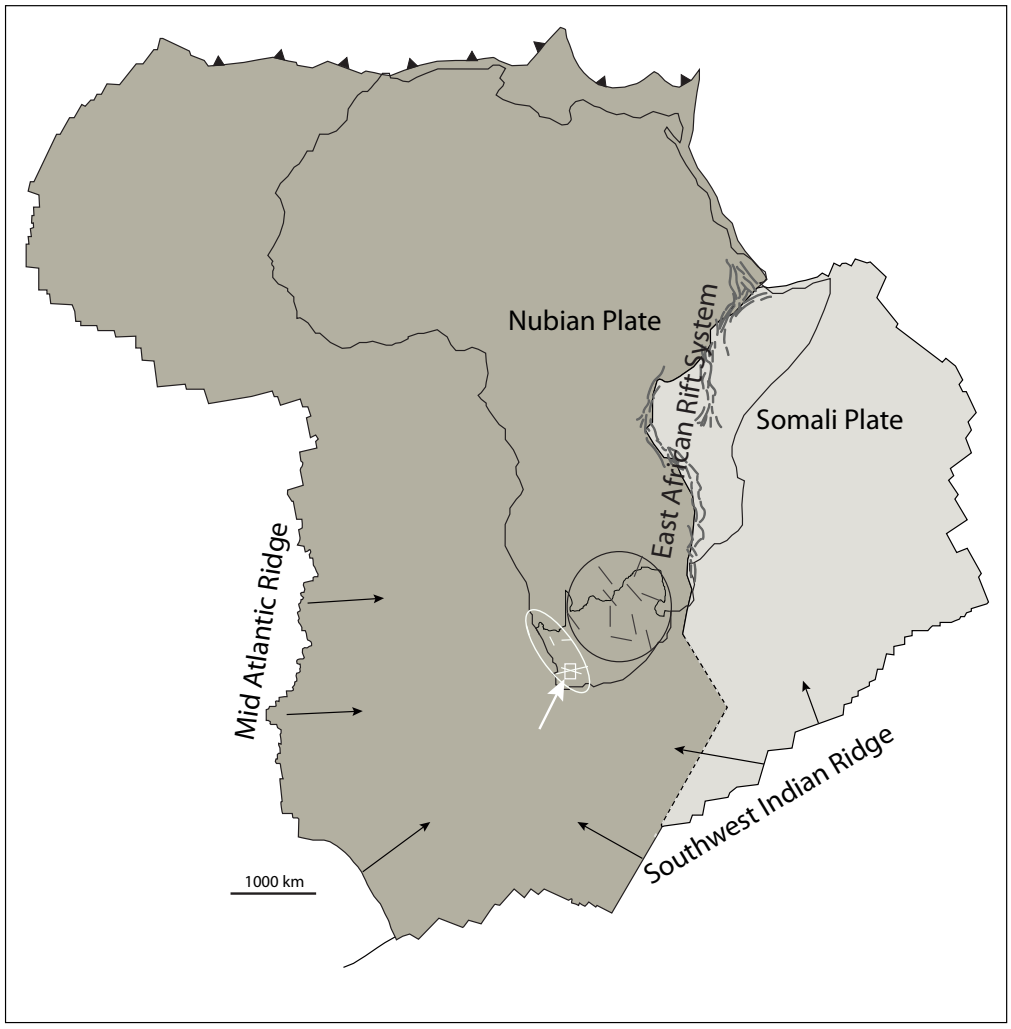

Figure 3.2: The African plate is commonly treated as two incipient plates due to rifting associated with the East African Rift System. Except for subduction along the northern margin, the Africa plate is surrounded by spreading ocean ridges and the continent is large associated with stable continental margins. The black arrows represent the inferred directions of compressive stress in the surrounding ocean crust assuming a compressive force perpendicular to spreading. The study area is loacted in the white box pointed out by the white arrow. Adapted from (Zoback, 1992) and (Ben-Avraham *et al.*, 1997).

The western Cape region is different in that it is experiencing a strike-slip faulting regime. Neotectonic faulting in the Orange Basin, southwestern Africa, is ascribed to strike-slip faulting with a NNW strike (Viola *et al.*, 2005). Seismic database and satellite image analysis by Andreoli *et al.* (1996) indicate a broad zone where the maximum compressive stress is

oriented NW-SE along the west coast of southern Africa (Fig. 3.3). This zone has been defined as the Wegener Stress Anomaly (WSA) (Andreoli *et al.*, 1996). Although this zone does not include only NW-SE trending stress vectors it believed to represent a zone as it includes faulting mechanisms and stress measurements that are different relative to the interior of South Africa. For example, a focal mechanism from the 1969 Ceres earthquake in South Africa (refer to next section) indicates strike-slip movement with the fault zone striking at 288 (Green and McGarr, 1972). Stress measurements in the Carolusburg mine, Namaqualand, South Africa, yielded the following principle stress orientations and magnitudes:

σ_1 = 90 MPa oriented NW/NNW

σ_2 = 40 MPa oriented vertically

σ_3 = 36 MPa oriented SE/ESE (Viola *et al.*, 2005).

According to Andersonian theory, strike-slip faulting is associated with a vertical σ_2 and will fault at 30° to a horizontal σ_1 (Anderson, 1951).

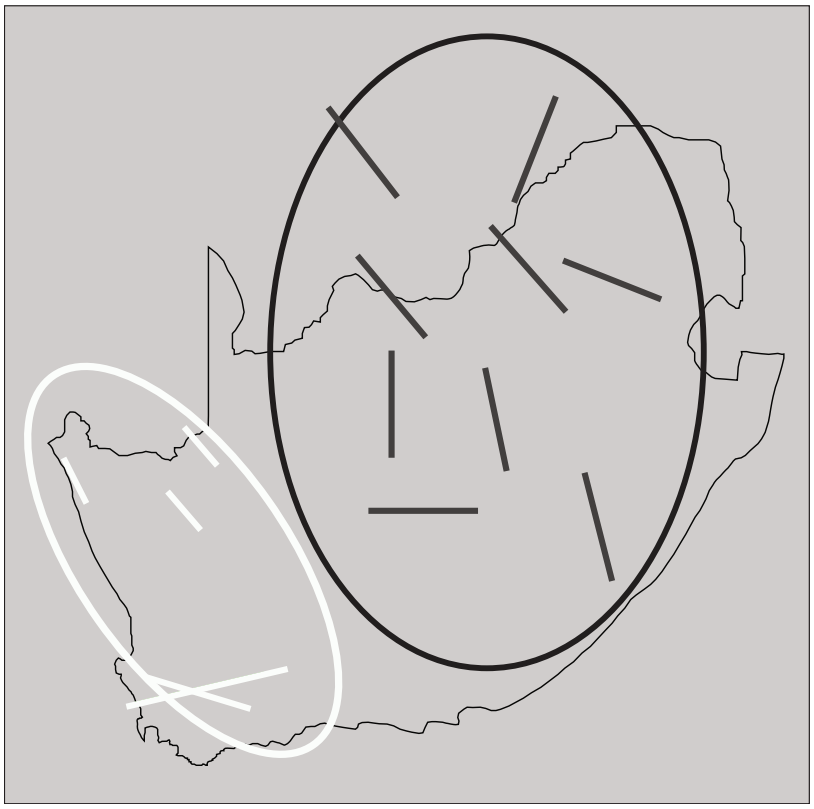

Figure 3.3: A simplification of the direction of maximum horizontal stress (white and black lines) Central South Africa is experiencing an extensional stress field and thus normal faulting commonly occurs (black ellipse). Conversely the western margin of South Africa (white ellipse) shows evidence of a maximum horizontal compressive stress in a roughly NW-SE orientation (Andreoli *et al.*, 1996) leading to slip faulting. Adapted from (Zoback, 1992) and (Ben-Avraham *et al.*, 1997)

3.3 The 1969 and 1970 Ceres earthquakes

The Western Cape exhibits the highest levels of seismic activity in South Africa from a tectonic source (Kijko *et al.*, 2002). The Ceres cluster has the record of the largest seismic event to date in recorded history in South Africa, namely the M_L 6.3 earthquake of September 29, 1969 (Green and Bloch, 1971; Singh *et al.*, 2009). A sinistral strike-slip focal mechanism (Fig. 3.4) was derived for this event (Green and McGarr, 1972).

In a data review, Singh *et al.* (2009) estimate that the Ceres cluster experiences six $1 < M_L < 3$ earthquakes per month.

Tremors were reported by locals in the days leading up to the main shock, which occurred at 20:03 local time, and was preceded by two shocks of M_L 4.5 and 4.3 at 09:02 and 17:22, respectively, recorded by the Hermanus Magnetic observatory and a seismology station in Pretoria (Theron, 1974; Fernandez, 1974). A temporary seismic array was deployed in the Ceres region to record the aftershocks of the M_L 6.3 epicentre. Locations of the aftershocks delineated a fault zone with orientation 299/88 SE (Green and Bloch, 1971) (Fig. 3.5). The aftershock zone is roughly 3 km wide, 20 km long and 9 km deep (Green and Bloch, 1971). The depth of the aftershocks decreased from Tulbagh toward Ceres with no shocks less than 5 km deep recorded in the Tulbagh (Green and Bloch, 1971). On April 14, 1970, an M_L 5.7 shock with a sinistral strike-slip motion occurred 12 km south east of the M_L 6.3 event (Green and Bloch, 1971). Aftershocks of the April 14 event occurred along 8 km of the original 20 km long inferred fault zone (Green and Bloch, 1971). A Maximum Mercalli Intensity (Tab. **??**) of VII was reported for the main shock (Keyser, 1974).

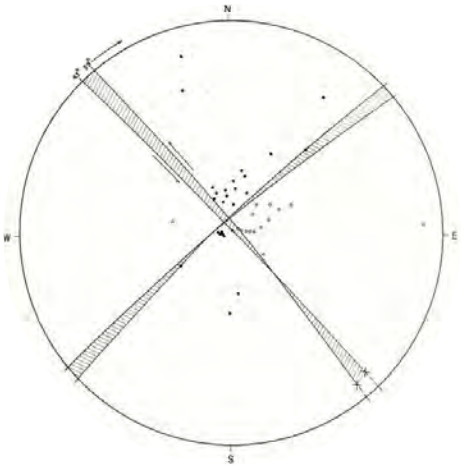

Figure 3.4: Focal plane solution derived for the M_L 5.7 shock of April 14, 1970 by Green and McGarr (1972).

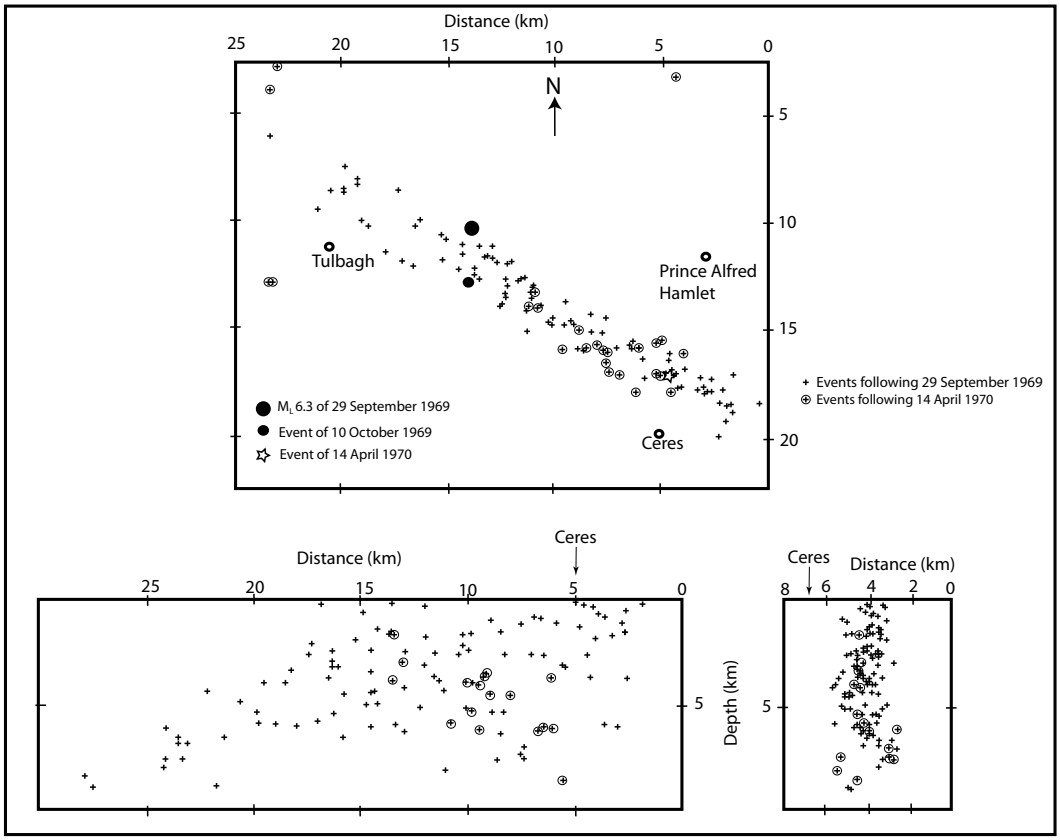

Figure 3.5: Distribution of aftershocks following the 1969 M_L 6.3 earthquake as recorded by Green and Bloch (1971).

According to Green and Bloch (1971), 26 cm of displacement was generated by the M_L 6.3 event. The rupture was thought to have nucleated along the extension of the Kango-Baviaanskloof Fault (Singh *et al.*, 2009). However, the lack of any surface rupture or fault scarp makes this difficult to test and previously mapped faults do not correlate to the rupture zone illuminated by the aftershocks (Green and Bloch, 1971). Despite the lack of surface rupture, sand volcanoes were reported both in Ceres and Prince Alfred Hamlet (Keyser, 1974; Gordon-Welsh, 1974). In Ceres the sand volcanoes stretched along a line parallel to the river bank and were apparently limited to areas directly around the epicenter (Keyser, 1974; Gordon-Welsh, 1974).

A seismic refraction profile across the southern Cape Fold Belt by Stankiewicz *et al.* (2007) revealed good correlation between shallow geological features and surface outcrops. They were also able to create a P-wave velocity model down to a depth of 25 km. Velocity models

are not known for the Ceres area and a structure was produced based on a first guess of the model. This will be discussed further in the methods chapter.

Saunders *et al.* (2013) recently derived an empirical M_L scale for South Africa. An M_L 2.4 event that occurred at 14:21:03 on 11 March 2012 was recorded by the Council of Geoscience (CGS) of South Africa and was also recorded by the temporary array used during this study (Fig. 5.14). The above-mentioned event was used as a calibrating event for local magnitude calculations during this study and will be discussed further in chapter 5.

Chapter 4

Geological Setting

4.1 Geological history of the study area

The lithosphere of southern Africa largely comprises of Archean cratons surrounded and sutured by younger shear zones and fold belts (Begg *et al.*, 2009; Viola *et al.*, 2012). The cratonic margins have undergone successive tectonic cycles of rifting and accretion and have influenced African tectonics greatly by, for example, channeling upwelling magma such as in the East African Rift System (EARS) (Begg *et al.*, 2009). The Archaean Kaapvaal craton (Zegers *et al.*, 1998) is bound to the west by the Kheis Belt, a Paleoproterozoic accretionary terrane (de Wit *et al.*, 1992). The Mesoproterozoic Namaqua Natal Metamorphic Belt (NNMB) is a poorly exposed terrane south of the Kaapvaal craton and west of the Kheis Belt stretching almost the entire width of South Africa and as far south as the coast line (de Wit *et al.*, 1992; Lindeque *et al.*, 2007). The Pan-African Saldania Belt is an accretionary belt which is only exposed in a few basins which formed during the breakup of Gondwana that overlies the NNMB (Frimmel *et al.*, 2013). Rocks of the Saldania Belt were intruded by the late Precambrian Cape Granite Suite. The Late Permian Cape Fold Belt (CFB) borders the south western margin of South Africa and overlies the Saldania belt and the Cape granite.

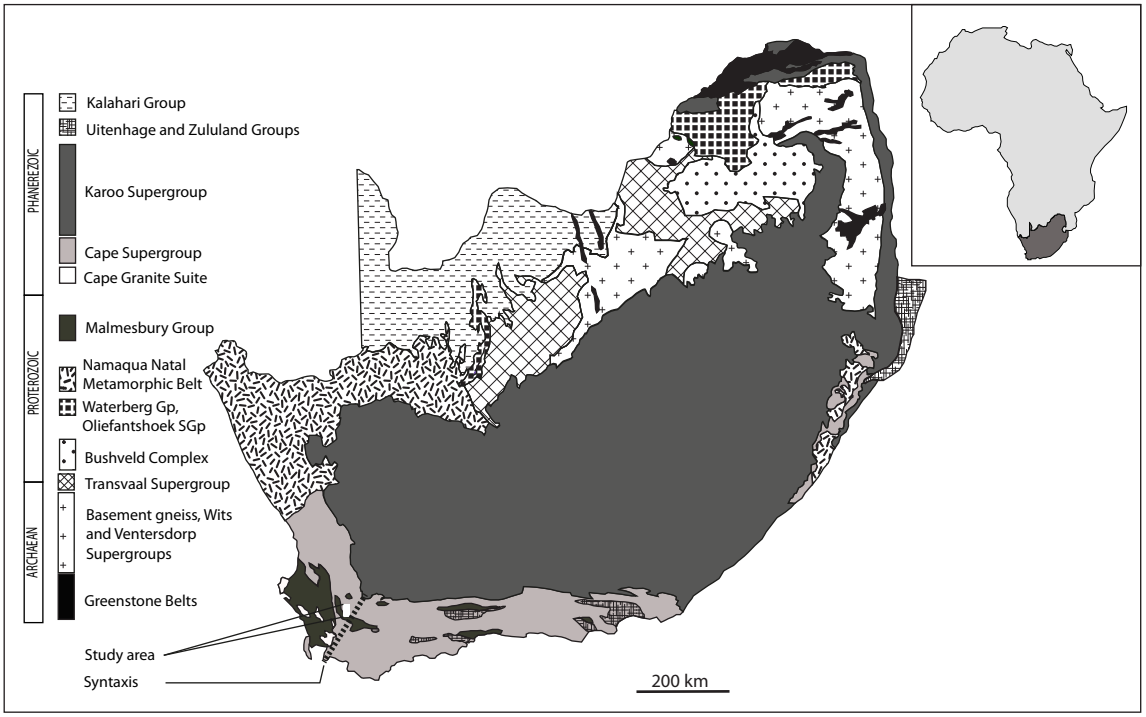

Figure 4.1: Simplified geological map of South Africa. Note the outcrop of the Cape Supergroup (CSG) rocks defining the Cape Fold Belt (CFB) and the syntaxis (dotted line) which divides the the CFB in western and southern limbs (Mielke and de Wit, 2009). The study area (white square) is located immediately north west of the syntaxis. Adapted from Johnson *et al.* (2009).

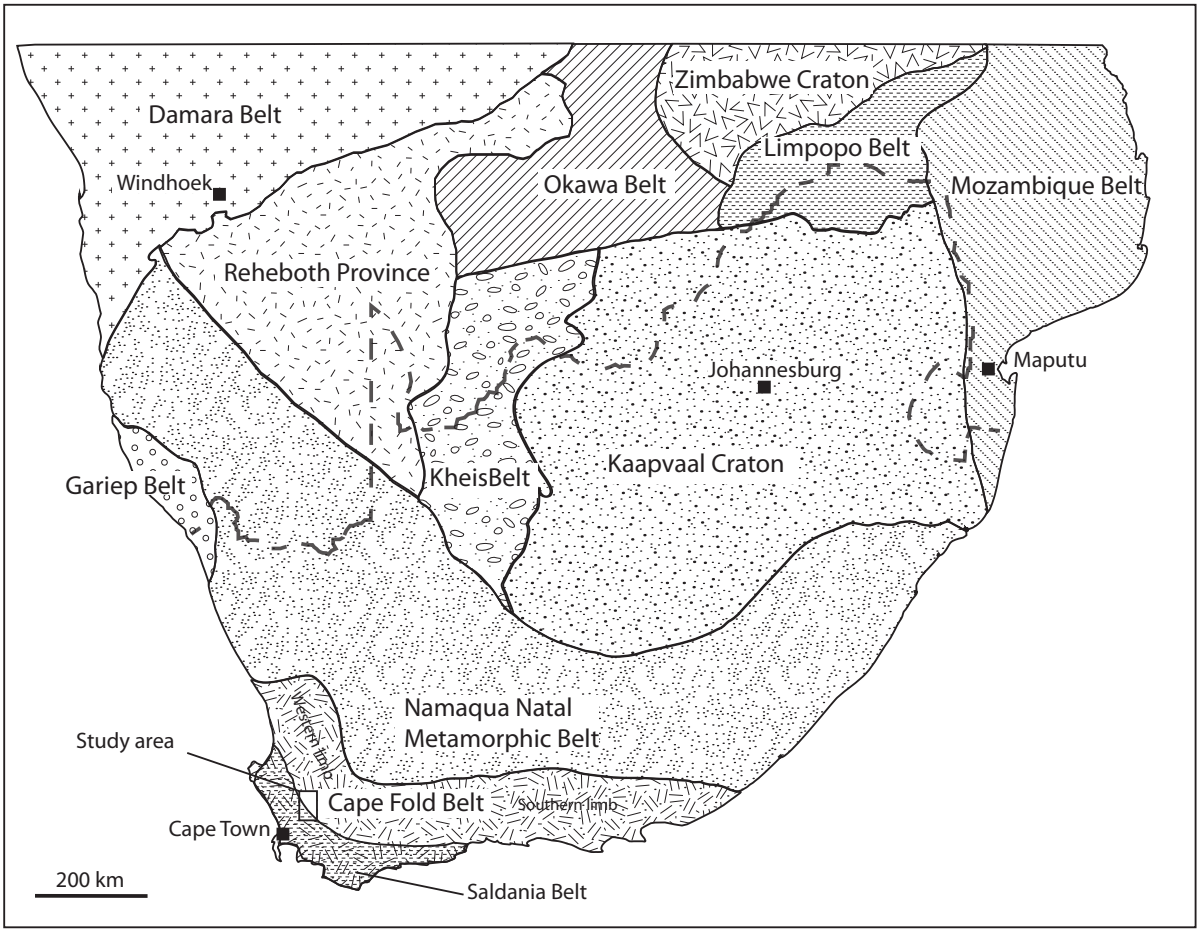

Figure 4.2: Figure depicting the tectonic provinces of Southern Africa. The Cape Fold Belt (CFB) is present on the southern and western margins of South Africa and overlies the Saldania Belt. Adapted from Viola *et al.* (2012).

The study area is situated in the syntaxis of the CFB (Fig. 4.1). The syntaxis a structurally complex region where there is a change in orientation in the structural trend within the fold belt from generally NW-SE striking structures of the western limb to broadly E-W striking the southern limb (Fig. 4.2). The topography of the study region is dominated by the resistant quartzite ridges of the Table Mountain Group (TMG) and the low lying Tulbagh valley consisting of Malmesbury Group (MG) shales. The Ceres region is thousands of kilometers away from the nearest plate boundary (Fig. 3.2) and in general, South Africa can be considered as a stable continental region (Schulte and Mooney, 2005; Saunders *et al.*, 2013). The rocks that crop out in the study area are the MG plus the TMG, Bokkeveld

Group (BG) and minor Witteberg Group (WG) of the Cape Supergroup (CSG) (Fig. 4.3).

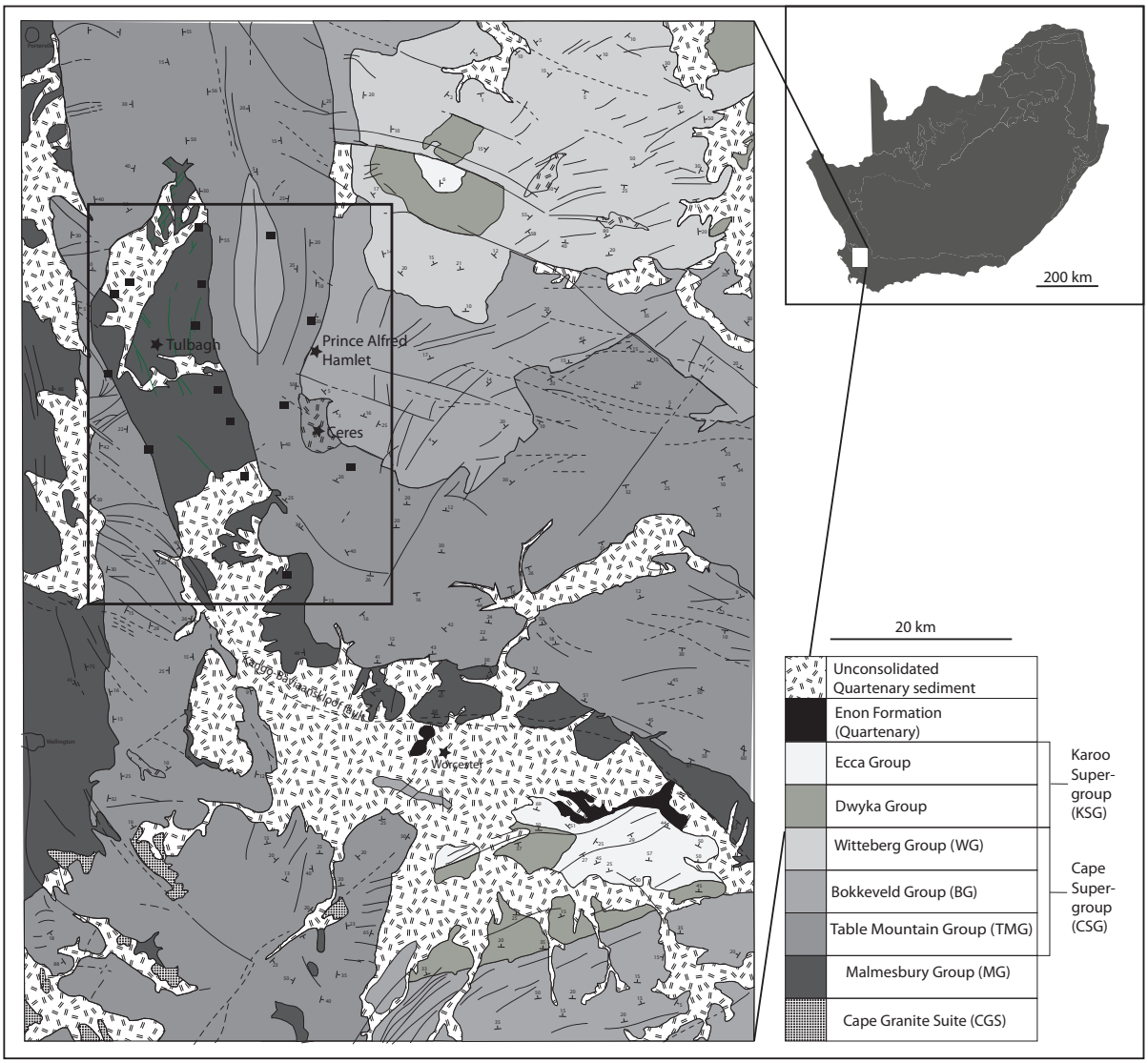

Figure 4.3: Simplified regional geology of the Ceres and Tulbagh area with the study area shown as a rectangular box including all the station locations. Adapted from Gresse (1997).

4.1.1 The Namaqua Natal Metamorphic Belt (NNMB)

The NNMB is only exposed in the north west and in the east of South Africa (Fig. 4.1) and is for the most part covered by younger sedimentary rocks of the Karoo Supergroup (KSG). However, the NNMB is thought to be extensive across the width of South Africa below the KSG rocks (Fig. 4.2). It largely consits of low-pressure, high-temperature granulite facies

rocks of crustal origin which are believed to have formed part of the assembly of Rodinia at 1.0 to 1.2 Ga (Raith *et al.*, 2003). Some of the crustal components of the NNMB have been dated with Sm/Nd at 2.1 to 1.6 Ga (Clifford *et al.*, 1995) which shows that the region experienced significant reworking and metamorphic overprinting during the Rodinia assemblage. (Clifford *et al.*, 1995) also found that the NNMB rocks have a low grade Pan African metamorphic overprint. There must be multiple generations of structures within the NNMB, but due to the lack of outcrop there is very little information on the structural trend within this metamorphic belt in the Western Cape.

4.1.2 Malmesbury Group

The Malmesbury Group of the Nama Supergroup is a succession of rocks associated with the Pan-African-aged Saldania Belt (Fig. 4.2). It is a lower greenschist facies orogenic belt along the southern and southwestern margins of the Kalahari craton (Rozendaal *et al.*, 1999; Belcher and Kisters, 2003; Gresse *et al.*, 2009). Outcrops of the Malmesbury Group are found north and north east of Cape Town (Fig. 4.1). Generally two models exist for the Malmesbury Group. Rozendaal *et al.* (1999) and Gresse *et al.* (2009) argue that the Pan-African age Colenso Fault separates the Tygerberg and Swartland terranes and the Piketberg-Wellington Fault separates the Tygerberg and Boland terranes. However, Frimmel *et al.* (2013) suggested that the Piketberg-Wellington Fault is the only terrane boundary fault in the region separating the 609-532 Ma Boland terrane from the 557-552 Ma Malmesbury terrane. Belcher and Kisters (2003) and Frimmel *et al.* (2013) have proposed that the Swartland and Tygerberg terranes be assimilated into the Malmesbury terrane on the basis of stratigraphical similarity and the notion that the Colenso Fault, previously suspected to be a terrane boundary fault (Rozendaal *et al.*, 1999), is an inherited structure from the underlying Namaqua-Natal Metamorphic Belt (NNMB) (Belcher and Kisters, 2003; Frimmel *et al.*, 2013). Thus, Belcher and Kisters (2003) and Frimmel *et al.* (2013) maintain that the subdivision into three distinct terranes cannot be upheld. It has been proposed that the Swartland and Tygerberg terranes be viewed as one and referred to as the Malmesbury Terrane separated from the Boland Terrane by the main tectonic boundary of the Piketberg-Wellington Fault (Frimmel *et al.*, 2013). In this study the Malmesbury Group would refer to the collective Malmesbury and Boland Terranes.

The age of deposition of the Malmesbury Group is not well constrained, nor is the depositional environment. Age estimates range from 780 to 750 Ma (Rozendaal *et al.*, 1999), 580 to 575 Ma (Belcher and Kisters, 2003) and 609 to 532 Ma (Frimmel *et al.*, 2013). Deposition appears to be syntectonic with crustal convergence that formed the Saldania orogen (Rozendaal *et al.*, 1999; Frimmel *et al.*, 2013). Isoclinal folding and thrusting occurred and the main trend in the structures have a north-west south-east orientation (Belcher and Kisters, 2003). Both the Colenso and Piketberg-Wellington Faults show evidence for reactivation with both sinistral and dextral strike-slip motion (Rozendaal *et al.*, 1999; Belcher and Kisters, 2003; Frimmel *et al.*, 2013). Deformation occurred during the Saldania orogeny in which parts of east and west Gondwana collided and amalgamated (Rozendaal *et al.*, 1999). The Saldania Belt was in places intruded by the late Precambrian to Early Cambrian Cape Granite Suite roughly 547 to 536 Ma (Da Silva *et al.*, 2000; Scheepers and Schoch, 2009).

The Tulbagh valley is underlain by rocks of the Boland terrane of the Malmesbury Group which comprise sub-greenschist facies siliciclastic sedimentary and volcanic rocks (Rozendaal and Scheepers, 1995; Rozendaal *et al.*, 1999; Frimmel *et al.*, 2013). Significant areas of bedrock are today covered by weathered clay or alluvial sediment (Fig 4.3). The strata in the study area are folded with open to tight upright folds with a near vertical axial planar cleavage and are north-south to NW-SE striking (Fig 4.4), (Hartnady *et al.*, 1974; Belcher and Kisters, 2003; Frimmel *et al.*, 2013). The Malmesbury Group rocks were intruded by the Cape Granite Suite .

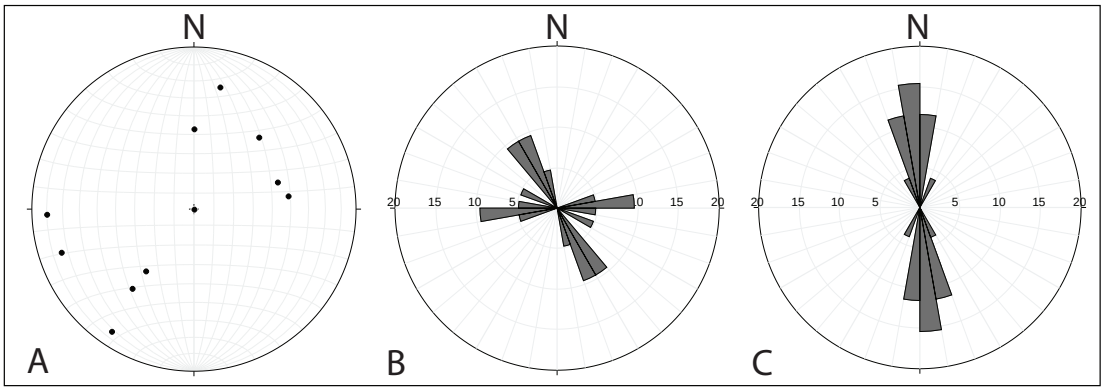

Figure 4.4: Summary of structural elements for the Malmesbury Group rocks present in the study area. A: Equal area stereo plot of poles to bedding planes. B: Rose diagram showing trend of fault surface traces. C:Rose diagram showing the strike of fold axial traces. Data for these plots were taken from Gresse (1997).

4.1.3 Cape Supergroup

The Early Ordovician to Early Carboniferous Cape Supergroup (CSG) crops out along the southern and western margins of South Africa (Fig. 4.1). The CSG comprises up to 10 km of siliciclastic sedimentary rocks ranging from quartzites and feldspathic arenites to silt and shale, with quartzites by far the dominant lithology (Tham and Johnson, 2009). Deposition occured in the Cape Basin which overlies Precambrian to Cambrian rocks of, amongst other, the Malmesbury Group and the Cape Granite Suite (Johnson, 1991; Cloetingh *et al.*, 1992; Frimmel *et al.*, 2001; Shone and Booth, 2005; Tham and Johnson, 2009). The quartzite dominated Table Mountain Group (TMG) consists of thick bedded sand of shallow marine to fluvial origin with abundant invertebrate fossils (Tham and Johnson, 2009). The Bokkeveld Group (BG) contains 5 complete coarsening upward sequences grading from mud to sand with well-preserved fossil assemblages including brachiopods, nautiloids and conodont fauna (Tankard and Barwis, 1982; Tham and Johnson, 2009). Micaceous shale and quartzite present in roughly equal proportions in the Witteberg Group (WG) preserved with evidence of multiple coarsening upward transgressive and regressive cycles with *Lycopod* fossils present in the Witteberg Formation (Tham and Johnson, 2009). Rocks of the CSG and MG were involved in the Permian to Triassic Cape orogeny that formed the present day Cape Fold Belt (CFB).

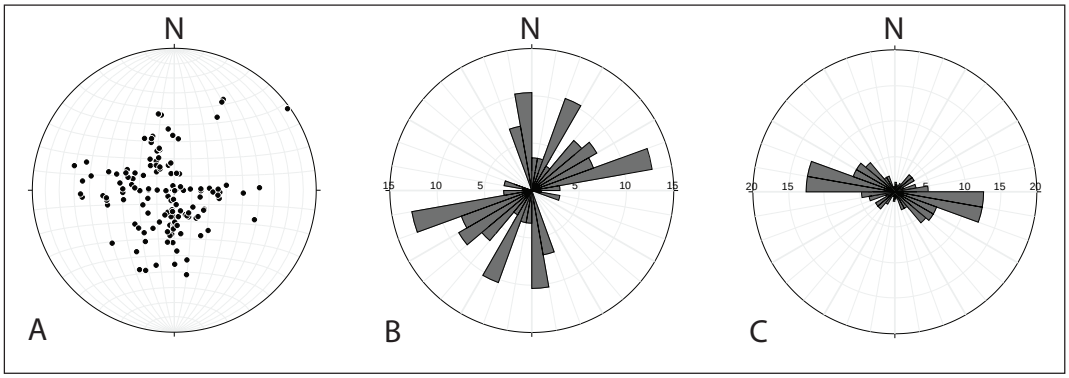

Figure 4.5: Summary of structural elements for the Cape Supergroup rocks present in the study region. A: Equal-area stereo plot of bedding planes. B: Rose diagram showing trend of fault surface traces. C:Rose diagram showing the strike of fold axial traces. Data for these plots adapted from Gresse (1997).

4.1.4 Karoo Supergroup

The Karoo Supergroup (KSG) rocks is a succession of glacial marine to marine to terrestrial clastic sedimentary rocks plus continental flood basalts with accompanying sills and dikes (Johnson *et al.*, 2006). It attains a maximum thickness of roughly 12 km and is host to a range of terrestrial vertebrate and plant fossil assemblages (Johnson *et al.*, 2006). There are only isolated downfaulted blocks of the KSG rocks present in the study area (Fig. 4.3) thus they don't form an important part of the underlying geology concerning this experiment.

4.1.5 The Cape Fold Belt

The deformation that formed the Cape Fold Belt (CFB) occurred from roughly 278 ± 2 to 230 ± 3 Ma (Hälbich, 1983b). It is a good example of an exposed foreland fold and thrust belt (Booth and Shone, 2002; Booth *et al.*, 2004; Mielke and de Wit, 2009) situated on the western and southern margin of Africa. The deformation associated with the CFB occurred along pre-existing structures, pre-dating the Cape orogeny, during the orgogeny phase and during the breakup of Gondwana (Paton *et al.*, 2006). The tectonically thickened quartzite of the CSG forms the ridges and cliffs of the Cape Fold Mountains in the south and west of South

Africa. The MG is poorly exposed but show signs of lower greenschist facies overprinting during the Cape orogeny (Frimmel *et al.*, 2013).

North verging folds together with an increase in metamorphic gradient from north to south is strongly indicative of an Andean type convergent margin with thin skin tectonics and compression from the south (Hälbich, 1983a; Frimmel *et al.*, 2001; Booth, 2011). Estimates of shortening ranges from 35-40 percent (Hälbich, 1983b; Newton *et al.*, 2006). The degree of deformation decreases from south to north and west to east in the southern and western limbs (Fig. 4.2), respectively, and only the lower units of the Karoo Supergroup are deformed (Johnson, 1991).

The syntaxis (Fig. 4.1) is a zone dividing the western and southern branches of the CFB (Mielke and de Wit, 2009). This area is characterised by fault surface traces and fold hinge lines changing orientation from broadly E-W trending in the southern limb to NW-SE trending in the western limb (Mielke and de Wit, 2009). The study area lies directly north west of the syntaxis. The southern limb is charaterised by north verging, closed to isoclinal folds and north verging thrust faults (Shone and Booth, 2005; Booth, 2011). The western limb is characterised by asymmetric open folds verging to the east together with thrust faults (Green and Bloch, 1971; Newton *et al.*, 2006).

Many models have been used in the past to attempt to explain the formation of the CFB and its associated syntaxis. Some models of formation include flat plate subduction (Lock, 1980), dextral transpression (Johnston, 2000), bulk deformation (Hälbich, 1983b) and thrust stacking (Shone and Booth, 2005). What is evident from all these models is that compressional tectonism and crustal shortening affected the Cape and and some of the Karoo Supergroup rocks.

Chapter 5

Methods

A temporary seismic array consisting of 15 stations was set up in the Ceres and Tulbagh region (Fig. 5.1) and left in the field to record for a period of three months. The array was set up to cover the aftershock zone (Fig. 3.5) of the M_L 1969 Ceres earthquake as completely as possible. The continuous data were manually processed for P- and S-wave arrival times, 1D velocity model and station corrections, hypocenter locations and empirically derived local magnitudes. A total of 172 microseismic events was located within the boundaries of the array during the duration of this experiment.

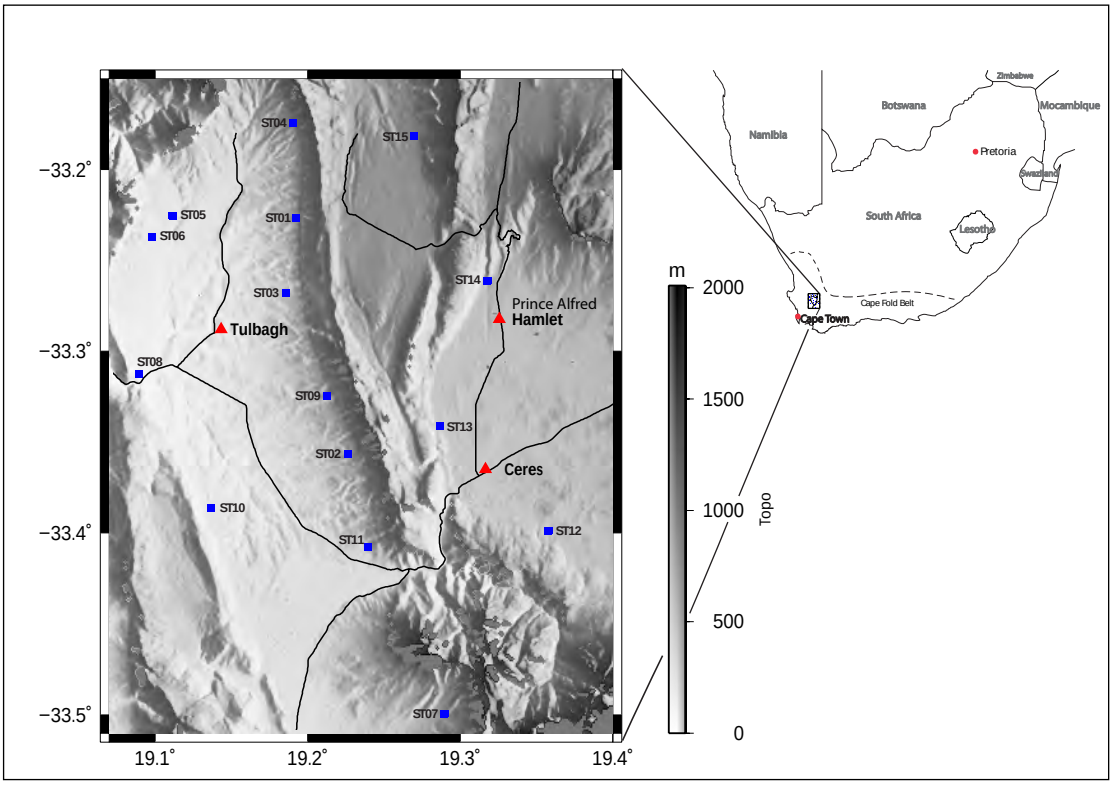

Figure 5.1: Location of the temporary seismic array used during this study. Red triangles show the location of the towns in the region with the blue squares representing the location of the 15 stations used during this study. The ridges comprise of resistant quartzites of the Table Mountain Group.The easily weathered Malmesbury Group shales underlies the low lying north-south trending Tulbagh valley in the west.

5.1 Instruments

The instruments (Fig. **??**) used during this experiment were supplied by the Geophysical Instruments Pool Potsdam (GIPP) of the German Research Centre for Geoscience (GFZ) in Potsdam, Germany. PE-6/B triaxial 4.5 Hz geophones made by SENSOR Nederland were used together with three channel DSS-cube data recorders (cubes). Each cube has a data storing capacity of 10 gigabytes (GB) and a built-in global positioning system (GPS) antenna which provided a time stamp of waveform data accurate to 10^{-6} s and the location coordinates of each station. The cubes were powered by a battery pack that lasted for an average of 51 days in laboratory test at the GFZ. It was decided to change batteries after six

weeks 42 days) to compensate for any difference between laboratory and field temperature conditions.

Figure 5.2: Instrumentation used during this study: three channel DSS-cube data recorder (middle) connected to a triaxial geophone (right) and battery pack (left) containing 8 D-size alkaline batteries. The top face of the cube was exposed to the sky during installation to ensure a GPS connection.

5.2 Data acquisition

The temporary seismic array that consisted of 15 stations was deployed in the aftershock zone of the 1969 Ceres earthquake (Fig. 5.1) and was installed with the help of scientists from the GFZ. The array was in the field from 20 February to 25 May 2012. All stations were installed on private farm land. The location of each station depended on access roads on the various farms but were installed as far away from main roads and farm activity as possible in order to minimise background noise from moving vehicles.

Each station was installed by digging a hole roughly 30 - 50 cm deep and placing the instruments in the bottom of the hole (Fig. 5.3A). Spikes at the base of the geophone ensured good coupling with the ground below. Arrows on the geophones were used to align the north-south component of the instrument with magnetic north and a bulls-eye level ensured horizontal installation. The cubes and battery packs were placed in plastic bags and taped shut to get

a watertight seal. These were placed in the hole on top of the geophones. The holes were filled in and the cubes were positioned such that the top face was exposed to the sky for a GPS connection (Fig. 5.3B). The soil in which the geophones were buried varied from sand to clay.

Figure 5.3: Station installation in the field. A: Geophones were placed in the bottom of a small hole. Spikes on the base of each geophone ensured good coupling with the ground below. B: Battery packs and cubes were sealed in plastic bags and placed in the hole on top of the geophone. Cube can be seen with the top surface exposed to the sky to maintain a GPS link.

Batteries were changed halfway through the experiment from 7-9 April after which the stations were left in the field for a further six weeks. Some of the battery packs were partly filled with water but still managed to power the cube. Data were downloaded in the field during the battery exchange (Fig. 5.4) and again after the the equipment was retrieved from the field. The first and second downloads of data will be referred to as batch one and two, respectively. On average, the stations recorded for 44 and 45 days during batch one and two, respectively. One station only recorded for 2 days after initial installation due to a faulty connection to the battery that caused a loss of power to the cube. This station also switched off and back on five times during the second batch as it was not possible to fix the connection in the field. Another cube only recorded for 19 days in batch one due to it being vandalised by baboons. The cube and geophone were undamaged in the process but the battery pack

was not found. A new battery pack was fitted and the station was reinstalled for the second half of the recording.

Figure 5.4: Photo of a station during the battery exchange. This opportunity was used to download the first six weeks of recorded data and to clear the memory on the cubes.

5.3 Data processing

All data processing was done on a Linux-based platform and involved several steps. Various short programs were written in c-shell to extract the necessary data and convert it to formats compatible with the various software used. The continuous data were viewed and processed manually for the arrival of seismic events. Events were then exported for P- and S-wave arrival time picking and hypocenter inversion. Next, coupled velocity model-hypocenter inversion was performed to obtain a velocity model for the study area, together with station corrections. Coupled inversion was performed iteratively with different starting parameters to arrive at a best velocity model. Seismic events were individually relocated using the final model to minimise the difference between observed and calculated travel times (time residuals). Finally amplitude data were extracted from maximum S-wave amplitudes and converted into local magnitude.

5.3.1 Event identification - PQL

The waveform data was viewed with PQLII (hereafter just PQL) . PQL was developed by the Program for Array Seismic Studies of the Continental Lithosphere (PASCAL). The program allows the user to view time-series data in a variety of formats, including MiniSEED. It does not have the capabilities to save P- and S-wave arrival times for individual stations and was thus just used to view the continuous data and build a database of arrival times of seismic events thought to be of tectonic origin.

Data were recorded continuously and these data were converted from cube format to MiniSEED format. The continuous data were cut into one hour-long-segments (Fig. 5.5) for ease of viewing and processing. All the hour long data files were manually scanned for the arrival of seismic events.

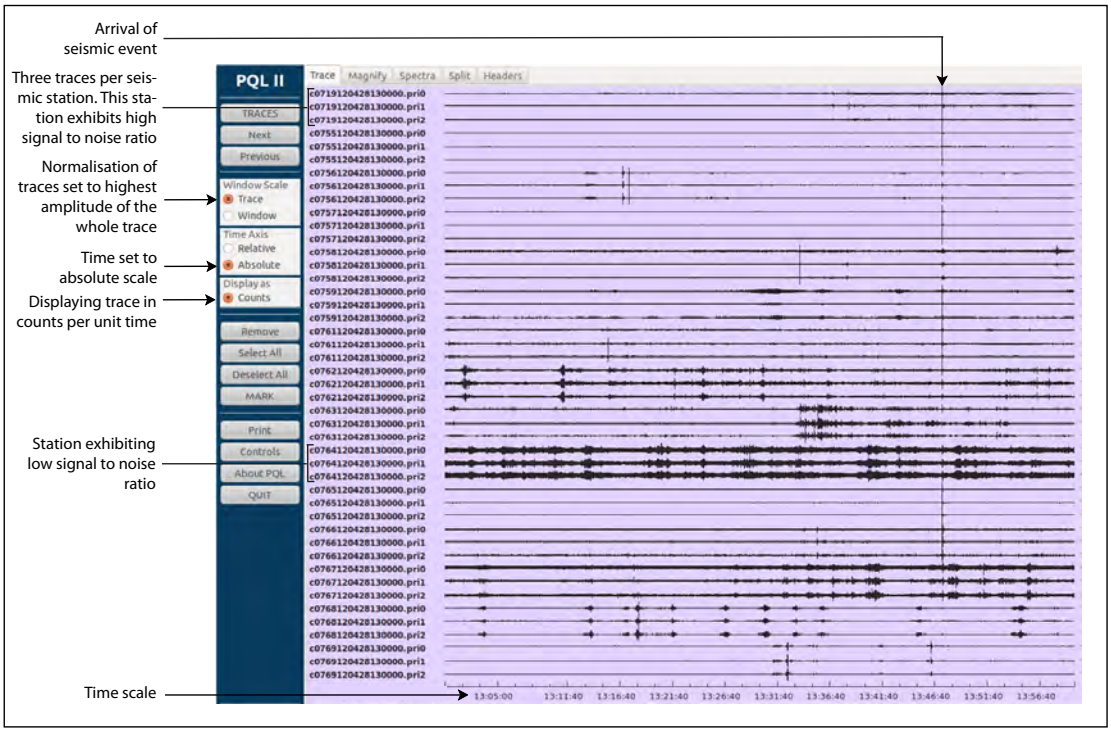

Figure 5.5: An hour-long recording of seismic data showing the arrival of a seismic event at roughly 13:47 local time on 28/04/2012. Different levels of background noise is visible on various stations.

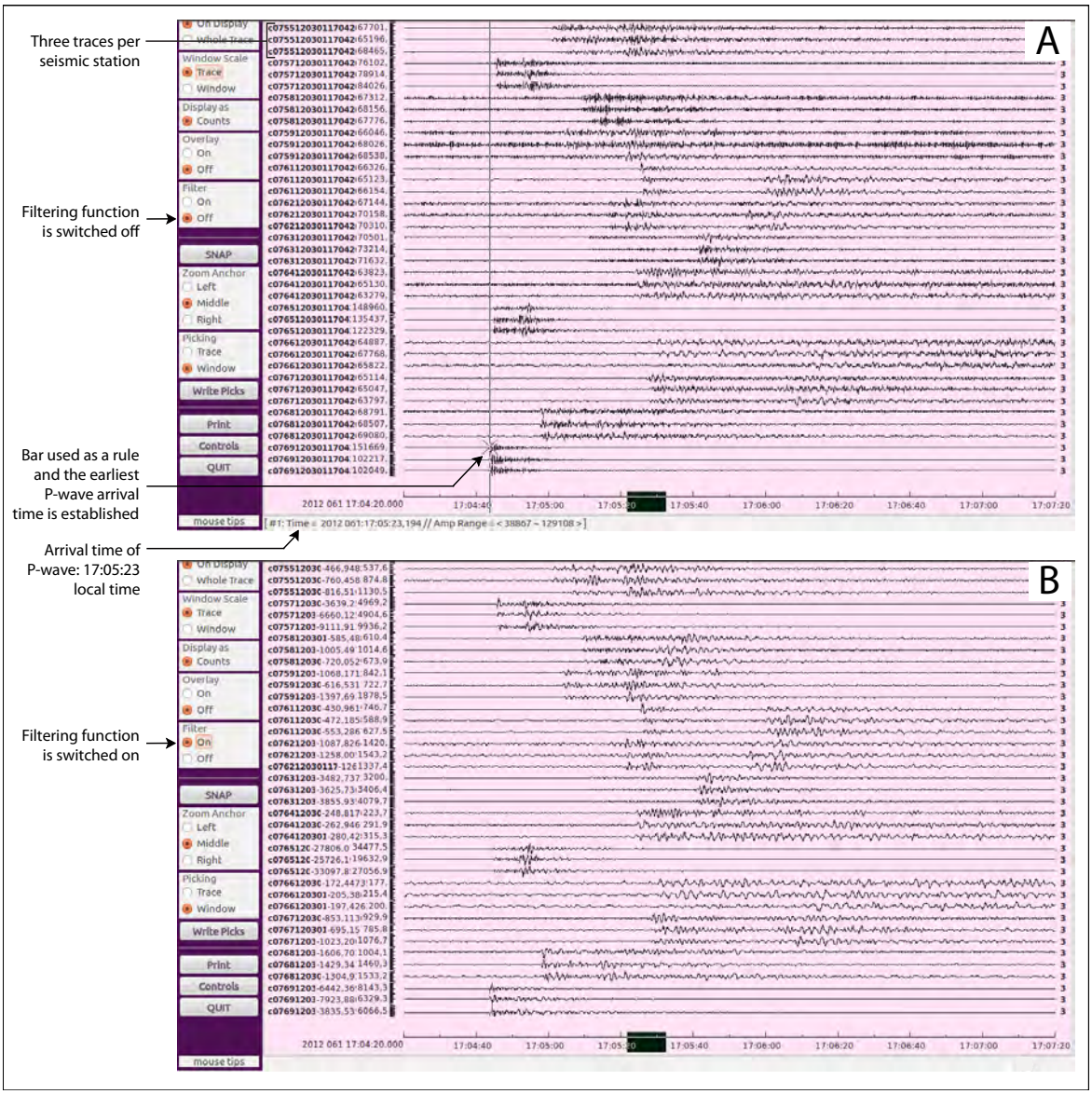

Figure 5.6: Zoomed in view of event in figure 5.5 with filter function turned off (A) and on (B). This view was used to establish the earliest arrival time of P-waves at the various stations (A). Bandpass filtering with a low- and high cut-off frequency of 1 and 20 Hz, respectively, was applied (B) where necessary to remove excess background noise for some events.

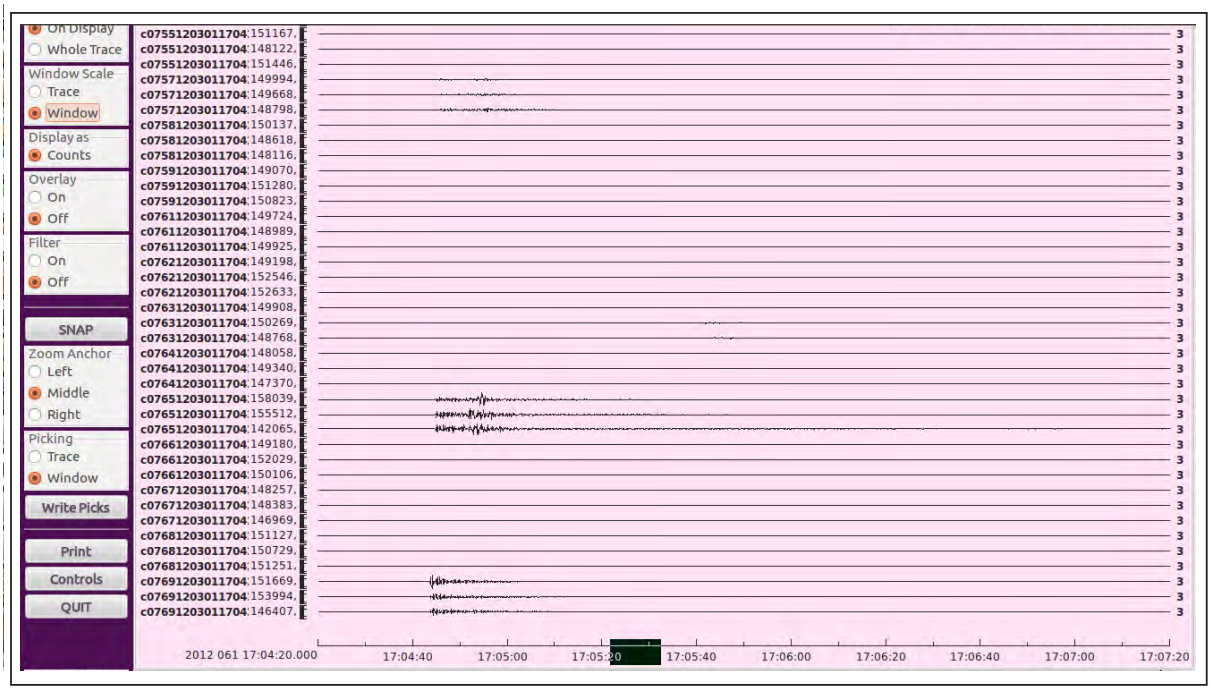

Figure 5.7: Zoomed in view of event in figure 5.5 with the trace amplitudes normalised to the highest trace in the viewing window. This view was not used as most of the traces are reduced to very low amplitude signal.

A few criteria were used to identify events for further consideration. (1) Traces of seismic events had to be recorded on a minimum of three stations. (2) Inside the array an initial P-wave velocity estimate of 5 km/s was used based on the average P-wave velocity for sandstone at the surface (Stankiewicz *et al.*, 2007). The maximum dimension of the array is roughly 40 km. Thus the maximum difference in arrival time of P-waves from one event at different stations could not be more than 8 seconds. (3) Using an average of 8 km for every second of difference in P- and S-wave arrival time (P-S time) of the same event, the P-S time for each station could not be much greater than 5 s. (4) The arrival of seismic waves had to be distinguishable above the background noise. These criteria are not necessarily proof that the events were indeed of tectonic origin, but served as a minimum basis before selecting events for further processing.

The software has a bandpass filtering function that allows frequencies between a low- and high cut-off limit to be viewed while blocking frequencies not in this range (Fig. 5.6). Bandpass filtering of 1-20 Hz was applied in PQL to remove high and low frequency noise when signal

to noise ratio was low.There was varying levels of noise from one event to another (Fig 5.8). When an event was identified in the data, the earliest P-wave arrival time was noted. Only stations with high signal to noise ratios were used to establish arrival time of seismic events. The trace amplitudes in PQL were normalised to the trace with the largest amplitude currently in the viewing window as opposed to normalised to the largest amplitude on the whole trace.

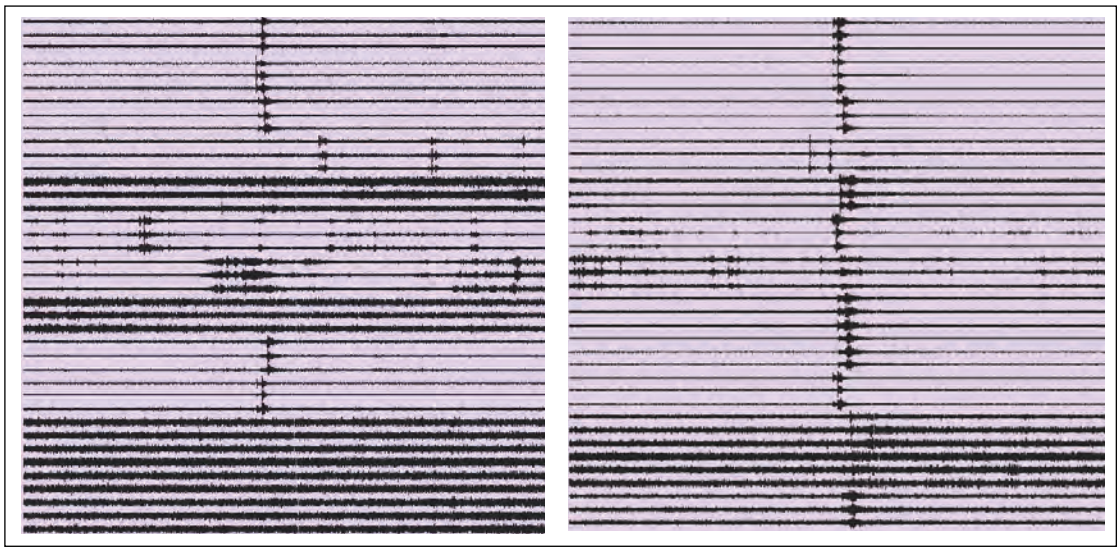

Figure 5.8: Three minute view of two events showing low (left) and high (right) signal to noise ratio. Note how the seismogram on the right shows the arrival of the event on more stations than the seismogram on the left. Both events are unfiltered.

After viewing all data, the arrival time database contained 351 events. A short program was written that took the starting time of all the identified events to copy three minute time sections from the raw cube format data for each arrival time. The three minute event files started one minute before the earliest P-wave arrival of each event. These event files were converted into a format compatible with the software (xQuake) used for P- and S-wave arrival time picking (phase picking). Even though stations with low signal to noise ratios weren't always used in PQL, all stations were included in the three minute event file data set for phase picking.

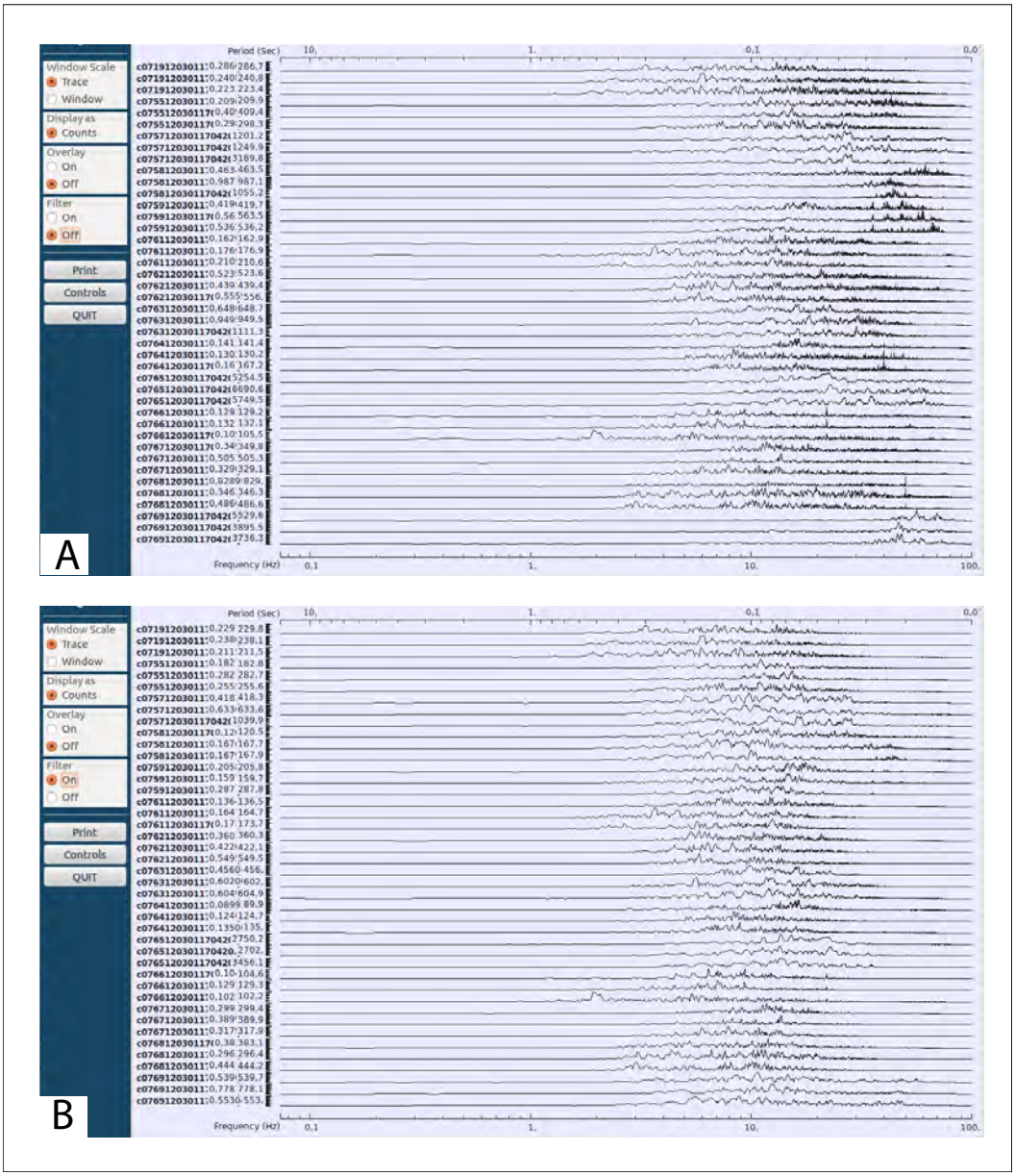

Figure 5.9: The spectral range of the seismic event shown in figure 5.5. The broadest range of spectra was in the range of 10-20 Hz although there are some events in the data set which exhibited spectra at frequencies as low as 1 Hz and as high as 40 Hz. Figure A shows a raw unfiltered view of the spectra while figure B shows the spectra after filtering between 1 and 20 Hz.

5.3.2 Hypocenter location - xQuake

The software xQuake was used to pick the arrival times of P- and S-wave phases (Fig. 5.10). It was developed by Dr Christian Haberland from the GFZ. It allows the user to pick and save

the arrival times of incident P- and S-waves at each station for each event. P-wave arrival time was picked on the vertical axis while S-wave arrival time was picked on the horizontal components. HYPO71 was used as a plug-in by xQuake to calculate the ray paths that fit the observed travel time and invert the travel times for hypocenter location.

Some of the hypocenters plotted outside of the array. For the purposes of this study, events that plotted inside the array were termed local events, and events plotting outside were termed regional. For the purposes of final hypocenter location, only local events will be considered. A variable that was used as a quality control was the azimuthal gap (hereafter just gap). The gap of an event is defined as the largest azimuth between any two stations that observed the seismic event with a gap of more than 180° implying that all stations were to one side of the event (Havskov and Ottemöller, 2010).

If an event was located during data processing with gap $< 180°$, it was automatically included in the hypocenter database. Events with $181° <$ gap $< 210°$ were relocated using the final velocity model. If the gap of an event decreased to less than 180° after relocation, the event was added to the hypocenter database. Events with gap $> 180°$ after relocation were not used for hypocenter plots.

Arrival of seismic waves must also have been recorded and picked on more than three stations to classify as a seismic event and to be included for hypocenter location. Bandpass filtering made it possible to identify the arrival of P- and S-phases where ambient noise levels are high. Different ranges of filtering were used for different events, depending on the noise frequencies. Filter ranges used include 1-40, 1-20, 10-40 and 20-40 Hz, with 1-20 Hz being used most frequently.

Stations show varying degrees of signal to noise for the same event. This can be seen when comparing figures 5.10 and 5.11A which are recordings from two stations of the same event. The seismic trace recorded on station number 14 (Fig. 5.11) is obscured by background noise while that of station 09 (Fig. 5.10) show very high signal to noise ratio. Bandpass filtering was applied to eliminate high levels of background noise (Fig. 5.11B). Filtering cleared up the traces and made it possible to pick arrival times more accurately and at more stations than without filtering. It was not necessary to apply filtering to all the stations for a specific event, as can be seen from the example above.

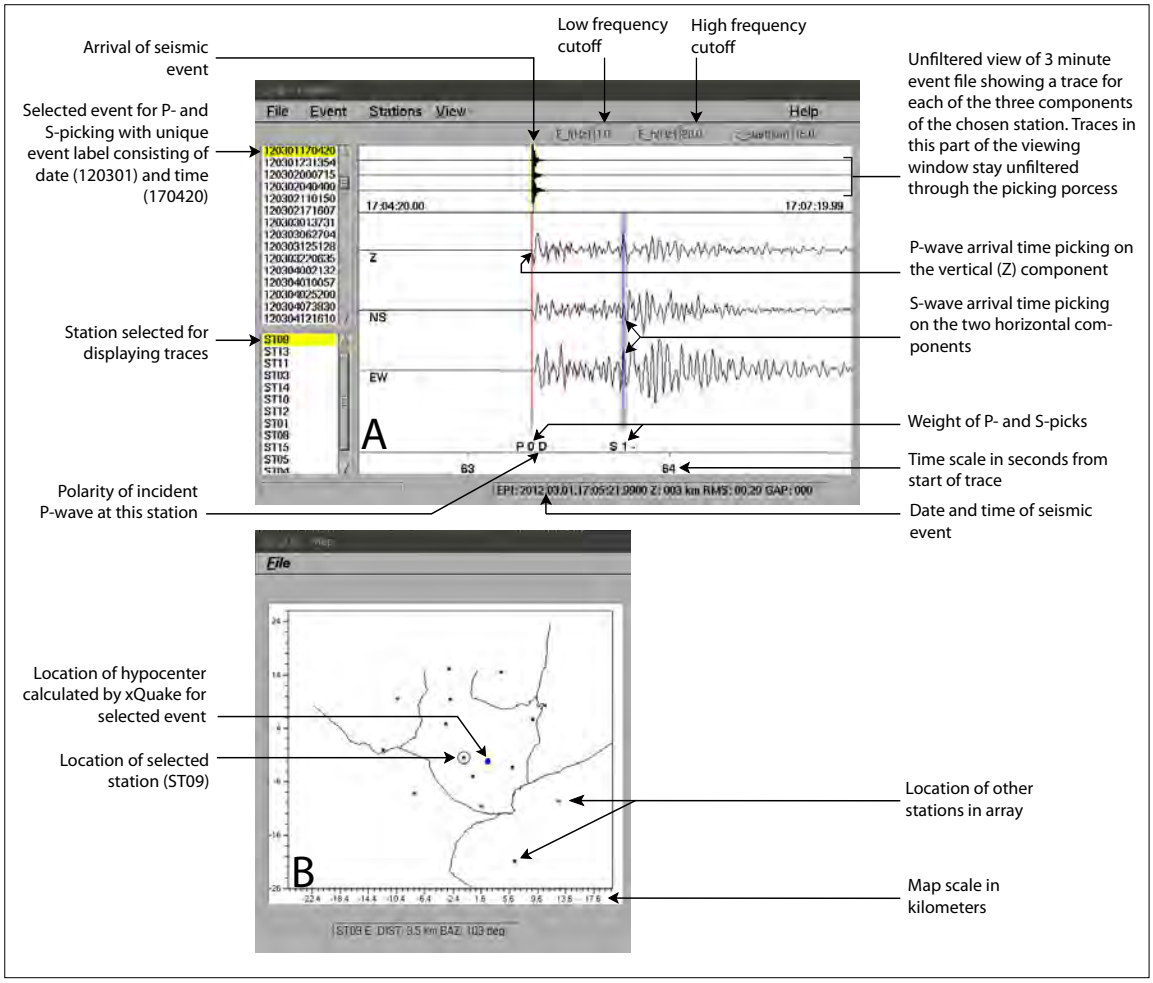

Figure 5.10: An example of a seismic event viewed in xQuake. In figure A the unfiltered seismic trace can be seen in the very top of the display window. The main display window contains a zoomed in imaged of the trace on which waveform arrival time picking is done. The hypocenter location for the event is displayed on figure B with a circle around the station that is currently displaying the waveform, in this case station 09. The other stations of the array are indicated by stars.

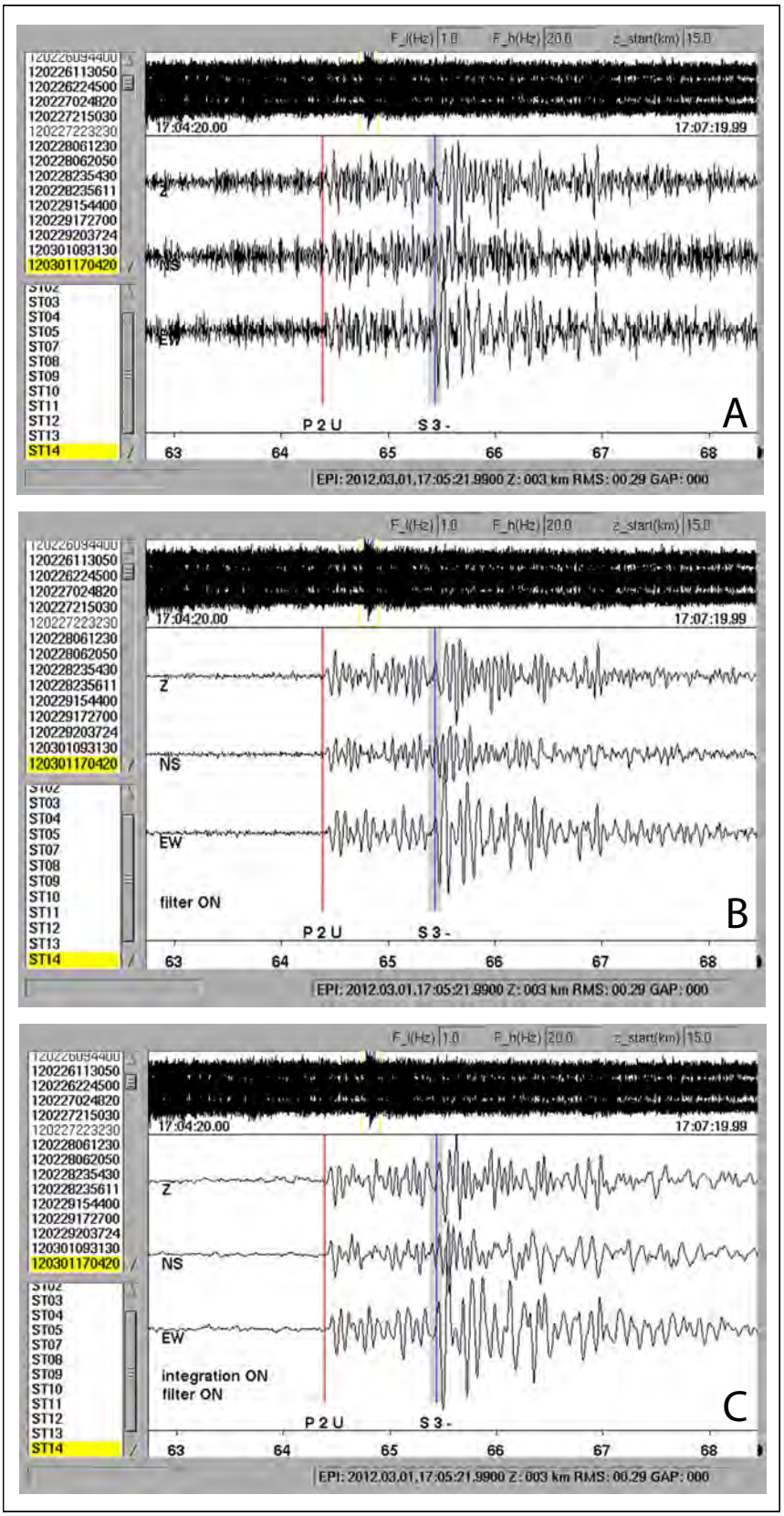

Figure 5.11: An example of a seismic event with high levels of background noise in which the P- and S-arrivals aren't clear (A). The filter function is applied in figure B with a low and high cut off limit set at 1 and 20 Hz, respectively. After filtering the waveform appears much clearer. Integration from the time to the displacement domain is applied in figure C which is used exclusively as an aid for S-picking. Note that the arrival of the S-wave can be seen more clearly in figure C relative to figure B.

Arrival times are weighted relative to the accuracy of the picks. A weight of zero is assigned to a pick with virtually no background noise (Fig. 5.10) and the arrival of P-waves can unambiguously be seen on the waveform. When filtering was applied a minimum weight of 1 was assigned to the pick. When integration was needed for an S-pick, a minimum weight of 2 was assigned to the pick. A weight of 3 was used when filtering and integration was used and background levels were still high enough to inhibit accurate picks. Where filtering and integration still cannot reveal the arrival of waveform above the background noise, but the relative position of the waveform is known from other picks, a weight of 4 was used.

Picks with a weight of 4 are not included in the inversion. However, it is useful to see how close the synthetic picks are relative to picks with weight equal to 4. If there is a small time difference and there is an incident waveform discernible in the noise the weight can be dropped to 3 to include the pick in the hypocenter calculation. The more picks there are the more robust the hypocenter location. And the more S-picks there are the more robust is the depth component of the calculation.

When all the visible P- and S-wave arrival times have been picked on all stations for a particular event, arrival times are inverted for hypocenter location in xQuake using HYPO71 (Fig. 5.10B). Synthetic picks are produced by xQuake based on the calculated arrival time for that station that minimises the time residual, i.e. the difference between observed and calculated travel times. Ideally the manual and synthetic picks should be very close to one another in time. Events with low noise levels usually showed the least difference between manual and synthetic picks.

One of the aims of the project was to produce focal mechanisms for some of the larger events. In order to define the compressional and tensional regions (P and T axes) in the focal sphere an event needed to be recorded by all or most stations in the array. For this the polarity (Fig. 5.10A) of the P-wave on the trace, i.e. up or down on the vertical component, was also saved along with the picks for potential focal mechanism derivation. A short list of events were compiled which could potentially be used for focal mechanism inversion.

When the whole database of three minute event files were picked, all the picks, together with the hypocenter locations and travel times, were exported to a new file which is in a compatible format with the software used in the next step of data processing which is

coupled hypocenter-velocity model inversion.

5.3.3 Coupled inversion - VELEST

A one dimensional (1D) velocity model is used to compute the possible ray paths and determine hypocenter locations for local earthquakes. Due to the intensive computational time involved, high data quality and long observational period required for three dimensional (3D) tomography it is not always possible to calculate a 3D velocity model (Husen *et al.*, 2011). Midzi *et al.* (2010) calculated an average 1D velocity model for South Africa. However, they state that different models should be used for the different tectonic provinces of South Africa. As there is no velocity model for the Ceres region, one was derived with the Ceres data by the simultaneous inversion of initial hypocenter locations (from xQuake) and travel times.

Coupled velocity-hypocenter inversion was performed using the software package VELEST. It was developed by Kissling (1995) and is used to produce a one dimensional (1D) velocity model (Fig. 5.12). The software inverts the observed travel times of seismic waves for all events in the database simultaneously, calculates the possible ray paths of seismic waves based on observed travel times for hypocenter locations while simultaneously solving for phase velocity within predetermined layers below the array. Thus there is a strong coupling between hypocenter location and seismic velocity during the inversion process.

The model needs a thin surface layer to compensate for topographical differences in station locations. In this case it was set 1 to 0 km above mean sea level, because the maximum topographical difference between stations for this study was 900 m above mean sea level. During the initial inversions with batch 1 of the data, the starting velocity, velocity increase, number of layers and layer thickness starting parameters were experimented with to get reasonable values that result in low scatter between the 36 models calculated for each inversion. Since VELEST does not automatically adjust layer thickness (as opposed to layer velocities), the appropriate layering of the model must be found by a trial-and-error process. Thus the calculation of a Minimum 1-D model normally starts with finding an appropriate model layering (Kissling, 1995). The parameter values that showed the least amount of scatter were saved and used again after the data from batch 1 and 2 were concatenated into a single file.

A total of 29 coupled inversions were performed with different starting parameters. There were initially six velocity layers which was increased to seven as the behavior of the model to changing parameters was observed. The parameter values of the velocity model which showed the least scatter of all possible models during a particular inversion were carried through to the next inversion. The choice to keep one parameter versus another, and thus one model versus the other, were based on the depth error in hypocenter location, difference between observed and calculated travel time (time residuals) and RMS values produced by VELEST.

The starting velocity for the final model was 4 km/s increasing by a factor of 0.4 for each iteration. The starting velocity increase per layer for the final model was set to 0.035 increasing by a factor of 0.02 for each iteration. A short program was written containing a loop that first changed the starting velocity then velocity increase six times each during every inversion, resulting in 36 possible velocity models per inversion. The inversion with the lowest RMS value was selected as the best model for each inversion as is shown as a red line on figure 5.12.

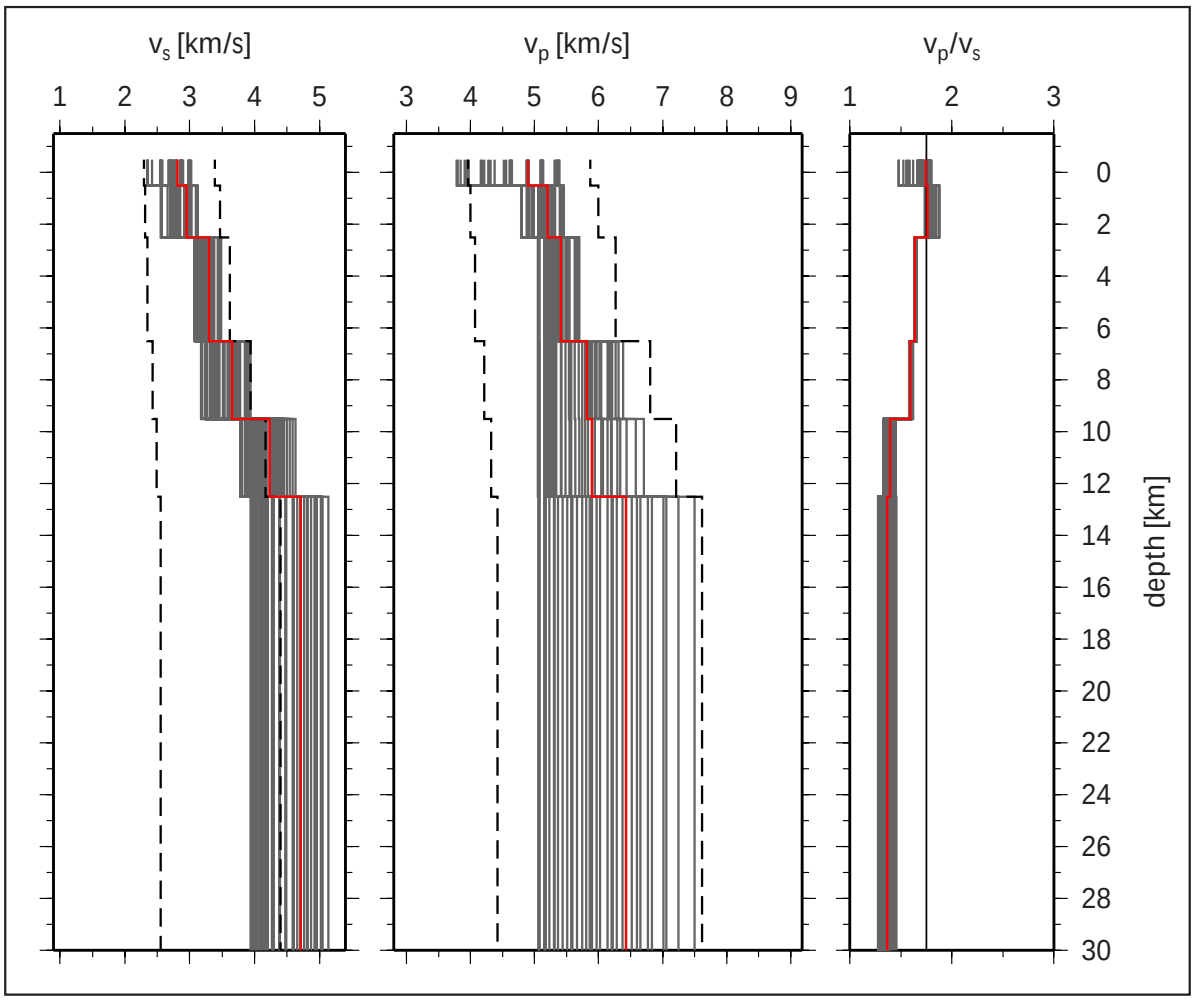

Figure 5.12: Final velocity model produced by VELEST for V_p (center), V_s (left) and V_p/V_s (right) for the Ceres data. There are a total of 36 iterations (solid grey lines) for each inversion with the model containing the lowest RMS value shown in red. The upper and lower limits of the starting velocity and velocity change values are shown by dashed lines. Every velocity increase, or step, in the model is a specific chosen layer thickness. The lowermost layer (between 12 and 30 km) is not well constrained due to a lack of events in this depth.

59 events recorded on a minimum of 6 stations were used in the final coupled inversion. These events all had a gap < 180. After the model was calculated, another 109 events recorded on 3 or more stations with gap $< 220°$ were added to the database for single mode relocation of individual hypocenters. This dataset of 172 relocated events make up the hypocenter locations that are plotted in figure 6.3.

5.3.4 Magnitude

M_L values for the Ceres-Tulbagh region were empirically derived for the 172 events used for hypocenter location during this study. Waveforms were integrated to the displacement domain and filtered with a low-pass filter of 1Hz and a high-pass filter of 40 Hz. Waveforms were then normalised to the S-picks and plotted against epicentral distance (Fig. 5.13). Maximum amplitude values (A) on the horizontal components (*i.e.* S-wave amplitude) of the waveforms were taken for each event and plotted against epicentral distance (Fig. 5.13). The maximum average displacement was obtained by summing the square root on the component with the higher amplitude and the square of the amplitude on the component with the lower amplitude. This gave an average S-wave amplitude for each station. The average of the three highest amplitudes was taken as the representative amplitude for each event to avoid the effect of possible amplitude outliers.

The amplitude values were converted to magnitude values using the equation

$$M_L = \log(A) + x * \log(r) + y(r) + z \tag{5.1}$$

where A is calculated amplitude, x is geometrical spreading, y is attenuation, z is a base level correction factor and r is epicentral distance (Havskov and Ottemöller, 2010).

The magnitude scale for this study was calibrated to an M_L 2.4 event (Fig. 5.14) that occurred offshore of the west coast of South Africa at 14:21:03 on 11 March 2012. This event was recorded by the CGS who also calculated the magnitude, as well as the temporary Ceres array. An M_L scale with local correction factors for South Africa was recently developed by Saunders *et al.* (2013) which yielded x=0.014 and y=0.00069.

The frequency distribution and the cumulative frequency was plotted for the data (Fig. 6.7) as well as the distribution of magnitude versus depth (Fig. 6.4). This will be further discussed in chapters 6 and 7.

The reason that the above mentioned event was chosen for calibrating our magnitude scale is that it was recorded by the CGS and used during their magnitude scale calibration (Saunders

et al., 2013), and it was also recorded by our temporary seismic array. Due to the small magnitude of events recorded during this study there were no events that was recorded by the CGS that fell in the boundary of our array. The fact that we are calibrating our scale for microseismic events in a range of 0 to 30 km to an event more than 100 km away is not ideal, as magnitude calculation is strongly dependent on epicentral distance. However, a base level correction factor (z) of -3 proved optimal for relating the two scales, and even though the absolute value of our scale may be off, the relative values still holds and the magnitude distribution approximates a Gutenberg-Richter distribution (Fig. 6.7).

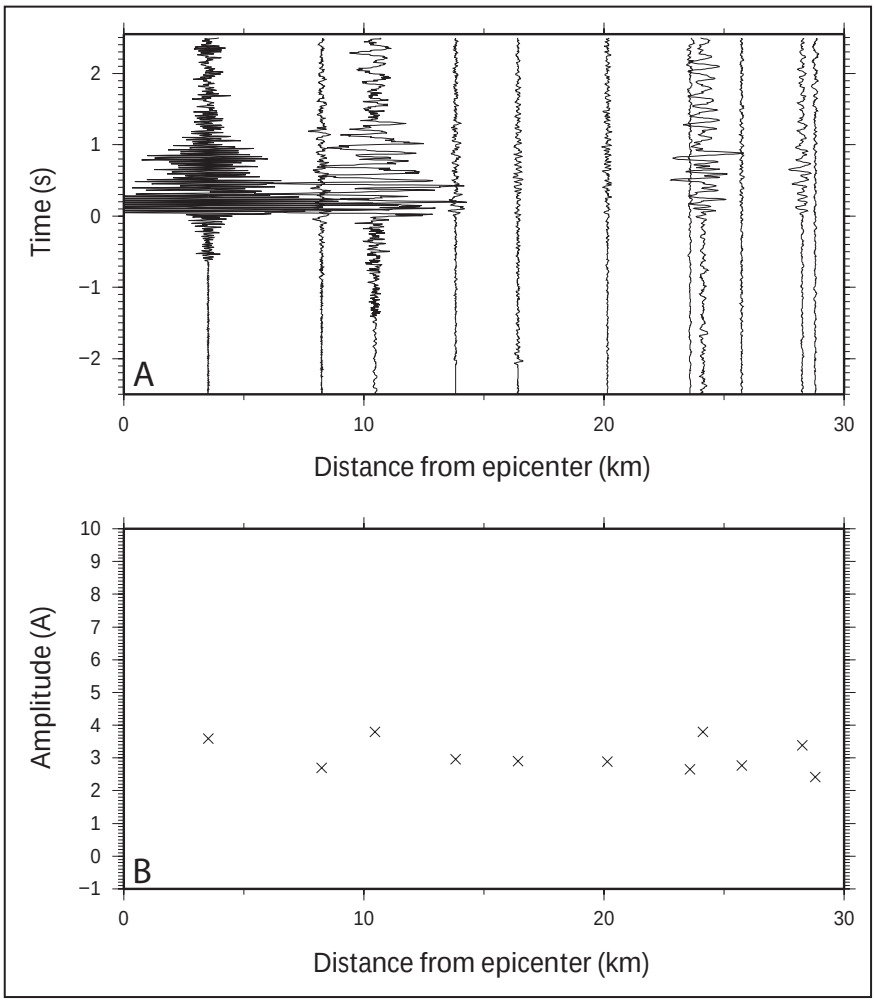

Figure 5.13: Example of an event which shows plot of time (top) and amplitude (bottom) against epicentral distance with the time plots normalised to the S-wave picks. The amplitude values of events were extracted from the values of the bottom figure and used in magnitude calculations.

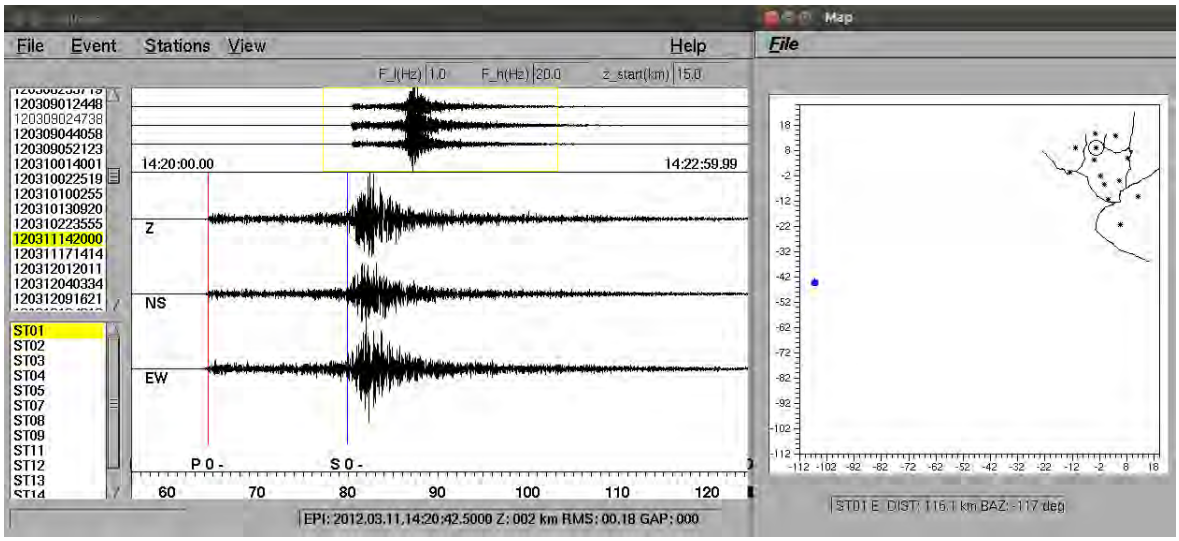

Figure 5.14: M_L 2.4 event that was recorded by the temporary Ceres array and which was used to calibrate the calculated magnitudes for this study.

Chapter 6

Results and observations

The results for this experiment are derived from the 172 microseisseismic events recorded during 2012 that occurred within the boundaries of the temporary seismic array after relocation. Figures 6.2 and 6.3 were plotted using GMT.

6.1 Velocity model

The calculated one dimensional (1D) velocity model does not account for lateral structural heterogeneities. Three dimensional tomography calculations were beyond the scope of this project due to not enough data from few stations and short recording time. The reason for using a 1D model is to achieve a simplistic model with which to locate hypocenters. There is a strong coupling between the velocity model and hypocenter location and an inaccurate model will result in inaccurate hypocenter locations. The velocity model needs to represent a global minimum for the data and not a local minimum which will represent a false model. Thus multiple coupled hypocenter-velocity inversions were performed with different starting parameters to obtain a model which represents the global minima for the data.

The velocity model is based on 59 events that were recorded on six or more stations, have a gap of less than 180° and thus have hypocenter locations with minimal time residual and RMS values. It showed the least amount of scatter in the calculated V_p and V_s values relative

to the other 29 inversions and has an RMS value of 0.054 s. The average RMS value for each individual event used in the inversion is 0.044 s.

The model shows an increase in V_p from roughly 4.9 km/s at the surface to 6.4 km/s at a depth of 12 km. V_s values range from 2.8 to 4.7 km/s from the surface down to 12 km, respectively. V_p/V_s decreases from 1.7 at the surface to 1.5 at 12 km depth. Due to the sparse distribution of events below 12 km this layer is not well constrained and not represented in the velocity model.

There is a strong coupling between the increase in velocity and the chosen layer thickness for the model. The step-wise increase in velocity shown in figure 6.1 is a function of the velocity layers that were used as input for the model.

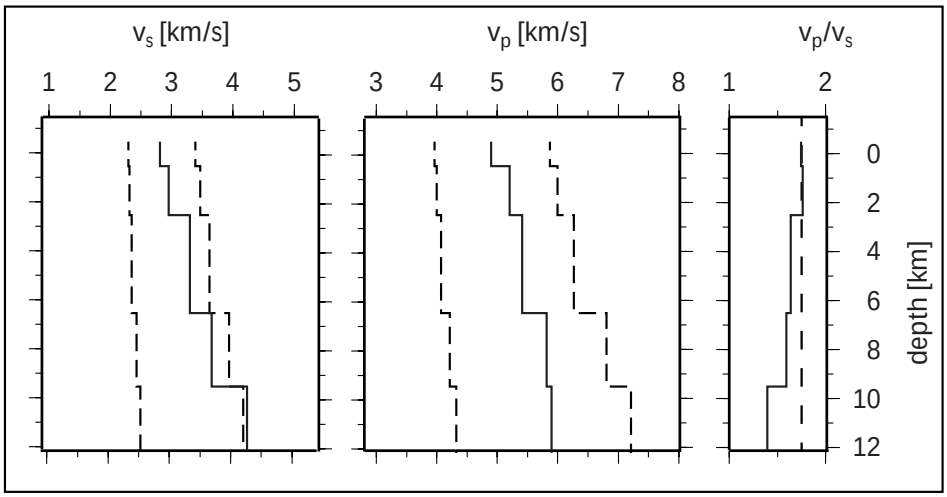

Figure 6.1: Final velocity model for V_S, V_P and V_P/V_S (solid lines) based on 59 events with a well constrained location error. The dashed lines represent the starting input parameters used during coupled inversion.

6.2 Station corrections

The reference station (ST12) was chosen on the basis of having recorded most of the seismic events in the data set and having high signal to noise ratio resulting in accurate picks. The reference station does not display any station correction and thus all corrections are relative

to this station. A positive correction means that seismic waves arrive at the station later than expected and a negative correction means that waves arrive earlier than what is predicted by the model based on calculated arrival times produced by VELEST.

Station corrections for P- and S-waves range from 0.14 to -0.33 s and 0.17 to -0.79 s, respectively. The absolute value of average stations corrections for P- and S-waves are 0.13 and 0.32 s respectively.

There is a notable structure to the corrections (Fig 6.2) with positive and negative P-wave corrections confined to the north eastern and south western parts, respectively, of the study area. The S-wave corrections show a similar trend but with larger corrections in general and less positive corrections than P-waves.

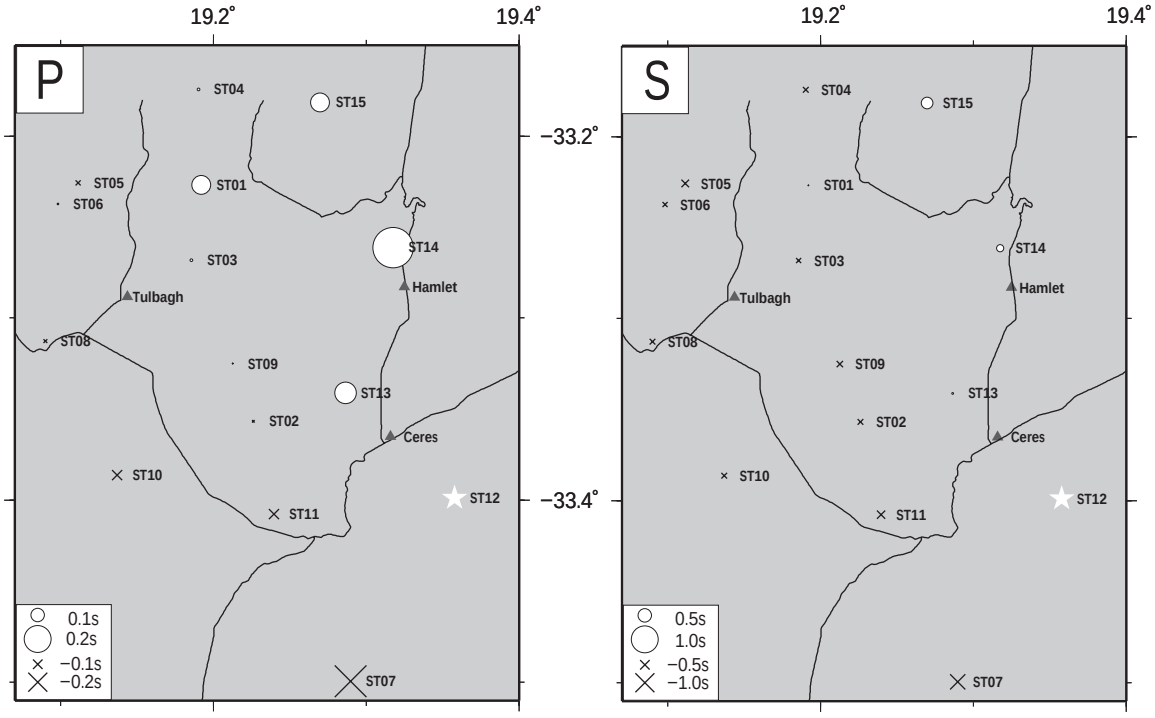

Figure 6.2: Station corrections for the array based on the same 59 events from the final velocity model. Station 12 (white star) was used as the reference station. The P-wave corrections (left) show roughly equal positive and negative corrections while S-wave corrections are mostly negative. The spread of positive and negative corrections for P-waves may hint at a structural discontinuity. The larger S-wave corrections may be attributed to higher noise levels surrounding S-waves than P-waves.

6.3 Hypocenter locations

The locations of 172 events recorded on three or more stations with an azimuthal gap of less than 180° are shown in figure 6.3. Only events with a gap <180° (59) were used for coupled inversion. Events with 180°<gap<210° (109) were relocated using the calculated velocity model. The locations of the 59 velocity model events were plotted and compared with the locations of the events with a higher gap. No inconsistencies were noted in the distribution of the hypocenters and thus the 109 relocated events were included in the data set.

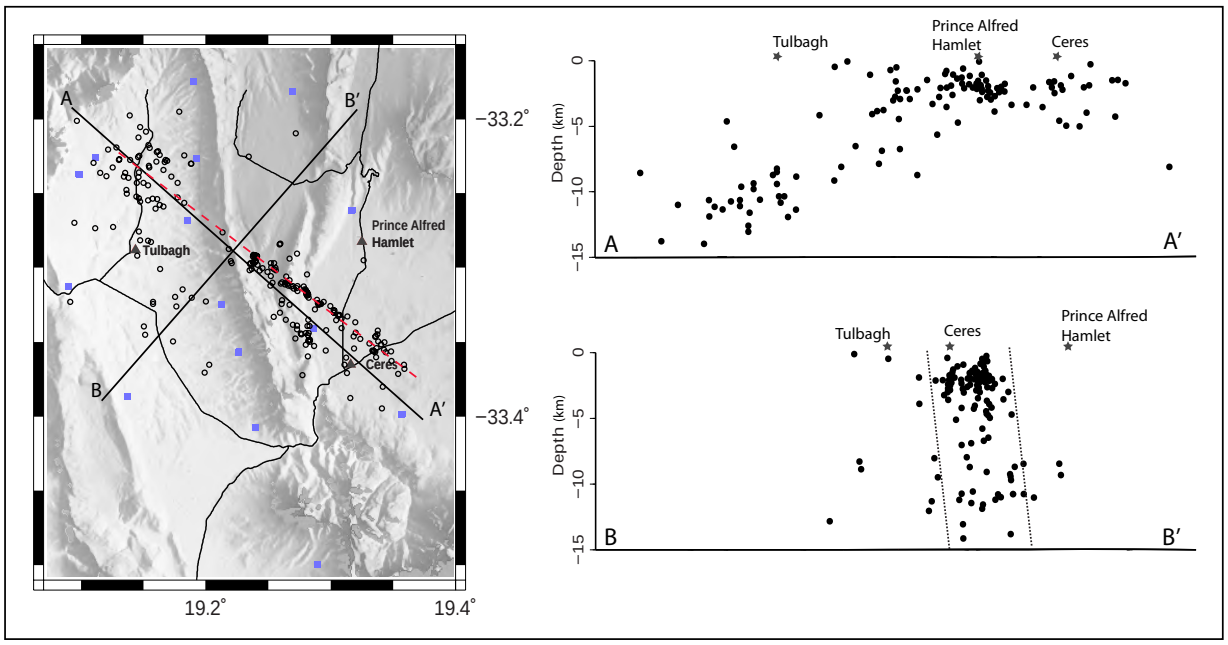

Figure 6.3: Final hypocenter locations (open circles on map view) of 172 local microseismic events and position of seismic stations (squares) overlain on topography with depth projections along A-A' and B-B'. The red dashed line represents the visual best fit trace of seismic activity used in figure 6.5. Note (1) the general NW-SE orientation of seismic activity (2) the clustering of and lateral discontinuity of hypocenter locations on the map view (3) a cluster of shallow seismicity 0 - 5 km deep below Ceres and Hamlet when viewed along A-A', (4) the deeper cluster of seismicity roughly 9 - 15 km north west long the fault zone when viewed along A-A' (5) the depth clustering is also visible when viewed along B-B' and (6) the sub-vertical structure of the fault zone when viewed along B-B'.

The distribution of microseismicity generally follows the same trend as the aftershocks (Figs.3.5 and 6.5) of the 1969 Ceres earthquakes recorded by Green and Bloch (1971), although there is

a difference in strike of roughly 7° azimuth. Neither the microseismic zone nor the aftershock zone show a clear correlation to previously mapped fault surface traces.

Seismic activity defines a sub-vertical fault zone (Fig. **??**) with a general NW - SE orientation that cross-cuts the existing topography in the region (Fig. 6.3 map view). The fault zone is roughly 5 -10 km wide (Fig. 6.3 B-B') and seismicity occurs to roughly 15 km depth.

There is a high concentration of events surrounding and north west of Ceres followed by a lateral discontinuity of roughly 5 km in the distribution of hypocenters along strike of the fault zone directly east of Tulbagh. Another concentration of hypocenters is present directly north of Tulbagh. The distribution defines two clusters of seismic activity, here after referred to as the Ceres and Tulbagh clusters.

A similar discontinuity exists in the depth distribution (Fig. 6.3 A-A' and B-B'). Seismicity occurs from 0 to roughly 9 km depth below and north-west of Ceres with very few events in the 5 to 9 km range. Seismic activity in the Tulbagh cluster ranges from 4 to 15 km with very few events in the 4 to 9 km range. The frequency-depth distribution (Fig. 6.4) of microseismic events show a similar bimodal distribution of events with depth. There is a high concentration of events in the upper 5 km with a peak at 3 km. Another smaller peak can be observed at 11 km depth with sparse events at 7 km. Unfortunately, no errors in location values are produced by VELEST.

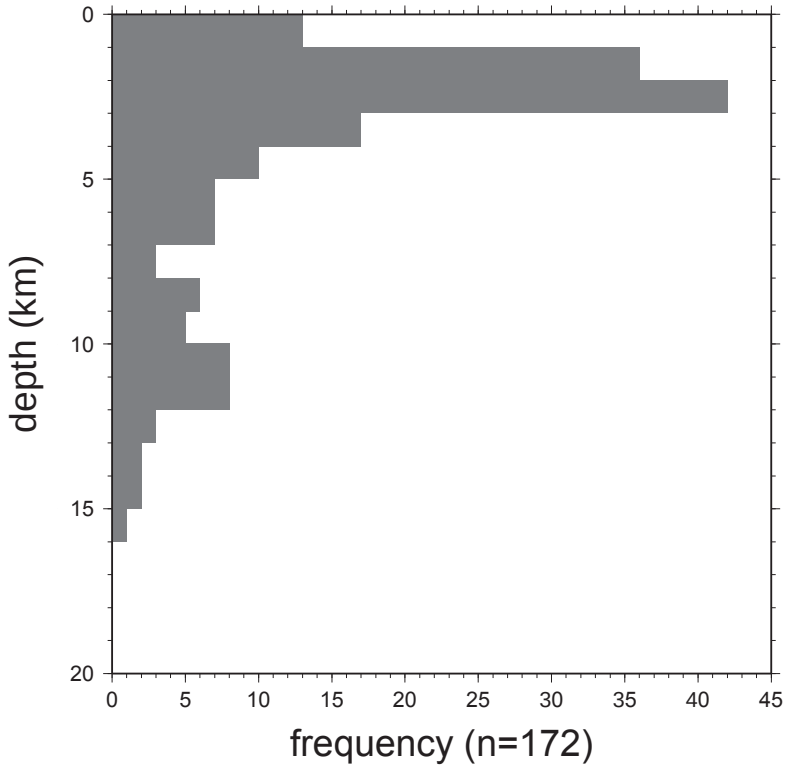

Figure 6.4: The depth distribution of seismic events in Ceres shows that the majority of the events occur in the top 5 km, which corresponds to the shallow events below Hamlet and Ceres (as seen on Fig. 6.3 A-A'). There is a small peak in the histogram at 10-12 km depth, which corresponds to the deeper events north of Tulbagh.

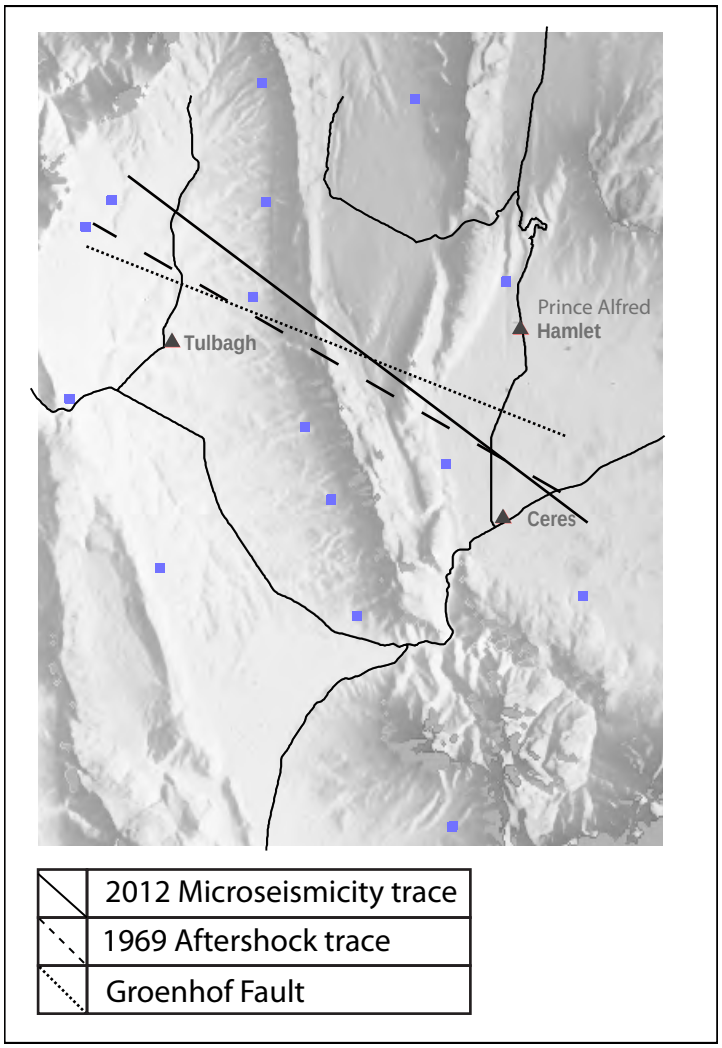

Figure 6.5: The orientation of the best fit lines delimiting the microseismic activity does not match up exactly with the distribution of the 1969 aftershocks, or the Groenhof Fault. The angle between the zone of microseismicity and the Groenhof fault is roughly 15°, and the angle between the zone of microseismicity and the aftershock zone is roughly 7°, while the difference between the aftershock zone and the Groenhof fault is roughly 8°.

Generally, the background noise levels were relatively high and signal to noise ratio for most events were relatively low. Picks done with high levels of background noise carry weight reflecting the confidence in the pick. Uncertainty in the velocity model and the location of seismic events result from inaccurate picks. However there are events that were recorded with high signal to noise and arrivals were picked with high confidence. These add to confidence of the velocity model and the hypocenter locations.

The temporal distribution of seismic activity (Fig. 6.6) is polymodal on a daily scale with multiple peaks of activity followed by short periods of reduced to no activity one or two days long. In the whole recording time of the experiment there are a total of 15 days in which no seismic activity was recorded. The highest number of events per day was 6. On average there was 1.8 microseisms per day.

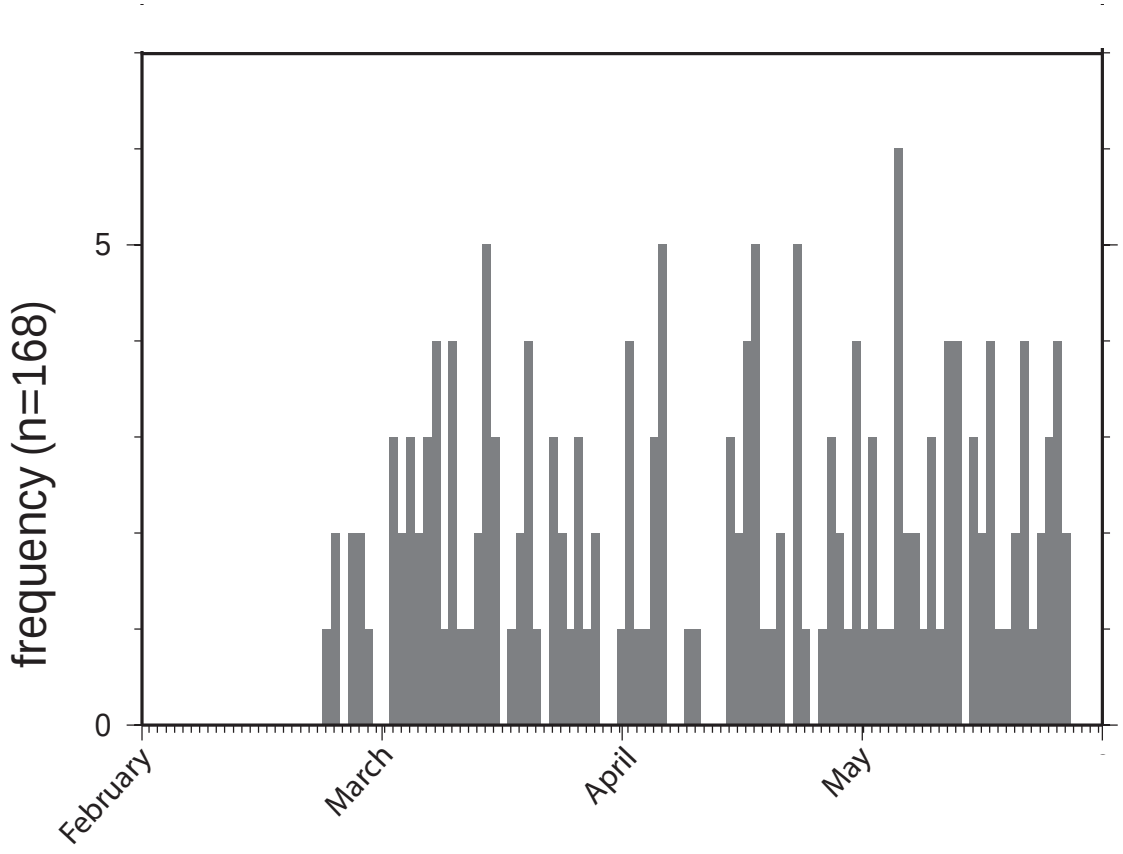

Figure 6.6: The frequency of seismic events on a daily scale during the recording time of 21 February to 25 May 2012.

6.4 Magnitude

Calculated magnitude values range from -2.2 < M_L < 1.6 with a magnitude of completeness of M_c = -1.5. The majority of events are in the -1.5 < M_L < -1.0 range (Fig. 6.7A). A Gutenberg-Richter b-value of 0.9 was calculated for the cumulative frequency distribution (Fig. 6.7B).

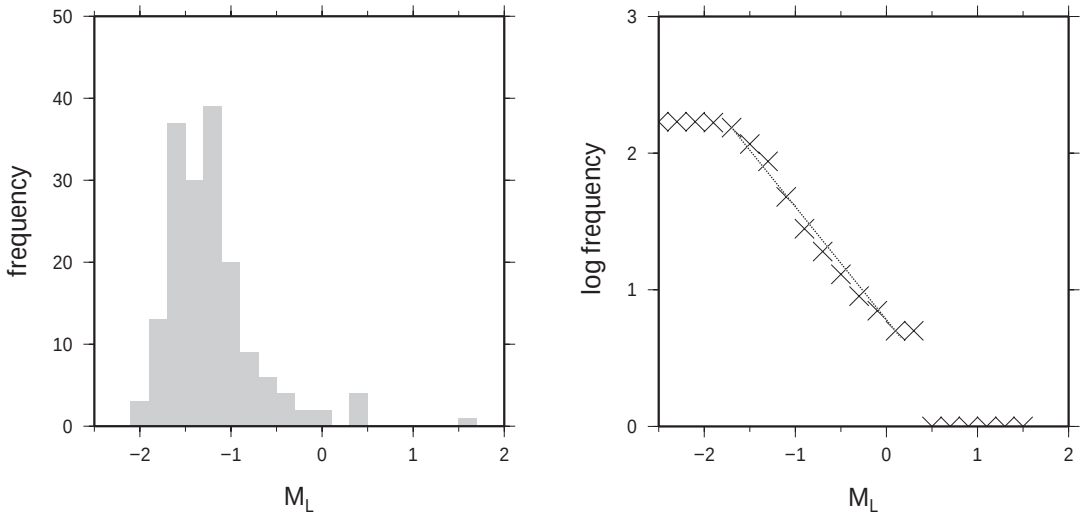

Figure 6.7: Histogram showing the distribution of calculated magnitudes with a magnitude of completeness of approximately M_L -1.6 (left) and cumulative frequency plot (right) from which a Gutenberg-Richter b-value of 0.9 has been calculated between the falloff curves of the cumulative plot (dashed line).

Chapter 7

Discussion

The manual processing of seismic data led to the first local velocity model and station corrections for the Ceres region and enabled the identification of a microseismically active fault zone that closely match the strike of the 1969-1970 aftershock plane from Green and Bloch (1971). Empirically determined local magnitude (M_L) values were derived from an event of known magnitude. The maximum depth of the microseismic activity (15 km) is interpreted as the base of the seismogenic zone, at least on the time-scale of this study.

In this chapter I aim to compare the observed seismic activity to other regions in terms of magnitude, detection limit and the depth of the seismogenic zone. An attempt is made to relate the intraplate microseismicity in Ceres to plate boundary forces acting on the African plate.

7.1 Waveforms

All stations were installed on private farm land. The activity on farms, such as tractors moving about, the use of heavy machinery and water pumps, are likely sources of noise. Some stations, for example stations 08 and 14 (Fig. 5.1) were located close to regional roads on which heavy vehicles transport goods, such as fruit grown in the area. These vehicles may also have contributed to high levels of background noise for the stations located in close

proximity to roads although such proximity was largely avoided while installing the stations. The amplitude of ambient noise determines the minimum amplitude of seismic waves that can be identified in the data. Manual processing of seismic data was an integral part of this project. Thus, a great effort was made to recognise events at as many stations as possible.

By filtering the waveforms there was always the possibility of losing data, and it may be that the arrival of some phases were filtered out and thus not picked. It also happened that filtering and integration did not sufficiently clear up some traces and waveforms were not picked on these traces. In general, S-wave arrivals were associated with higher levels of noise than P-waves. One source of noise surrounding S-waves could originate from the scattering of P-coda thus making it more difficult to determine.

7.2 Velocity model

The 1D velocity model (Fig. 5.12) presented in chapter 6 is the first local velocity model derived for the Ceres region. Microseisms occur down to a depth of 15 km but due to the sparse distribution of events between 12 and 15 km the final model was only calculated to a depth of 12 km. It predicts V_p and V_s of 4.8 to 5.9 km/s and 2.8 to 4.2 km/s , respectively, from the surface down to 12 km.

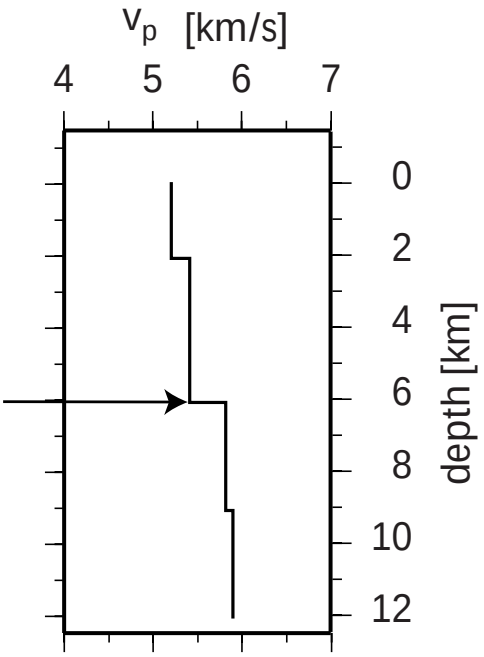

Figure 7.1: There is a change in V_p at the 6 km layer (arrow) from 5.4 km/s to 5.8 km/s which is relatively large in comparison to the changes in the layers above and below. This change occurs within the 2 to 6 km depth layer of the velocity model and implies that within this layer there may be a significant change in lithology, in this case probably the contact between the Malmesbury Group and the Namaqua Natal Metamorphic Belt.

There is a change in the P-wave model of 0.4 km/s at 6 km depth (Fig. 7.1) which may represent a change in lithology. The change in velocity can occur anywhere between 2 and 6 km depth range but is only reflected at the 6 km layer because of the layer thickness specified in the input model parameters. The regional unconformity between the Malmesbury Group (MG) and overlying Table Mountain Group (TMG) was topographically higher than all stations except for stations 12, 13, 14 and 15. The maximum difference in elevation between stations is 900 m and thus the contact between the MG and the TMG can only be reflected in the upper 1 km of the velocity model. The top most 1 km of the model is above ground to compensate for topographical elevation differences in station locations. Thus the upper layer (0 to 2 km) in the final P-wave model must contain the Malmesbury Group rocks. Although little is known about the true thickness of the MG, the change in velocity at the 6 km layer from 5.4 to 5.8 km/s may represent the transition from MG to the underlying Namaqua Natal

Metamorphic Belt (NNMB).

Midzi *et al.* (2010) derived an average 1-D P-wave velocity model for all tectonic terranes in South Africa based on inversion of P-waves recorded by the South African National Seismograph Network. This is an improved model based on previous models derived for earthquake location by the Council for Geoscience and predicts an average V_p of 5.6 km/s from the surface down to a depth of 20 km. The P-wave velocity in the Ceres model reaches 5.6 km/s in the 2 to 6 km depth range. A seismic refraction profile across the Cape Fold Belt by Stankiewicz *et al.* (2007) suggested a V_P of 5.4 to 5.8 km/s for the Cape Supergroup rocks. In the Ceres region this velocity range seems to correspond with the MG rocks. A seismic refraction profile by Green and Durrheim (1990) in the Northern Cape across the north western edge of the NNMB found that the lower crust in the region comprises a significant proportion of rocks with V_p ranging from 6.2 to 6.9 km/s. The value of 5.9 km/s derived from the Ceres velocity model thus appear to approach mid crustal values at a depth of 12 km. There can probably be improvement on the Ceres model given a longer observational period.

7.2.1 Station corrections

Station corrections were produced using VELEST after relocating the events. Either positive or negative corrections were produced depending on whether the calculated arrival time of ray paths used for hypocenter location arrived later or earlier, respectively, than the observed travel time at a given station. Figure 7.2 A, B and C show zones of positive and negative corrections overlain by microseismic distribution, geology and topography, respectively. The distribution of positive and negative S-wave corrections broadly mirror the P-wave corrections, although the zone of positive S-corrections is shifted north east relative to the positive P-corrections. This similar distribution of corrections is an indication that the uncertainty in S-picks is not a significant problem as it is expected that random errors will yield a more random distribution of station corrections. The cluster of shallow seismicity (Fig. 7.3) is almost exclusively contained within the zone of positive P-wave corrections with some deeper events of the Tulbagh cluster also in the positive correction zone. The zone of negative S-corrections are host to the deeper seismicity associated with the Tulbagh cluster (Fig. 7.3) and contain some of the shallow events in the Ceres cluster. P-corrections cross cut geological

and topographical more so than S-corrections which approximates the geological and topographical boundaries. In general, the P-picks were more reliable than the S-picks thus the station corrections probably reflect that.

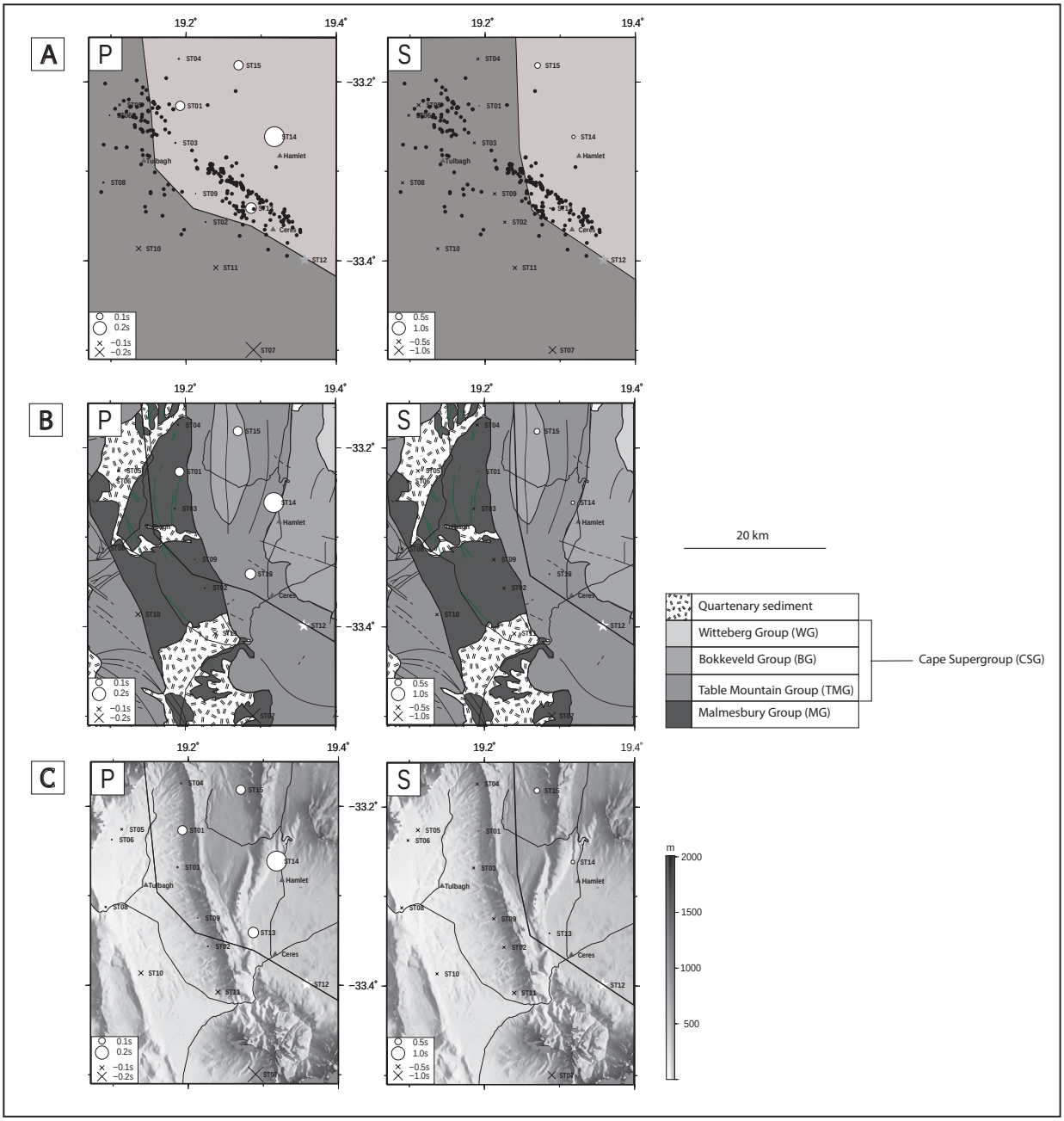

Figure 7.2: A) Zones of similar station correction are highlighted above with positive corrections (light grey) and negative corrections (dark grey) for both P and S waves. Note how the change from positive to negative corrections define a trend in the P-correction distribution that has a similar trend to the microseismic distribution and the S-correction transition has an oblique relation to the microseismic distribution. B) The trend of the change from positive to negative P-corrections cross cuts major geological contacts while the trend of the negative S-corrections corrections approximates the geological contacts. C) The trend defined by the P-wave corrections cross cuts the topography of the region more than the S-wave corrections which is sub-parallel to the large ridges and valleys in the study region.

Dziewonski and Anderson (1983) noted that where coverage of seismic stations are sufficiently dense, P-wave station corrections often reflect the sudden changes between geological provinces. The temporary Ceres array of 2012 was the densest microseismic study to be completed for the region to date, thus the changes in P-wave corrections obtained during this study could reflect a difference in geological properties in the rocks by the systematic negative and positive corrections (Fig. 7.2A) southwest and northeast of the fault zone, respectively.

The change from negative to positive P-wave corrections roughly mimic the distribution of microseismic events. The same change for S-corrections is located more to the east. A large majority of the events of the shallow Ceres cluster are located in the zone of positive P and S corrections. Events of the deeper Tulbagh cluster roughly correlate with the negative P-corrections and is located exclusively in the zone of negative S-corrections.

Most stations installed on the Malmesbury Group (Fig. 7.2B) have negative corrections for P waves. All stations installed on the MG have negative corrections for S waves. The stations installed on Cape Supergroup rocks all have positive corrections for both P and S waves. The CSG rocks are highly fractured as a result of the Cape orogeny, effectively increasing the porosity of the rocks which may result in a lower than expected seismic velocity and thus positive corrections. The greenshcist facies MG overlies the granulite facies metamorphic rocks of the NNMB. Seismic waves probably propagate through the granulitic rocks without losing much velocity and where there are no rocks of the CSG cropping out does not attenuate to the same degree at the surface. If true, this may explain the negative corrections correlating with the outcrop of the MG.

7.3 Hypocenter locations

Sibson (1982) argues that, with a long enough observational period, the maximum depth of aftershocks and the maximum depth of microseismic activity represents the transition from seismic to aseismic, or in other words, frictional to viscous deformation. The transition from frictional deformation to viscous mylonitization may be associated with an increase in temperature with depth (Byerlee and Brace, 1969). The transition from seismic to aseismic deformation in regions with a normal geotherm (roughly 20 °C/km) and hydrostatic fluid

pressure typically occurs at mid-crustal depths of between 10 and 15 km (Sibson, 1977). Meissner and Strehlau (1982) argues that the presence of water and the influence of temperature has more influence on the maximum depth of seismicity than the properties of particular layer of the crust.

The locations of hypocenters of microseismic events recorded in Ceres reflects the geometry and depth at which the underlying faults are microseismically active. There is good agreement between the distribution of microseismic events recorded in 2012 (this study) and the aftershocks of the 1969 M_L 6.3 Ceres earthquake recorded during 1969 and 1970 (Green and Bloch, 1971) (*cf.* Fig. 6.3 and Fig. 3.5).

The strike of the surface trace and orientation of the fault zone, as derived from hypocenters recorded during this study, does not match mapped faults in the region, cross cuts geology and no obvious surface displacement has been observed. These are observations similar to those found by Green and Bloch (1971). Figure 6.3 illustrates that microseismic activity occurs from at least 1 km depth, also a similar observation to Green and Bloch (1971).

The lack of an observed surface expression of the active fault zone does not mean that there is no fault trace at the surface. The rocks that are exposed in the study region are either shale from the Malmesbury Group that has been subject to greenshcist facies metamorphism or Cape Supergroup quartzite and minor shale. The shales are typically not well exposed and forms the gentler, vegetation covered slopes of the mountains in the region. Where MG is exposed the rocks are weathered and in the low lying areas of Tulbagh valley, covered by meters-thick recent alluvium. The quartzite-rich Table Mountain Group is very homogeneous in composition consisting mainly of recrystallised quartz. The quartzite generally forms steeper slopes and cliffs and is to a large degree covered by talus. The easily weathered, alluvium covered shale and the homogeneous quartzite of the region makes identifying and mapping faults difficult. Thus the lack of a fault trace on the surface may simply mean that it has not been found yet, because it is covered by talus and/or alluvium.

In a data review on seismicity in South Africa, Singh *et al.* (2009) identified several clusters of high seismic activity (Fig. 3.1), including a Ceres cluster. Results from this study show that the distribution of microseismicity along the fault zone in the Ceres cluster is bimodal along strike and down dip (Fig. 7.3). Thus, in detail, the Ceres cluster should be viewed as

two separate clusters, namely the Ceres and Tulbagh clusters (Fig. 7.3). The two clusters seen along strike correspond to the two clusters seen at different depths, ie. microseismicity is clustered along strike, and into two clusters with different depth ranges. Microseismic activity in the Ceres cluster ranges from roughly 0 to 5 km depth, with dispersed hypocenters in the 5 to 9 km range. In the Tulbagh cluster, microseisms range from roughly 8 to 12 km deep with scattered events in the 5 to 8 km range. Aftershock depths of the 1969 Ceres earthquake range from 0 to 8 km below Ceres and 4 to 10 km below Tulbagh. The clustering is not as pronounced in the 1969-1970 aftershock locations as they are in the microseismic distribution during this study, but what is similar is that there were no aftershocks shallower than roughly 4 km below below Tulbagh and there are no microseisms shallower than 5 km here.

As the difference in topography between the lowest and highest station location was 900 m, and the presence of TMG topographically higher than all but 4 stations, it is conclusive that the TMG can only cause seismicity in the upper 1 km of the Ceres cluster. Thus there may be some structure/s in the MG that is/are presently microseimically active in the Ceres cluster. Considering the presence of MG rocks at the surface of the Tulbagh cluster, it is not easy to explain the lack of microseismicity in the upper 5 km in this cluster. It may be that the existing structures are not suitably oriented for reactivation in the upper 5 km.

Aftershocks from Green and Bloch (1971) go down to 8 km in the region representing the Ceres cluster. Consequently the lack of microseismic events below 5 km depth in the Ceres cluster does not necessarily imply that the seismic-aseismic transition is this shallow. It may be that there is an active part of the fault zone below 5 km and that the observational period of this study was not long enough to record microseismic activity below this depth. On the assumption that the NNMB is present in the study area below 6 km depth (as discussed previously) then the lack of microseismic activity in the 5 to 12 km depth range below the Ceres cluster could be due to an asperity in the structurally heterogeneous NNMB.

There is, however, an along-strike increase in depth of both the 1969-1970 aftershocks and 2012 microseisms from Ceres to Tulbagh. If the maximum depth of seismicity is taken as 8 km in the Ceres cluster and 15 km in the Tulbagh cluster, it either implies 1) a different thermal structure below the two clusters or 2) there exist a locked part of the fault zone. On the assumption that NNMB rocks of the upper crust in the region are of a general quartzo-felspathic composition that starts to deform plastically at 350 °C, it translates to

geotherms of roughly 39 and 23 °C/km for the two clusters, respectively, if this change is thermally controlled. No previous work has estimated a geothermal gradient for the Ceres region and there is little to compare these values to in order to know whether it is a reliable estimate. A factor of 1.7 difference in geotherm across less that 40 km in a continental setting with no known magmatic activity is unlikely. Thus option 1 above is improbable. The NNMB is a compositionally and structurally heterogeneous shield. It is conceivable that the heterogeneities can cause faults to encounter more resistant rock or unsuitably oriented structures and lock up sections of active fault zone. Thus it is proposed that the depth of the seismogenic zone in the region of the study area is located at roughly 15 km and that the fault zone below the Ceres cluster is locked and may fail seismically at some point in time, as it did in 1969 and 1970.

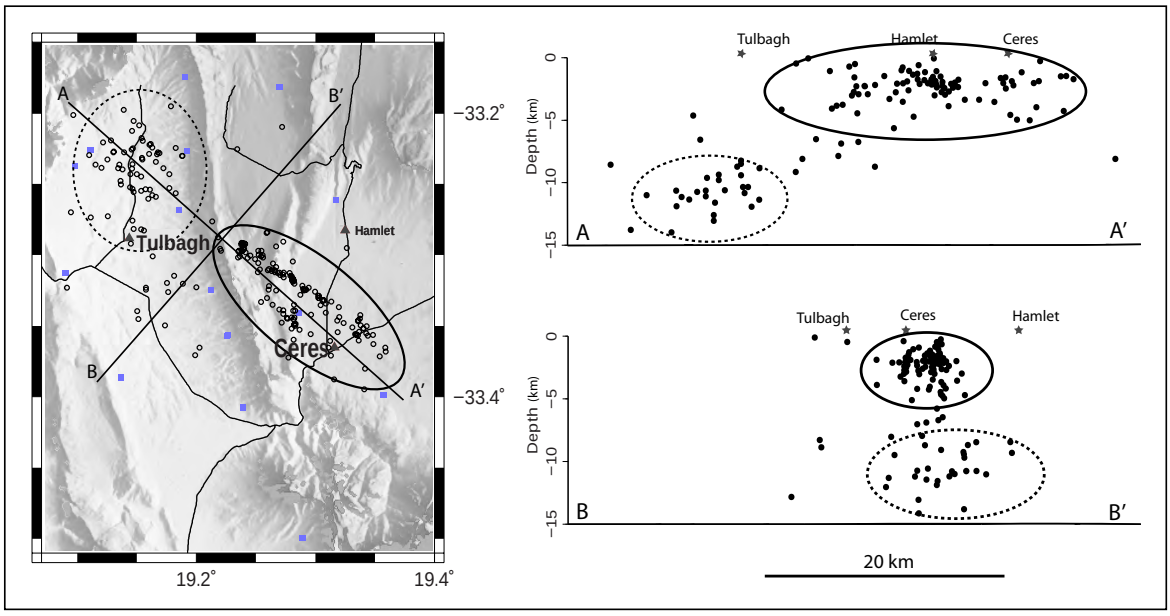

Figure 7.3: The distribution of microseismic events defines two clusters in the study region, namely the Ceres cluster (solid line) in the south east and the Tulbagh cluster (dashed line) in the north west. Depth projections along A-A' and B-B' reveal that the clusters also have different depth distributions.

7.4 Magnitude

The method described in chapter 5 to calculate magnitudes is an empirical calibration where microseismic events within a radius of 0-30 km were calibrated to an event of known magnitude more than 100 km away. There is an inherent uncertainty in the values cited as the magnitude calculations are very strongly dependent on the epicentral distance of events.

Microseismic events for this study ranged from -2.2 $< M_L <$ 1.6 with magnitude of completeness of M_L -1.5. Jost *et al.* (1998) recorded induced microseismic events in a bore-hole at 9 km depth during the KTB drilling project ranging from -2 $< M_L <$ 0 with a magnitude of completeness of M_L -1.6. Abercrombie (1995) recorded natural seismicity in the Cajun Pass Scientific Project bore-hole at 2 km depth ranging from -1 $< M_L <$ 5.5 with $M_c \approx 0$. What both these studies have in common is that geophones were installed in boreholes thus eliminating surface interference effects.

Braeuer *et al.* (2012) recorded seismicity in the Dead Sea region with a surface array and calculated a duration magnitude (M_D) range of -0.5 $< M_D <$ 4.5 with M_c 0.4. Albaric *et al.* (2010) recorded seismicity in North Tanzanian Divergent Zone of the EARS with a range of 3.5 $< M_w <$ 5.9 and M_c 3.5. The magnitude scales used during both these experiments are different to M_L used during the current study but it is worth noting the higher range of magnitudes obtained from these studies that both had surface installations.

The reason for the low magnitude range detected by the Ceres array may be attributed to: 1) the shallow levels at which consolidated rock occurs in the Ceres and Tulbagh region resulting in low attenuation of seismic waves near the surface; 2) shallow level of seismicity and thus decreasing the source to receiver distance and increasing the probability of recording seismic events 3) short recording period.

The magnitude range and magnitude of completeness of the Ceres data seems comparable to values obtained from studies with bore-hole installations. It appears that the Ceres array had a good detection limit considering the geophones were installed on the surface.

If the estimation from Singh *et al.* (2009) that the Ceres cluster experiences roughly 6 M_L 1 events per month was true, there should have been roughly 18 M_L 1 events present in the data

and represented in figure 6.7. Conversely there is only one event in this magnitude range, an M_L 1.6 event. As M_L is a relative scale, it may be possible that the calibration of the M_L scale for this study underestimates the absolute magnitude of the events. From figure 6.7 the magnitude that best fit the estimation is M_L -1 for which 20 events were recorded. Thus, if the prediction made by Singh *et al.* (2009) is true, our magnitude range underestimates the absolute value by two orders of magnitude. Conversely, the prediction by Singh *et al.* (2009) was done on data from the SANSN and the detection limit of the network of is roughly M_L 3 (Saunders, 2005). Thus Singh *et al.* (2009) could have overestimated the magnitude range for which they made the predictions.

7.5 Focal mechanisms

One of the aims of this study was to produce focal mechanisms for some of the larger events that were located near the center of the array. A short list of events recorded on 12 or more stations, that could potentially be used for focal mechanism inversion, was compiled. The majority of events that were located near the center of the array were only recorded by up to 6 stations and thus did not suitably define all quadrants of the focal sphere that is needed to establish the P and T axes orientations. Many of the high amplitude events that were noted during phase picking plotted outside the array after relocation. After relocation a total of 4 events met the criteria of being located near the center of the array and being recorded on 12 or more stations. Studying the waveforms of these 4 events it was noted that the signals at at least three stations were accompanied by high noise levels thus reducing the reliable picks to less than 10 per event. High noise, as discussed earlier, means filtering had to be applied and in the process data could potentially be lost. If the polarity of the P-waves could only be picked if filtering was applied to see the polarity, then the station was not considered for focal mechanism inversion. The combination of noise, location of events relative to the array and attenuation of low amplitude seismic waves being recorded on few stations meant the data were not suitable for focal mechanism inversion.

7.6 Ceres seismic activity

A sinistral strike slip mechanism striking at 319±2° was obtained for the 1969 M_L 6.3 earthquake from 42 stations of the global seismic monitoring network (Green and McGarr, 1972). According to Andersonian theory (**?**), strike-slip faulting occurs on vertical planes at 30° to σ_1 with a vertical σ_2 (Fig. 7.4). The trend of the best fit line through the 1969-1970 aftershock zone is 299° (Green and Bloch, 1971). The trend of the plane of average microseismic activity from 2012 is roughly 305° and within uncertainty closely matches the trend of the 1969-1970 aftershock plane.

The similarity in the orientation of the 1969-1970 aftershock zone (Green and Bloch, 1971) and microseismic zone from the current study suggests that the same fault zone that produced the 1969 and 1970 aftershocks is now microseismically active. The similarity in geometry of the fault zone, *i.e.* the sub-vertical orientation of the fault zone suggests that a strike-slip mechanism is still responsible for seismic activity in the region. The Strike-slip faulting regime observed in the south-western coastal region of South Africa is different to the NE interior of the country where a normal faulting regime is observed (Singh *et al.*, 2009).

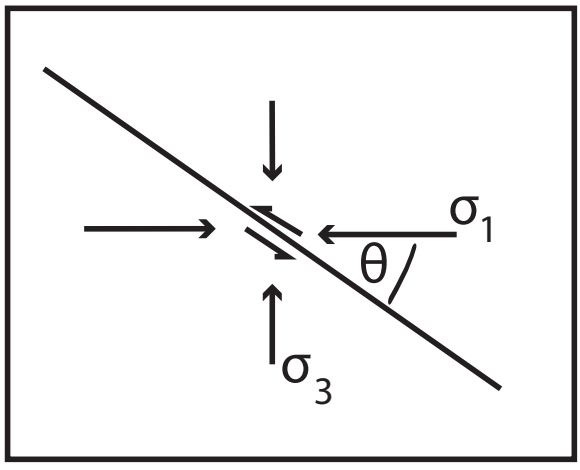

Figure 7.4: Illustration of Andersonian faulting conditions with respect to the orientation of the principle stresses. Note that for a strike-slip fault σ_2 would be vertical and the fault would occur on a vertical plane.

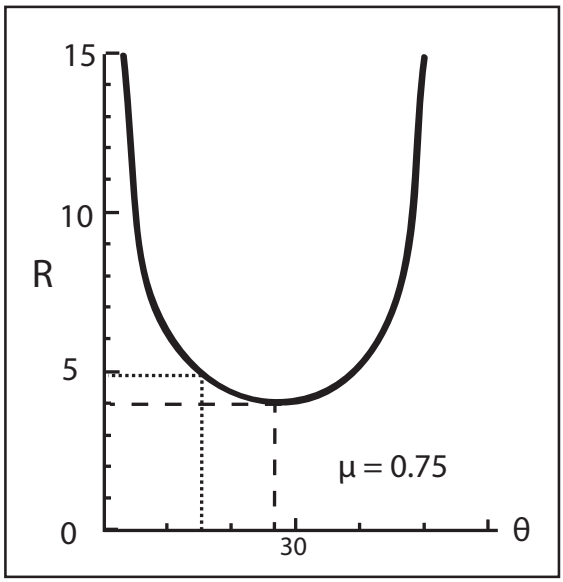

Figure 7.5: The reactivation ratio (R) is at its lowest (4) when $\theta \approx 30°$ (dashed line). For $\theta \approx 15°$, $R \approx 5$ (dotted line). Figure adapted from (Sibson, 1985).

There is a broad zone of maximum compressive stress along the western coastal margin of South Africa known as the Wegener Stress Anomaly (WSA) (Andreoli *et al.*, 1996). The trend of the WSA is not well defined but strikes roughly NW-SE. According to Sibson (1985), the stress ratio for reactivation (Eqn. 2.5) of continental faults, which is more likely than creating new structures (Sykes, 1978), is ideal when the angle between the greatest principle stress and the fault plane (θ) is roughly 30° (Fig. 7.5). Based on the trend of microseismic activity from this study (305°), it follows that the WSA must be at some angle close to 30° relative to the active microseismic plane to cause reactivation of deeper, inherited structures in the basement rocks. Viola *et al.* (2012) suggest, based on analysis of fractures systems that southwest Africa experiences WNW trending horizontal stresses.

Figure 4.5 illustrates that there are fault surface traces of Malmesbury or Namaqua-Natal age in the region surrounding Ceres and Tulbagh that are oriented roughly NW-SE. This may imply that these sets of structures are suitably, although not ideally, oriented for reactivation. The orientation (319°) of the 1969 nodal plane may also be suitably, but not perfectly, oriented for reactivation along an existing structure in the current stress field. The sinistral offset derived from focal mechanism inversion of the 1969 M_L 6.3 Ceres earthquake (Fig. 7.6)

implies that for reacticvation there needs to exist a horzontal maximum compressive stress (Anderson, 1951) oriented roughly 30° relative to the existing structures (Sibson, 1985).

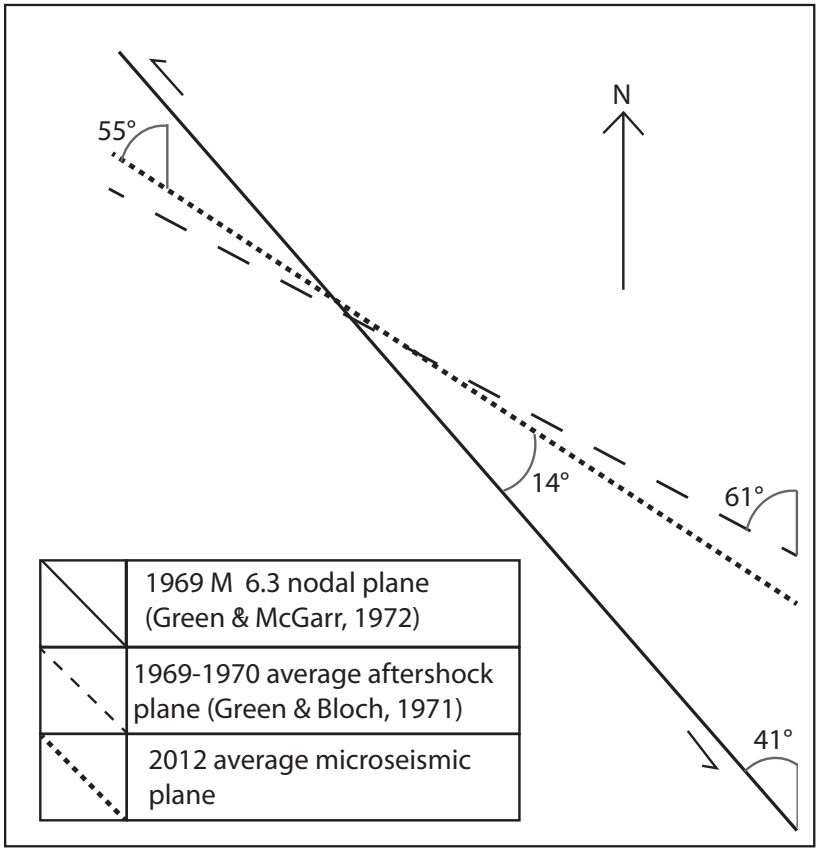

Figure 7.6: The orientation of the 1969 M_L 6.3 Ceres earthquake is well oriented for reactivation if it is assumed that the trend of the 1969-1970 aftershock zone and the trend of the 2012 microseismic zone represents the direction of maximum compressive stress.

7.6.1 Driving forces

In South Africa, as a stable continental region (Saunders *et al.*, 2013; Johnston, 1996) the driving forces are not as obvious as, for example, in the East African Rift System (EARS). In a worldwide analysis of shallow seismicitiy in continental regions, Klose and Seeber (2007) point out that even though stable continental regions are relatively isolated from the direct influence of plate boundary stresses, stresses can be transmitted to stable continental regions.

Based on previous focal mechanisms (Green and McGarr, 1972; Brandt and Saunders, 2011),

stress measurements from bore-hole breakouts (Viola *et al.*, 2005), thin shell rheological modeling (Bird *et al.*, 2006), fracture analysis (Viola *et al.*, 2012), geodetic measurements (Malservisi *et al.*, 2013), together with the location and orientation of microseismic activity(this study) it is apparent that the southwestern coastal margin of South Africa experiences a strike-slip regime with a general NW-SE trend in horizontal stress. This is in contrast with the normal faulting regime that is observed in central and NE South Africa with a general E-W trend in horizontal stress Bird *et al.* (2006); Delvaux and Barth (2010) which may be related to the southward propagation of the EARS and gravitational potential energy. Conversely, the strike slip regime observed on the south west coast does not correlate clearly with any tectonic processes and does not match with the models of extension caused by either rift propagation (Bird *et al.*, 2006) or topographical potential relaxation (Delvaux and Barth, 2010) and thus another explanation is required. Bird *et al.* (2006) argue that stress in the interior of the plate along the south western coast could be generated by the relative rotation of the Somali and Nubian plates (Fig. 3.2) with the cold and rigid lithosphere underlying southern Africa posing resistance to deformation. Brandt and Saunders (2011) argue that the oceanic spreading ridges surrounding the southern part of the continent are responsible for the observed strike-slip regime. Viola *et al.* (2005) also attributes the seismic activity to far field stress transfer originating from the oceanic spreading ridges.

When the forces acting on the African plate in southern Africa are simplified (Fig. 7.7), and considering that a strike-slip fault forms as a result of a horizontal maximum compressive stress (Anderson, 1951), the direction of spreading of the Southwest Indian Ridge fits the formation of the strike-slip regime observed along the southwestern coast of South Africa. The north-westerly movement of the African plate in the Cape Town region (Malservisi *et al.*, 2013) is similar to the orientation of the observed strike-slip zone and the direction of spreading of the Southwest Indian ridge. The stress could be transmitted along transform faults along the ocean floor and cause the reactivation of the Ceres fault zone. If this is indeed the case, then it is conceivable that the transform fault may one day bridge onto land and link up with the Ceres fault. In this way it may be possible to form a new plate boundary inland of the present day coastline of South Africa. Although speculative, it can be proposed that the strike slip zone represents an area that is undergoing incipient plate boundary formation and that strike slip faulting observed in this zone may be the first manifestations a major transform fault. To test this theory one will need to deploy dense seismic arrays across

the south western margin of South Africa to establish where the boundary between normal and strike slip faulting lies and whether or not the observed zone of strike-slip is indeed representative of a regional strike-slip regime.

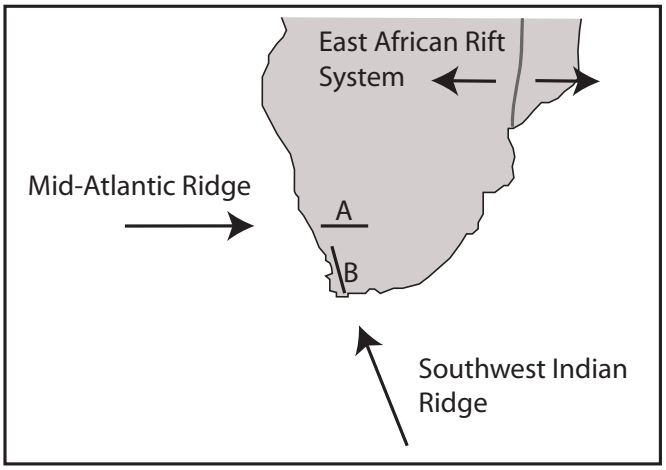

Figure 7.7: Simplification of the forces acting on the African plate in southern Africa by assuming the greatest compressive stress perpendicular to spreading ridges. Normal faulting in central and north eastern South Africa may be explained by the spreading forces generated by the EARS. If the Mid Atlantic Ridge was the dominant force on the south western coastal margin then one would expect to see structures developing with an orientation sub-parallel to the spreading direction of the ridge (A). However the structure forming in Ceres is sub-parallel to the spreading direction of the Southwest Indian Ridge (B) leading to the suggestion that far field stress transfer from the Soutwest Indian Ridge is responsible for the strike slip regime observed along the southwestern coastal margin of South Africa.

Chapter 8

Conclusions

In the course of the observational period of 3 months during 2012 a total of 168 microseismic events were located within the boundaries of the array of roughly 30 km x 40 km. The surface trace of the average plane of microseismic activity does not match previously mapped faults in the region. V_p ranges from 4.9 km/s at the surface to 6.4 km/s at a depth of 12 km. V_s ranges from 2.8 km/s to 4.7 km/s from the surface down to 12 km, respectively. The change over from positive to negative station corrections reflect the strike of the microseismic plane.

The magnitude range for the events was -2.2 $< M_L <$ 1.6 with a magnitude of completeness of M_c -1.5. Although this study used seismometers installed on the surface, the magnitude range is comparable with other studies that installed geophones in bore-holes kilometers deep, probably due to the low attenuation of bedrock at surface levels in the study region. The maximum depth of seismicity, and thus the brittle-ductile transition, in the Ceres region is taken to be at 15 km depth.

Microseismicity occurred on a sub-vertical fault zone roughly 4 km wide. The strike of the surface trace of the average plane of microseismic events is 305°. The strike of the surface trace of the average aftershock plane of the 1969-1970 Ceres earthquakes is 299°. Aftershocks also occurred on a sub-vertical fault zone roughly 4 km wide. Within error, the orientation and geometry of the microseismic plane is similar to that of the aftershock plane. It is thus assumed the same structure that caused the 1969-1970 Ceres earthquakes is still active and that is has a sinistral strike-slip orientation.

The maximum horizontal compressive stress is estimated to be roughly NW-SE to WNW-ESE. Given the orientation of the active fault zone in Ceres, it is proposed that basement structures in the Malmesbury Group and the Namaqua Natal Metamorphic Complex is suitably, but not perfectly, oriented for reactivation in the current stress field.

It is proposed that the spreading of the mid ocean ridges, in particular the Southwest Indian ridge, surrounding the southern African plate could be the driving force behind the microseismicity. It is further proposed, albeit based on speculation, that the strike slip faulting observed in the Ceres region could be the start of incipient plate boundary formation in the form of a newly developing transform fault along the present Ceres fault.

References

Abercrombie, R. (1995). Earthquake locations using single-station deep borehole recordings: Implications for microseismic activity on the San Andreas fault in southern California. *Journal of Geophysical Research*, *100*, 24003–24014.

Aki, K. (1967). Scaling law of seismic spectrum. *Journal of Geophysical Research*, *72*, 1217–1231.

Albaric, J., Perrot, J., Déverchère, J., Deschamps, A., Le Gall, B., Ferdinand, R. W., Petit, C., Tiberi, C., and Songo, M. (2010). Contrasted seismogenic and rheological behaviors from shallow and deep earthquake sequences in the North Tanzania Divergence, East Africa. *Journal of African Earth Sciences*, *58*, 799–811.

Anderson, E. (1951). *The dynamics of faulting*. Oliver & Boyd.

Andreoli, M. A. G., Doucore, M., Van Bever Donker, J., Brandt, D., and Andersen, N. J. B. (1996). Neotectonics of southern Africa - a review. *Africa Geoscience Review*, *3*, 1–16.

Begg, G. C., Griffin, W. L., Natapov, L. M., O'Reilly, S. Y., P., G. S., O'Neill, C., Hronsky, J. M. A., Djomani, Y. P., Swain, C. J., Deen, T., and Bowden, P. (2009). The lithospheric architecture of Africa: Seismic tomography, mantle petrology, and tectonic evolution. *Geosphere*, *5*, 23–50.

Belcher, R. W. and Kisters, A. F. M. (2003). Lithostratigraphic correlations in the western branch of the Pan-African Saldania belt, South Africa: the Malmesbury Group revisited. *South African Journal of Geology*, *106*, 327–342.

Ben-Avraham, Z., Hartnady, C. J. H., and Kitchin, K. A. (1997). Structure and tectonics of the Agulhas-Falkland fracture zone. *Tectonophysics*, *282*, 83–89.

Bird, P., Ben-Avraham, Z., Schubert, G., Andreoli, M., and Viola, G. (2006). Patterns of stress and strain rate in South Africa. *Journal of Geophysical Research*, *111*, 1–14.

Booth, P. (2011). Stratigraphic, structural and tectonic enigmas associated with the Cape Fold Belt: challenges for future research. *South African Journal of Geology*, *114*, 235–238.

Booth, P. W. K., Brundson, G., and Shone, R. W. (2004). A duplex model for the Eastern Cape Fold Belt? Evidence from the Palaeozoic Witteberg and Bokkeveld Groups (Cape Supergroup), near Steytlerville, South Africa. *Gondwana Research*, *7*, 211–222.

Booth, P. W. K. and Shone, R. W. (2002). A review of thrust faulting in the Eastern Cape Fold Belt, South Africa, and the implications for current lithostratigraphic interpretation of the Cape Supergroup. *Journal of African Earth Sciences*, *34*, 179–190.

Brace, W. F. and Byerlee, J. D. (1966). Stick-slip as a mechanism for earthquakes. *Science*, *153*, 990–992.

Braeuer, B., Asch, G., Hofsetter, R., Haberland, C., Jaser, D., El-Kelani, R., and Weber, M. (2012). Micoseismicity distribuiton in the southern Dead Sea basin and its implications on the structure of the basin. *Geophysical Journal International*, *188*, 873–878.

Brandt, D., Andreoli, M. A. G., and McCarthy, T. S. (2005). The late Mesozoic palaeosoils and Cenozoic fluvial deposits at Vaalputs, Namaqualand, South Africa: possible depositional mechanisms and their bearing on the evolution of the continental margin. *South African Journal of Geology*, *108*, 271–284.

Brandt, M. B. and Saunders, I. (2011). New regional moment tensors in South Africa. *Seismological Research Letters*, *82*, 69–80.

Byerlee, J. D. (1978). Friction of rocks. *Pure Applied Geophysics*, *116*, 615–626.

Byerlee, J. D. and Brace, W. F. (1969). Stick-slip, stable sliding and earthquakes - effect of rock type, pressure, strain rate and stiffness. *Journal of Geophysical Research*, *73*, 4741–4750.

Campbell, D. A. (1978). Investigation of the stress-concentration mechanism for intraplate earthquakes. *Geophysical Research Letters*, *5*, 477–479.

Choy, G., McGarr, A., Kirby, H., and Boatwright, J. (2009). An overview of the global variability in energy release and apparent stress. In *Earthquakes: Radiated energy and the physics of faulting*. American Geophysical Union.

Clifford, T., Barton, E. S., Retief, E. A., Rex, D. C., and Fanning, C. M. (1995). A crustal progenitor for the intrusive anorthosite-charnokite kindred of the cupriferous Koperberg Suite, Okiep District, Namaqualand, South Africa: new isotope data for the country rocks and the intrusives. *Journal of Petrology*, *36*, 231–258.

Cloetingh, S., Lankreijer, A., de Wit, M. J., and Martinez, I. (1992). *Inversion Tectonics of the Cape Fold Belt, Karoo and Cretaceous Basins of Southern Africa*, Chapter Subsidence history analysis and forward modeling of the Cape and Karoo Supergroups, 239–248. Balkema.

Da Silva, L. C., Gresse, P. G., Scheepers, R., McNaughton, N. J., Hartman, L. A., and Fletcher, I. (2000). U-Pb SHRIMP and Sm-Nd age constraints on the timing and sources of the Pan-African Cape Granite Suite, South Africa. *Journal of African Earth Sciences*, *30*, 795–815.

de Wit, M. J., Cornell, E. J., de Ronde, E. J., Tredoux, M., Roering, C., Hart, R. J., Armstrong, R. A., Green, R. W. E., Pederby, E., and Hart, R. A. (1992). Formation of an Archaean continent. *Nature*, *357*, 553–562.

Delvaux, D. and Barth, A. (2010). African stress pattern from formal inversion of focal mechanism data. *Tectonophysics*, *482*, 105–128.

Dziewonski, A. M. and Anderson, D. L. (1983). Travel times and station corrections for P waves at teleseismic distances. *Journal of Geophysical Research*, *88*, 3295–3314.

Fernandez, L. M. (1974). Geophysical implications of the Ceres earthquake succession of 1969 - 1971. *Seismology Series*, *4*, 34–43.

Frimmel, H. E., Basei, M. A. S., Correa, V., and Mbangula, N. (2013). A new lithostratigraphic subdivision and geodynamic model for the Pan-African western Saldania Belt, South Africa. *Precambrian Research*, *Accepted manuscript*.

Frimmel, H. E., Fölling, P. G., and Diamond, R. (2001). Metamorphism of the Permo-Triassic Cape Fold Belt and its basement, South Africa. *Mineralogy and Petrology*, *73*, 325–346.

Gordon-Welsh, J. F. (1974). Some hydrological occurrences in the Southwestern Cape which is associated with the Ceres earthquake. *Seismology Series*, *4*, 22–26.

Green, R. and Bloch, S. (1971). The Ceres, South Africa, earthquake of September 29, 1969. Report on some aftershocks. *Bulletin of the Seismological Society of America*, *61*, 851–859.

Green, R. W. E. and Durrheim, R. J. (1990). A seismic refraction investigation of the Namaqualand metamorphic complex, South Africa. *Journal of Geophysical Research*, *95*, 19927–19932.

Green, R. W. E. and McGarr, A. (1972). A comparison of the focal mechanism and aftershock distribution of the Ceres, South Africa earthquake of September 29, 1969. *Bulletin of the Seismological Society of America*, *62*, 869–871.

Gresse, P. G. (1997). 1:250 000 Geological Series, 3319 Worcester. *Council for Geoscience*.

Gresse, P. G., von Veh, M. W., and Frimmel, H. E. (2009). *The Geology of South Africa*, Chapter Namibian (Neoproterozoic) to Early Cambrian successions, 395–420. Geological Society of South Africa and the Council of Geoscience.

Gutenberg, B. and Richter, C. F. (1944). Frequency of earthquakes in California. *Bulletin of the Seismological Society of America*, 185–188.

Hälbich, I. W. (1983a). A geodynamic model of the Cape Fold Belt. *Special Publication, Geological Society of South Africa*, *12*, 177–184.

Hälbich, I. W. (1983b). A tectonogenesis of the Cape Fold Belt (CFB). *Special Publication, Geological Society of South Africa*, *12*, 165–175.

Hand, M. and Sandiford, M. (1999). Intraplate deformation in central Australia, the link between subsidence and fault reactivation. *Tectonophysics*, *305*, 121–140.

Hanks, T. C. and Kanamori, H. (1979). A moment magnitude scale. *Journal of Geophysical Research*, *84*, 2348–2350.

Hartnady, C. J. H., Newton, A. R., and Theron, J. N. (1974). The stratigraphy and structure of the Malmesbury Group in the southwestern Cape. *Bulletin of the Precambrian Research Unit*, *15*, 193–213.

Havskov, J. and Ottemöller, L. (2010). *Routine data processing in Earthquake seismology.* Springer.

Hubbert, M. K. and Rubey, W. (1959). Role of fluid pressure in the mechanics of overthrust-faulting. *Bulletin of the Seismological Society of America*, *70*, 115–205.

Husen, S., Kissling, E., and Clinton, J. F. (2011). Local and regional minimum 1D models for earthquake location and data quality assessment in complex tectonic regions: application to Switzerland. *Swiss Journal of Geoscience*, *104*, 455–469.

Jackson, D. D. and Anderson, D. L. (1970). Physical mechanisms of seismic-wave attenuation. *Reviews of Geophysics*, *8*, 1–63.

Johnson, M. R. (1991). Sandstone petrography, provenance and plate tectonic setting in Gondwana context of the southeastern Cape-Karoo Basin. *South African Journal of Geology*, *94*, 137–154.

Johnson, M. R., Anhaeusser, C. R., and Thomas, R. J. (Eds.) (2009). *The Geology of South Africa.* Council for Geoscience.

Johnson, M. R., Visser, J. N. J., Cole, D. I., de V. Wickens, H., Christie, A. D. M., Roberts, D. L., and Brandl, G. (2006). *Geology of South Africa*, Chapter Sedimentary rocks of the Karoo Supergroup, 461–499. Geological Society of South Africa and the Council of Geoscience.

Johnston, A. C. (1996). Seismic moment assessment of earthquakes in stable continental regions-I. Instrumental seismicity. *Geophysical Journal International*, *124*, 381–414.

Johnston, S. T. (2000). The Cape Fold Belt and syntaxis and the rotated Falkland Islands: dextral transpressional tectonics along the southwest margin of Gondwana. *Journal of African Earth Sciences*, *31*, 51–63.

Jost, M. L., Büßelberg, T., Jost, O., and Harjes, H.-P. (1998). Source parameters of injection-induced microearthquakes at 9 km depth at the KTB deep drilling site, Germany. *Bulletin of the Seismological Society of America*, *88*, 815–832.

Kanamori, H. (1973). Mode of strain release in major earthquakes in Japan. Technical report, Earthquake Research Institute, Tokyo University, Japan.

Kanamori, H. (1977). The energy release in great earthquakes. *Journal of Geophysical Research*, *82*, 2981–2987.

Kanamori, H. and Anderson, D. (1975). Theoretical basis of some empirical relations in seismology. *Bulletin of the Seismological Society of America*, 1073–1095.

Kanamori, H. and Rivera, L. (2006). Energy partitioning during an earthquake. *Geophysical Monograph series*, *170*, 3–13.

Keyser, A. (1974). Various macroseismic observations in the Meizoseismal area of the Ceres earthquake. *Seismology Series*, *4*, 16–22.

Kijko, A., Retief, S. J. P., and Graham, G. (2002). Seismic Hazard and Risk Assessment for Tulbagh, South Africa: Part I Assessment of Seismic Hazard. *Natural Hazards*, *26*, 175–201.

Kissling, E. (1995). Program VELEST user's guide - Short introduction. *Institute of Geophysics, ETH Zuerich*, 1–26.

Klose, C. D. and Seeber, L. (2007). Shallow seismicity in stable continental regions. *Seismological Research Letters*, *78*, 554–562.

Lee, W. H. K., Kanamori, H., Jennings, P., and Kisslinger, C. (2003). *International handbook of earthquake and engineering seismology.* Academic Press.

Li, Q., Liu, L. M., and Stein, S. (2009). Spatiotemporal complexity of continental intraplate seismicity: Insights from geodynamic modeling and implications for seismic hazard estimation. *Bulletin of the Seismological Society of America*, *99*, 52–60.

Lindeque, A. S., Ryberg, T., Stankiewicz, J., Weber, M., and de Wit, M. J. (2007). Seismic imaging of the crust and Moho in a section across the Beatie Magnetic Anomaly, South Africa. *South African Journal of Geology*, *110*, 419–438.

Lock, B. E. (1980). Flat-plate subduction and the Cape Fold Belt of South Africa. *Geology*, *8*, 35–39.

Malservisi, R., Hugentobler, U., Wonnacott, R., and Hackl, M. (2013). How rigid is a rigid plate? Geodetic constraints from the TrigNet CGPS network, South Africa. *Geophysical Journal International*, *192*, 918–928.

Meissner, R. and Strehlau, J. (1982). Limits of stresses in continental crust and their relation to the depth-frequency distribution of shallow earthquakes. *Tectonophysics*, *1*, 73–89.

Midzi, V., Saunders, I., Brandt, M. B. C., and Molea, T. (2010). 1-D velocity model for use by the SANSN in earthquake location. *Seismological Research Letters*, *81*, 460–466.

Mielke, C. and de Wit, M. J. (2009). Large-scale structural map of the Cape Fold Belt derived by remote sensing analysis. *SAGA Biennial Technical Meeting and Exhibition Swaziland*, *11*, 521–523.

Mignan, A. (2012). Functional shape of the earthquake frequency-magnitude distribution and completeness magnitude. *Journal of Geophysical Research*, *117*, B08302.

Mussett, A. and Kahn, M. (2000). *Looking into the Earth.* Cambridge University Press.

Newton, A. R., Shone, R. W., and Booth, P. W. K. (2006). *The Cape Fold Belt.* Geological Society of South Africa and the Council of Geoscience.

Paton, D. A., Macdonald, D. I. M., and Underhill, J. R. (2006). Applicability of thin skinned structural models in a region of multiple inversion episodes; southern South Africa. *Journal of Structural Geology*, *28*, 1933–1947.

Pavoni, N. (1992). Rifting of Africa and pattern of mantle convection beneath the African plate. *Tectonophysics*, *215*, 35–53.

Raith, J. G., Cornell, D. H., Frimmel, H. E., and De Beer, C. H. (2003). New insights into the geology of the Namaqua Tectonic Province, South Africa, from ion probe dating of detrital and metamorphic zircon. *The Journal of Geology*, *111*, 347–366.

Reid, H. F. (1911). *The elastic rebound theory of earthquakes.* University of California Press.

Richardson, R. M., Solomon, S. C., and Sleep, N. H. (1979). Tectonic stress in the plates. *Reviews of Geophysics and Space Physics*, *17*, 981–1019.

Romanowicz, B. (2008). Using seismic waves to image Earth's internal structure. *Nature*, *451*, 266–268.

Rozendaal, A., Gresse, P. G., and P., L. R. J. (1999). Neoproterozoic to Early Cambrian crustal evolution of the Pan-African Saldania Belt, South Africa. *Precambrian Research*, *97*, 303–323.

Rozendaal, A. and Scheepers, R. (1995). Magmatic and related mineral deposits of the Pan-African Saldania Belt in the Western Cape Province, South Africa. *Journal of African Earth Sciences*, *21*, 107–126.

Saunders, I. (2005). Seismicity of South Africa: South Afican National Seismograph Network (SANSN) FDSN report. 1–8.

Saunders, I., Brandt, M. B., Steyn, J., Roblin, D., and Kijko, A. (2008). The South African National Seismograph Network. *Seismological Research Letters*, *79*, 203–210.

Saunders, I., Ottemöller, L., Brandt, M. B., and Fourie, Christoffel, J. (2013). Calibration of an M_L scale for South Africa using tectonic earthquake data recorded by the South African National Seismograph Network: 2006 to 2009. *Journal of Seismology*, *02*, 437–451.

Scheepers, R. and Schoch, A. E. (2009). *The Geology of South Africa*, Chapter The Cape Granite Suite, 421–432. Geological Society of South Africa and the Council of Geoscience.

Schulte, S. M. and Mooney, W. D. (2005). An updated global earthquake catalogue for stable continental regions: reassessing the correlation with ancient rifts. *Geophysical Journal International*, *161*, 707–721.

Shearer, P. (2009). *Introduction to seismology*. Cambridge University Press.

Shone, R. W. and Booth, P. W. K. (2005). The Cape Basin, South Africa: a review. *Journal of African Earth Sciences*, *43*, 196–210.

Sibson, R. H. (1977). Fault rocks and fault mechanisms. *Journal of the Geological Society*, *133*, 191–213.

Sibson, R. H. (1982). Fault zone models, heat flow, and the depth distribution of earthquakes in the continental crust of the United States. *Bulletin of the Seismological Society of America*, *72*, 151–163.

Sibson, R. H. (1983). Continental fault structure and the shallow earthquake source. *Journal of the Geological Society*, *140*, 741–767.

Sibson, R. H. (1985). A note on fault reactivation. *Journal of Structural Geology*, *7*, 751–754.

Singh, M., Kijko, A., and Durrheim, R. (2009). Seismotectonic models for South Africa: Synthesis of geoscientific information, problems, and the way forward. *Seismological Research Letters*, *80*, 71–80.

Stankiewicz, J., Ryberg, T., Schulze, A., Lindeque, A., Weber, M. H., and de Wit, M. J. (2007). Initial results from wide-angle seismic refraction lines in the southern Cape. *South African Journal of Geology*, *110*, 407–418.

Sykes, L. R. (1978). Intraplate seismicity, reactivation of preexisting zones of weakness, alkaline magmatism, and other tectonism postdating continental fragmentation. *Reviews of Geophysics and Space Physics*, *16*, 621–688.

Tankard, A. J. and Barwis, J. H. (1982). Wave-dominated deltaic sedimentation in the Devonian Bokkeveld Basin of South Africa. *Journal of Sedimentary Petrology*, *52*, 959–974.

Tarantola, A. (2006). Popper, Bayes and the inverse problem. *Nature Physics*, *2*, 492–494.

Tham, A. G. and Johnson, M. R. (2009). *The Geology of South Africa*, Chapter The Cape Supergroup, 443–460. Geological Society of South Africa and the Council of Geoscience.

Thatcher, W. and Hanks, T. C. (1973). Source parameters of Southern California earthquakes. *Journal of Geophysical Research*, *78*, 8547–8576.

Theron, J. (1974). The seismic history of the Southwestern Cape Province. *Seismology Series*, *4*, 9–16.

Toksöz, M. N., Johnston, D. H., and Timur (1979). Attenuation of seismic waves in dry and saturated rocks: I. Laboratory measurements. *Geophysics*, *44*, 681–690.

Trifunac, M. D. and Brady, A. G. (1975). On the correlation of seismic intensity scales with the peaks of recorded strong ground motion. *Bulletin of the Seismological Society of America*, *65*, 139–162.

USGS (2013). Modified Mercalli Intensity scale.

Viola, G., Andreoli, M., Ben-Avraham, Z., Stengel, I., and Reshef, M. (2005). Offshore mud volcanoes and onland faulting in southwestern Africa: neotectonic implications and constraints on the regional stress field. *Earth and Plannetary Science Letters*, *231*, 147–160.

Viola, G., Kounov, A., Andreoli, M. A. G., and Mattila, J. (2012). Brittle tectonic evolution along the western margin of South Africa: More than 500 Myr of continued reactivation. *Tectonophysics*, *514-517*, 93–114.

Walsh, J. B. (1966). Seismic wave attenuation in rock due to friction. *Journal of Geophysical Research*, *71*, 2591–2599.

Warpinski, N. (2009). Microseismic monitoring: Inside and out. *Journal of Petroleum Technology*, 80–85.

Wesnousky, S. G. (1999). Crustal deformation processes and the stability of the Gutenberg-Richter relationship. *Bulletin of the Seismological Society of America*, *89*, 1131–1137.

Wiemer, S. and Wyss, M. (2000). Minimum magnitude of completeness in earthquake catalogs: Examples from Alaska, the Western United States and Japan. *Bulletin of the Seismological Society of America*, *90*, 859–869.

Wood, H. O. and Neumann, F. (1931). Modified Mercalli intensity scale of 1931. *Bulletin of the Seismological Society of America*, *21*, 277–283.

Zegers, T. E., de Wit, M. J., Dann, J., and White, S. H. (1998). Vaalbara, Earth's oldest assembled continent? A combined structural, geochronological, and palaeomagnetic test. *Terra Nova*, *10*, 250–259.

Zoback, M. L. (1992). First and second-order patterns of stress in the lithosphere: the world stress map project. *Journal of Geophysical Research*, *97*, 11703–11728.

Chapter 9

Appendix 1

Physical parameters

Size: 10*10*8.3 cm

Weight: 1 kg with batteries

Temperature range: -40 to 60 degrees Celsius

Waterproof: 1 m for 48 hours

A/D

Channel: 3

Input impedance: 100 kOhm

Full scale input: 4.1 Vpp @ gain 1

Type: Delta-Sigma

Sample rate: 200 Hz

ADC resolution : Typically 21.5 bits @ 100 sps

Time and base

GPS: GPS built-in

Typical stability and accuracy: <10 ms over 20 days without processing

Typical stability/accuracy: < 0.01 with processing (re-sampling)

Data storage

Storage type: SD card

Capacity: Up to 64 GByte

Recording type: Continuous

Power

Batteries: 2 x D cells or battery pack with 8 x D cells

Power: Max runtime with 2 batteries is up to 14 days

External power: 4.5 - 24 V

Connectors

Sensor: MIL-C-2684 A12-10S

Power/communication: MIL-C-2684 A10-07P

Chapter 10

Appendix 2

This appendix contains a list of dates, times, lattitudes, longitudes, depths and magnitudes for all events used during this study.

NR date time LAT LON DEP MAG

1 120223 38:38.7 33.3383S 19.2696E 1.29 -1.4

2 120224 28:50.6 33.3231S 19.1577E 0.53 -1.57

3 120224 01:51.4 33.3182S 19.2820E 0.81 -0.41

4 120226 49:14.4 33.3527S 19.2867E 1.69 -1.6

5 120226 31:50.0 33.3846S 19.3708E 1.61 -1.1

6 120227 49:14.4 33.3060S 19.2644E 2.09 -1.28

7 120227 51:30.0 33.3230S 19.0915E 5.95 -1.41

8 120228 21:48.3 33.2763S 19.2132E 6.69 -1.62

9 120301 05:22.3 33.3243S 19.2606E 1.06 -0.03

10 120302 04:58.4 33.2275S 19.1678E 9.68 -1.74

11 120302 17:06.9 33.2874S 19.2182E 1.13 -0.99

12 120303 28:04.1 33.3491S 19.2820E 2.37 -1.1

13 120303 07:24.7 33.3552S 19.3428E 4.7 -1.28

14 120304 22:32.2 33.2973S 19.2384E 2.88 0.43

15 120304 17:07.8 33.3822S 19.3575E 1.72 -1.44

16 120304 50:32.5 33.3519S 19.2801E 2.17 -1.05

17 120305 54:18.3 33.2256S 19.1458E 11.1 -1.6

18 120305 03:33.7 33.2913S 19.2379E 0.73 -1.23

19 120306 30:49.5 33.2246S 19.1468E 10.69 -1.68

20 120306 57:42.5 33.3680S 19.3589E 1.94 -1.05

21 120306 03:12.7 33.3452S 19.1512E 0.15 -1.14

22 120307 21:52.5 33.2969S 19.2521E 0.55 -1.66

23 120307 25:32.5 33.3108S 19.2600E 2.38 -1.31

24 120307 15:40.0 33.3487S 19.2826E 2.24 -0.87

25 120307 13:53.8 33.3567S 19.3357E 2.38 -1.1

26 120308 38:18.6 33.2970S 19.2357E 2.94 -1.63

27 120309 25:47.6 33.2964S 19.2377E 2.29 -1.58

28 120309 48:38.0 33.3499S 19.2830E 3.07 -1.28

29 120309 41:58.0 33.2970S 19.2546E 0.13 -1.29

30 120309 22:22.0 33.3801S 19.3417E 5.1 -1.2

31 120310 26:18.2 33.3651S 19.3587E 1.99 -0.99

32 120311 15:13.0 33.2538S 19.1611E 10.51 -1.5

33 120312 04:33.8 33.2924S 19.2376E 0.67 -0.92

34 120312 48:11.5 33.2749S 19.1805E 4.21 -1.11

35 120313 01:46.8 33.3556S 19.2961E 2.88 -1.53

36 120313 16:47.3 33.2957S 19.2201E 7.95 -1.5

37 120313 39:43.0 33.2221S 19.1606E 9.5 -1.36

38 120313 47:33.1 33.2361S 19.1152E 11.13 -1.65

39 120313 27:11.0 33.3008S 19.1633E 2.16 -1.32

40 120314 15:34.0 33.3448S 19.2766E 2.17 -1.49

41 120314 03:07.3 33.2999S 19.2523E 1.89 -1.16

42 120314 57:55.4 33.2537S 19.1573E 8.72 -1.42

43 120316 45:14.1 33.3490S 19.3311E 3.66 -1.34

44 120317 12:16.1 33.2974S 19.2355E 2.74 -1.32

45 120317 51:15.1 33.3475S 19.2718E 3.18 -1.88

46 120318 31:41.3 33.2215S 19.1616E 9.61 -1.37

47 120318 12:50.5 33.3020S 19.2430E 2.5 -1.36

48 120318 27:21.2 33.2296S 19.1101E 14.05 -1.29

```
49 120318 26:21.2 33.3177S 19.2812E 1.71 -1.05
50 120319 55:03.7 33.2838S 19.2596E 2.99 -0.87
51 120321 32:28.6 33.3285S 19.3022E 3.95 -1.63
52 120321 12:06.5 33.2360S 19.1464E 11.58 -1.48
53 120321 30:44.3 33.3479S 19.3236E 2.21 -0.56
54 120322 32:55.2 33.2526S 19.1774E 8.97 -1.66
55 120323 38:13.6 33.2920S 19.2405E 4.55 -1.28
56 120324 44:40.4 33.3261S 19.1763E 1.49 -1.5
57 120325 51:43.5 33.2819S 19.1538E 11.3 -1.26
58 120325 26:28.9 33.2084S 19.1521E 3.91 -1.25
59 120325 58:54.6 33.3156S 19.2734E 1.04 -1.3
60 120326 59:17.6 33.3841S 19.3723E 4.28 -0.97
61 120327 10:28.0 33.2817S 19.1473E 11.97 -0.87
62 120327 08:08.4 33.3001S 19.2556E 1.95 -1.67
63 120330 39:13.6 33.3167S 19.2814E 0.22 -1.16
64 120331 51:28.9 33.3316S 19.3063E 2.45 1.66
65 120331 13:25.2 33.3352S 19.3044E 2.38 -1.47
66 120401 50:14.3 33.3877S 19.3156E 1.99 -1.53
67 120401 03:11.6 33.3542S 19.3186E 3.16 -1.61
68 120402 32:38.6 33.3321S 19.3059E 2.28 -1.25
69 120403 26:11.0 33.2387S 19.1723E 10.91 -1.9
70 120404 51:33.2 33.3124S 19.2734E 2.01 -1.14
71 120404 19:52.9 33.3720S 19.3551E 1.75 -0.68
72 120404 40:13.1 33.3083S 19.2671E 2.17 -1.21
73 120405 25:20.8 33.3563S 19.3342E 1.83 -0.58
74 120405 01:09.4 33.3541S 19.3365E 1.96 -0.66
75 120405 17:20.8 33.3561S 19.3343E 1.9 -0.37
76 120405 04:04.6 33.3463S 19.3183E 3.44 -1.08
77 120405 41:11.5 33.3391S 19.2829E 2.44 -1.19
78 120408 55:27.7 33.2254S 19.2343E 9.22 -1.2
79 120409 32:42.2 33.2501S 19.1368E 10.22 -1.05
80 120413 00:37.2 33.3497S 19.1736E 15.38 NaN
81 120413 48:37.5 33.3211S 19.2572E 2.92 -1.66
```

82 120414 57:37.4 33.3120S 19.2661E 2.12 -1.45

83 120415 26:16.2 33.3484S 19.2832E 2.66 -1.95

84 120415 17:19.9 33.2190S 19.1283E 10.55 -1.7

85 120416 22:49.3 33.3706S 19.1991E 8.85 0.09

86 120416 56:41.4 33.3407S 19.3088E 3.45 -1.22

87 120416 47:52.2 33.3606S 19.3123E 2.79 -1.38

88 120416 15:50.5 33.3563S 19.3482E 4.96 -1.29

89 120417 22:49.4 33.3441S 19.2799E 1.35 -1.25

90 120417 26:21.1 33.3470S 19.2795E 1.69 -1.39

91 120417 56:41.6 33.2159S 19.3098E 29.39 -1.49

92 120417 49:23.4 33.3303S 19.2593E 2.01 -1.54

93 120417 12:13.0 33.3249S 19.2671E 2.66 -0.97

94 120418 25:58.6 33.3478S 19.2792E 2.92 -1.14

95 120419 33:12.2 33.3330S 19.2542E 3.57 -1.43

96 120420 06:51.8 33.3349S 19.2639E 1.49 -1.79

97 120420 29:45.9 33.3395S 19.1502E 8.22 -1.18

98 120422 10:16.6 33.3545S 19.2719E 2.16 -1.85

99 120422 14:17.7 33.2325S 19.1254E 11.31 -1.66

100 120422 41:53.6 33.3280S 19.2872E 1.92 -1.22

101 120422 53:28.5 33.3201S 19.2824E 2 -1.66

102 120422 58:27.7 33.2999S 19.2211E 6.96 -1.67

103 120423 10:02.7 33.3415S 19.2731E 2.18 -1.72

104 120425 43:18.4 33.3245S 19.2923E 0.21 0.33

105 120426 33:40.1 33.2980S 19.2415E 7.44 -0.28

106 120426 00:48.4 33.2324S 19.1815E 2.77 NaN

107 120426 41:53.6 33.2445S 19.1536E 5.46 -1.87

108 120427 10:44.0 33.2124S 19.1461E 10.76 -1.36

109 120427 48:29.5 33.3721S 19.2773E 1.4 -1.72

110 120428 33:02.4 33.2904S 19.2731E 3.73 -1.71

111 120429 34:47.5 33.3569S 19.3439E 2.36 -0.23

112 120429 48:59.2 33.3946S 19.3410E 0.43 -1.22

113 120429 09:47.9 33.3628S 19.3486E 2.05 -0.9

114 120429 11:25.2 33.3734S 19.3398E 1.09 -1.05

115 120430 41:06.8 33.3226S 19.2001E 3.87 -1.61

116 120501 20:45.8 33.3250S 19.2903E 5.91 -0.69

117 120501 32:29.1 33.3102S 19.2640E 5.73 -1.46

118 120501 07:45.6 33.3055S 19.2520E 1.31 -1.16

119 120502 26:33.0 33.3328S 19.3133E 3.52 -1.61

120 120503 28:59.5 33.3709S 19.3130E 0.05 -0.84

121 120504 47:28.9 33.2756S 19.1463E 12.13 -1.29

122 120504 29:44.4 33.2390S 19.1460E 4.27 -1.98

123 120505 57:43.5 33.3229S 19.2942E 3.85 -1.36

124 120505 21:53.4 33.3106S 19.2656E 1.21 -0.96

125 120505 30:44.5 33.2951S 19.3262E 6.88 -1.6

126 120505 28:12.9 33.2173S 19.1540E 9.58 -1.25

127 120506 24:01.5 33.3112S 19.2633E 3.77 -1.26

128 120506 42:00.5 33.2556S 19.1473E 6.01 -1.74

129 120507 31:10.6 33.3188S 19.2810E 1.36 -0.94

130 120507 06:17.8 33.3008S 19.2545E 2.28 -1.25

131 120508 15:06.7 33.2396S 19.1380E 13.3 -1.69

132 120509 57:34.3 33.3603S 19.3364E 1.99 -1.03

133 120509 22:56.1 33.3714S 19.3541E 4.03 -0.3

134 120509 29:19.8 33.2243S 19.1825E 8.36 -1.63

135 120510 58:32.9 33.3140S 19.2703E 0.93 -0.72

136 120511 19:32.4 33.3017S 19.2351E 6.84 0.31

137 120511 20:27.4 33.2918S 19.1450E 3.77 -0.77

138 120511 06:16.1 33.1974S 19.1389E 10.72 -1.31

139 120511 38:13.7 33.3652S 19.3109E 4.3 -1.15

140 120512 51:31.6 33.3319S 19.3074E 2.39 -0.37

141 120512 56:10.1 33.3392S 19.2814E 2.09 -0.99

142 120512 08:21.3 33.3121S 19.2516E 1.6 -1.59

143 120512 46:00.1 33.2204S 19.1215E 11.81 -1.02

144 120514 16:20.3 33.3275S 19.2778E 1.99 -1.15

145 120514 15:23.2 33.3243S 19.1577E 2.28 -0.87

146 120514 17:20.8 33.3018S 19.2559E 2.26 -1.56

147 120515 57:34.2 33.2697S 19.0948E 15 -1.3

148 120515 01:12.9 33.2276S 19.1393E 6.51 -1.54

149 120516 02:57.9 33.3343S 19.3086E 3.82 -1.27

150 120516 49:27.4 33.2478S 19.1362E 12.93 -1.3

151 120516 38:09.4 33.2725S 19.1257E 13.46 -1.69

152 120516 56:29.8 33.3421S 19.2963E 2.58 -1.27

153 120517 05:42.7 33.3442S 19.2759E 2.35 -1.09

154 120518 43:55.0 33.2285S 19.1604E 6.94 -1.86

155 120519 15:55.9 33.3126S 19.2683E 4.56 -1.44

156 120519 25:41.3 33.1951S 19.1788E 8.36 -1.67

157 120520 21:00.5 33.3597S 19.2818E 0.66 -1.96

158 120520 23:54.6 33.3097S 19.2611E 3.2 -1.84

159 120520 16:48.2 33.2931S 19.2395E 1.65 -1.39

160 120520 39:28.9 33.3245S 19.2914E 1.83 -0.89

161 120521 35:56.4 33.3147S 19.2789E 5.43 -1.21

162 120522 15:39.6 33.2363S 19.1353E 7.58 -1.71

163 120522 27:22.2 33.2938S 19.2670E 2.84 -1.17

164 120523 14:04.0 33.3140S 19.2761E 5.5 -1.59

165 120523 40:21.9 33.3045S 19.2811E 1.95 -1.63

166 120523 32:30.5 33.3148S 19.2799E 4.89 -0.73

167 120524 06:01.3 33.2300S 19.1880E 12.23 -1.31

168 120524 31:50.7 33.3729S 19.3702E 1.85 0.38

169 120524 29:50.6 33.3196S 19.1754E 28.75 -1.15

170 120524 50:50.0 33.2522S 19.1443E 10.67 -1.64

171 120526 50:43.7 33.3028S 19.2492E 1.24 -0.53

172 120526 11:28.5 33.2461S 19.1091E 11.14 -1.55

Chapter 11

Appendix 3

This appendix contains the station numbers togehter with their longitude, lattitude and altitude (in meters above mean sea level).

Station	Long	Lat	Alt
ST01	19.1921	-33.2266	551
ST02	19.2262	-33.3567	526
ST03	19.1857	-33.2681	381
ST04	19.1902	-33.1743	500
ST05	19.1115	-33.2257	216
ST06	19.0981	-33.2373	237
ST07	19.2896	-33.4995	645
ST08	19.0898	-33.3126	177
ST09	19.0898	-33.3249	535
ST10	19.1368	-33.3864	233
ST11	19.1368	-33.4076	377
ST12	19.3577	-33.3989	480
ST13	19.2865	-33.3411	473
ST14	19.3176	-33.2612	575
ST15	19.2699	-33.1813	923

Chapter 12

Appendix 4

This appendix contians the P- and S-arrival times of all the events during this study for each station on which a pick could be made for a particular event. The event numbers corresponds to those of Appendix 2.

1
ST02 P 0.903
ST02 S 1.383
ST09 P 1.093
ST09 S 1.783
ST13 P 0.673
ST13 S 0.793
2
ST02 P 1.6
ST02 S 2.46
ST03 P 1.3
ST03 S 2.09
ST09 P 1.02
ST09 S 1.45
ST10 P 0.91

```
ST10 S 2.5
3
ST01 P 2.804
ST01 S 5.374
ST02 P 1.314
ST02 S 1.914
ST03 P 2.034
ST05 P 3.564
ST05 S 5.824
ST07 P 3.604
ST07 S 5.984
ST08 P 3.414
ST08 S 5.674
ST09 P 1.294
ST09 S 3.764
ST11 P 2.024
ST11 S 3.224
ST13 P 0.724
ST13 S 1.064
ST14 P 1.724
ST15 P 3.114
ST15 S 5.494
4
ST13 P 0.641
ST13 S 1.011
ST02 P 1.101
ST02 S 1.711
ST11 P 1.581
ST11 S 2.501
ST09 P 1.531
ST09 S 2.421
ST12 P 1.671
ST12 S 2.701
```

```
5
ST12 P 0.504
ST12 S 0.784
ST13 P 2.044
ST13 S 3.764
ST11 S 0.424
ST07 P 2.584
ST07 S 4.104
ST02 P 2.744
ST02 S 4.504
ST09 P 3.174
ST09 S 3.294
ST14 P 3.184
ST14 S 4.734
6
ST03 P 1.678
ST03 S 2.318
ST09 P 1.138
ST09 S 1.648
ST02 P 1.398
ST02 S 2.128
ST14 P 1.808
ST14 S 2.108
ST13 P 1.168
ST13 S 1.678
7
ST01 P 3.087
ST01 S 4.907
ST02 P 2.807
ST02 S 4.667
ST03 P 2.517
ST03 S 4.127
ST05 P 2.367
```

```
ST05 S 3.917
ST08 P 1.057
ST08 S 2.347
ST09 P 2.597
ST09 S 4.457
ST10 P 2.297
ST10 S 3.737
8
ST03 P 1.565
ST03 S 2.625
ST09 P 1.875
ST09 S 3.175
ST01 P 1.875
ST01 S 3.235
ST02 P 2.325
ST02 S 3.845
ST05 P 1.515
ST05 S 2.665
ST04 P 1.605
ST04 S 3.915
9
ST02 P 0.928
ST02 S 1.358
ST09 P 0.978
ST09 S 1.438
ST13 P 0.868
ST13 S 1.298
ST11 P 1.698
ST11 S 2.658
ST03 P 1.878
ST03 S 3.048
ST14 P 2.058
ST14 S 3.108
```

```
ST10 P 2.518
ST10 S 4.318
ST12 P 2.398
ST12 S 3.728
ST01 P 2.668
ST08 P 2.828
ST08 S 5.118
ST15 P 3.258
ST05 P 3.348
ST05 S 5.408
ST04 P 3.648
ST07 P 3.458
ST07 S 5.918
10
ST01 P 2.181
ST01 S 3.081
ST03 P 2.061
ST03 S 3.051
ST05 P 1.831
ST05 S 2.731
ST04 P 2.191
ST04 S 3.261
ST09 P 2.741
ST09 S 4.261
11
ST03 P 0.689
ST03 S 1.279
ST09 P 0.839
ST09 S 1.319
ST02 P 1.469
ST02 S 2.369
ST01 P 1.749
ST01 S 2.649
```

```
ST05 P 2.309
ST05 S 3.839
12
ST13 P 0.734
ST13 S 1.054
ST02 P 1.124
ST02 S 1.714
ST09 P 1.454
ST09 S 2.214
ST12 P 1.824
ST12 S 2.764
13
ST13 P 1.57
ST13 S 2.39
ST12 P 1.36
ST12 S 2
ST02 P 2.26
ST02 S 3.66
ST11 P 2.25
ST11 S 3.49
ST09 P 2.59
ST09 S 4.04
ST07 P 3
ST07 S 4.74
ST03 P 3.41
ST15 P 4.28
ST08 P 4.54
ST08 S 7.3
ST05 P 4.88
ST05 S 7.82
14
ST09 P 0.961
ST09 S 1.451
```

```
ST03 P 1.231
ST03 S 1.901
ST02 P 1.381
ST02 S 2.191
ST13 P 1.621
ST13 S 2.441
ST01 P 1.911
ST01 S 3.301
ST14 P 2.051
ST14 S 3.081
ST11 P 2.251
ST11 S 3.671
ST10 P 2.581
ST10 S 4.201
ST08 P 2.631
ST08 S 4.401
ST05 P 2.711
ST05 S 4.311
ST15 P 2.811
ST15 S 4.511
ST04 P 2.891
ST04 S 4.621
ST12 P 3.111
ST07 P 4.031
15
ST12 P 0.456
ST12 S 0.706
ST11 P 2.396
ST11 S 3.956
ST13 P 1.996
ST13 S 2.866
ST07 P 2.526
ST07 S 4.066
```

```
ST09 P 3.136
ST09 S 3.376
16
ST02 P 1.075
ST02 S 1.725
ST13 P 0.725
ST13 S 1.045
ST12 P 1.805
ST12 S 2.045
ST09 P 1.435
ST09 S 2.185
ST07 P 2.955
ST07 S 4.805
17
ST05 P 2.076
ST05 S 3.006
ST01 P 2.496
ST01 S 3.606
ST03 P 2.376
ST03 S 3.476
ST04 P 2.466
ST04 S 3.646
ST09 P 3.046
ST09 S 4.616
ST02 P 3.636
ST02 S 5.476
18
ST09 P 0.861
ST09 S 1.261
ST03 P 1.121
ST03 S 1.741
ST02 P 1.481
ST02 S 2.301
```

```
ST14 P 1.871
ST14 S 3.021
19
ST05 S 2.773
ST01 P 2.413
ST01 S 3.493
ST03 P 2.313
ST03 S 3.403
ST04 P 2.353
ST04 S 3.543
ST09 P 3.053
ST09 S 4.573
ST02 S 5.543
20
ST12 P 0.811
ST13 P 1.661
ST13 S 2.541
ST11 P 2.241
ST02 P 2.451
ST02 S 3.631
ST07 P 2.841
ST07 S 4.451
ST09 P 2.831
ST09 S 4.241
ST14 P 2.761
ST14 S 3.421
21
ST10 S 9.642
ST02 P 1.482
ST02 S 2.122
ST09 P 1.192
ST09 S 1.522
ST03 P 1.942
```

```
ST03 S 2.962
22
ST09 P 0.958
ST09 S 1.368
ST13 P 0.888
ST13 S 2.098
ST02 P 1.378
ST02 S 2.198
ST03 P 1.388
ST03 S 2.148
ST14 P 1.858
ST14 S 2.758
23
ST09 P 1.05
ST09 S 1.56
ST13 P 1.13
ST13 S 1.7
ST02 P 1.26
ST02 S 1.86
ST03 P 1.71
ST03 S 2.83
ST14 P 1.9
ST14 S 2.48
24
ST13 P 0.709
ST13 S 1.019
ST02 P 1.129
ST02 S 1.759
ST09 P 1.449
ST09 S 2.199
ST12 P 1.809
ST03 P 2.359
ST07 P 2.999
```

```
ST07 S 4.649
25
ST13 P 1.271
ST13 S 1.941
ST12 P 1.111
ST12 S 1.581
ST02 P 2.041
ST02 S 3.071
ST11 P 2.051
ST11 S 3.201
ST14 P 2.431
ST09 P 2.401
ST09 S 3.581
ST07 P 2.721
ST07 S 4.561
ST03 P 3.861
26
ST09 P 0.968
ST09 S 1.368
ST03 P 1.278
ST03 S 1.868
ST02 P 1.418
ST02 S 2.168
ST13 P 1.588
ST13 S 2.518
ST01 P 1.938
ST01 S 3.058
ST14 P 2.208
27
ST09 P 0.917
ST09 S 1.337
ST03 P 1.247
ST03 S 1.817
```

```
ST02 P 1.377
ST02 S 2.117
ST13 P 1.617
ST13 S 2.447
ST01 S 2.997
ST14 P 2.147
ST08 S 4.407
ST10 P 2.567
ST05 P 2.737
ST05 S 4.397
28
ST13 P 0.87
ST13 S 1.25
ST02 P 1.18
ST02 S 1.9
ST11 S 2.28
ST09 P 1.51
ST09 S 2.41
ST12 P 1.87
ST12 S 2.75
29
ST09 P 0.982
ST09 S 1.462
ST13 P 1.292
ST13 S 1.992
ST03 P 1.382
ST03 S 2.162
ST02 P 1.382
ST02 S 2.132
ST14 P 1.742
ST14 S 2.552
30
ST12 P 1.147
```

```
ST12 S 1.677
ST13 P 1.537
ST13 S 2.717
ST11 P 2.127
ST11 S 3.187
ST02 P 2.347
ST02 S 3.707
ST07 P 2.547
ST07 S 4.007
ST09 P 2.757
ST09 S 4.267
31
ST12 P 0.869
ST12 S 1.209
ST13 P 1.649
ST13 S 2.479
ST11 P 2.229
ST11 S 3.479
ST02 P 2.419
ST02 S 3.619
ST14 P 2.709
ST14 S 3.219
ST09 P 2.799
ST09 S 4.229
ST07 P 2.889
ST07 S 4.479
32
ST03 P 2.063
ST03 S 2.983
ST01 P 2.163
ST05 P 2.133
ST05 S 3.143
ST04 P 2.623
```

```
ST04 S 3.993
ST09 P 2.573
ST02 P 3.103
33
ST09 P 0.881
ST09 S 1.261
ST03 P 1.041
ST03 S 1.551
ST02 P 1.371
ST02 S 2.321
ST13 P 1.521
ST13 S 2.421
ST01 P 1.741
ST14 P 1.861
ST11 P 2.401
ST11 S 3.841
ST05 P 2.671
ST05 S 4.331
ST15 P 2.771
ST15 S 4.481
ST04 P 2.801
ST04 S 4.521
ST12 P 3.131
ST12 S 5.181
34
ST03 P 0.908
ST03 S 1.208
ST01 P 1.738
ST01 S 2.358
ST09 P 1.488
ST09 S 2.238
ST02 P 2.078
ST02 S 3.238
```

```
35
ST13 P 0.911
ST13 S 1.281
ST12 P 1.571
ST12 S 2.341
ST02 P 1.381
ST02 S 2.111
ST09 P 1.741
ST09 S 2.711
ST14 P 2.441
ST14 S 6.011
36
ST03 P 1.682
ST03 S 2.552
ST09 P 1.672
ST09 S 2.542
ST01 P 3.382
ST02 P 2.012
ST02 S 3.172
ST13 P 2.322
ST13 S 3.602
ST14 P 2.662
ST14 S 4.112
ST05 P 2.702
ST05 S 4.232
ST04 P 3.002
ST04 S 4.762
ST15 P 3.072
ST15 S 4.982
37
ST01 P 2.049
ST01 S 3.089
ST03 P 2.109
```

```
ST03 S 3.139
ST05 P 1.919
ST05 S 2.909
ST04 P 2.109
ST04 S 3.159
ST09 P 2.879
ST09 S 4.419
ST15 P 3.129
ST15 S 4.789
ST02 P 3.399
ST02 S 5.319
ST14 P 3.669
ST14 S 5.529
ST13 P 3.869
38
ST05 P 0.546
ST05 S 3.056
ST03 P 2.556
ST03 S 3.676
ST01 P 2.716
ST01 S 3.936
ST04 P 2.776
ST04 S 4.076
ST09 P 3.126
ST09 S 4.676
ST02 P 3.716
ST02 S 5.556
39
ST03 P 0.983
ST03 S 1.353
ST09 P 1.133
ST09 S 1.673
ST08 P 1.113
```

ST08 S 2.373

ST02 P 1.723

ST02 S 2.693

ST01 P 1.653

ST01 S 2.813

40

ST13 P 0.7

ST13 S 1

ST02 P 1.04

ST02 S 1.57

ST09 P 1.34

ST09 S 2

ST12 P 1.95

ST12 S 2.96

ST14 P 2.23

ST14 S 3.29

41

ST09 P 0.924

ST09 S 1.504

ST13 P 1.394

ST13 S 2.104

ST02 P 1.384

ST02 S 2.274

ST03 P 1.594

ST03 S 2.354

ST14 P 1.734

ST14 S 2.744

42

ST03 P 1.842

ST03 S 2.672

ST01 P 1.852

ST01 S 3.072

ST05 P 1.862

```
ST05 S 2.712
ST08 S 3.392
ST09 P 2.402
ST09 S 3.622
ST04 P 2.432
ST04 S 3.702
ST02 P 2.852
ST02 S 4.512
ST14 P 3.622
ST14 S 5.542
43
ST13 P 1.284
ST13 S 1.974
ST12 P 1.394
ST12 S 2.084
ST11 P 0.934
ST11 S 3.284
ST02 P 2.004
ST02 S 3.234
ST09 P 2.364
ST09 S 3.674
ST07 P 3.034
ST07 S 4.814
44
ST09 P 0.926
ST09 S 1.376
ST03 P 1.266
ST03 S 1.846
ST02 P 1.396
ST02 S 2.196
ST13 P 1.706
45
ST13 P 0.915
```

```
ST13 S 1.355
ST02 P 1.065
ST02 S 1.575
ST09 P 1.355
ST09 S 1.985
46
ST01 P 2.023
ST01 S 3.093
ST03 P 2.143
ST03 S 3.183
ST05 P 1.943
ST05 S 2.893
ST04 P 2.133
ST04 S 3.203
ST08 P 2.753
ST08 S 4.153
ST09 P 2.903
ST09 S 4.453
ST02 P 3.433
ST02 S 5.343
ST14 P 3.733
ST14 S 5.493
47
ST09 P 0.924
ST09 S 1.304
ST03 P 1.394
ST03 S 2.094
ST02 P 1.314
ST02 S 2.064
ST13 P 1.464
ST13 S 2.294
ST14 P 1.874
ST14 S 3.284
```

```
ST11 P 2.214
48
ST05 P 2.455
ST05 S 3.485
ST03 P 2.995
ST03 S 4.295
ST01 P 3.155
ST01 S 4.545
ST08 P 2.945
ST08 S 4.205
ST04 P 3.105
ST04 S 4.495
ST09 P 3.555
ST09 S 5.105
ST02 P 4.005
ST02 S 6.045
49
ST13 P 0.817
ST09 P 1.347
ST09 S 1.997
ST02 P 1.357
ST02 S 1.997
ST14 P 1.757
ST14 S 2.647
ST03 P 2.067
ST03 S 3.097
ST11 P 2.037
ST11 S 2.947
ST12 P 2.297
ST12 S 3.527
ST07 P 3.627
ST07 S 5.637
50
```

```
ST09 P 1.381
ST09 S 1.981
ST03 P 1.551
ST03 S 2.271
ST14 P 1.501
ST02 P 1.761
ST02 S 2.661
ST01 P 1.581
ST01 S 3.071
ST04 P 1.891
51
ST13 P 1.079
ST13 S 1.579
ST02 P 1.659
ST02 S 2.569
ST09 P 1.799
ST09 S 2.779
ST11 P 2.059
ST11 S 3.219
ST12 P 1.989
ST03 P 2.549
ST03 S 3.979
ST07 P 3.369
ST07 S 5.329
ST15 P 3.409
ST15 S 5.299
ST05 P 3.999
ST05 S 6.459
52
ST03 P 2.367
ST03 S 3.457
ST01 P 2.487
ST01 S 3.647
```

```
ST05 P 2.157
ST05 S 3.217
ST04 P 2.617
ST04 S 3.887
ST09 P 2.957
ST09 S 4.477
ST02 P 3.457
ST02 S 5.357
ST14 P 4.037
53
ST13 P 1.02
ST13 S 1.53
ST12 P 1.33
ST12 S 1.95
ST02 P 1.82
ST02 S 2.72
ST11 P 1.93
ST11 S 2.65
ST09 P 2.13
ST09 S 3.11
ST14 P 2.23
ST14 S 3.51
ST07 P 3.01
ST07 S 4.8
ST03 P 3.02
ST01 P 3.38
ST15 P 3.86
ST08 P 4.09
ST08 S 6.64
ST05 P 4.51
ST05 S 7.38
54
ST03 P 1.786
```

ST03 S 2.616

ST01 P 1.996

ST01 S 2.946

ST05 P 2.036

ST05 S 3.056

ST09 P 2.326

ST09 S 3.606

ST04 P 2.386

ST04 S 3.706

ST02 P 2.716

ST02 S 4.396

55

ST09 P 1.251

ST09 S 1.861

ST03 P 1.431

ST03 S 2.151

ST02 P 1.651

ST02 S 2.571

ST01 P 1.811

ST01 S 3.351

ST13 P 1.981

ST13 S 3.041

ST14 P 2.371

ST05 P 2.761

ST05 S 4.331

ST11 P 2.361

ST04 P 2.891

ST04 S 4.741

56

ST08 P 1.29

ST08 S 2.5

ST09 P 0.73

ST09 S 1.01

```
ST02 P 1.21
ST02 S 1.87
ST03 P 1.37
ST03 S 2.04
ST13 P 0.3
ST13 S 1.98
57
ST03 P 2.22
ST03 S 3.23
ST05 P 2.42
ST05 S 3.51
ST01 P 2.62
ST01 S 3.92
ST09 P 2.48
ST09 S 3.68
ST02 P 2.84
ST02 S 4.33
ST04 P 2.86
ST04 S 4.65
58
ST05 P 0.912
ST05 S 1.332
ST01 P 1.392
ST04 P 1.252
ST04 S 1.432
ST03 P 1.502
ST03 S 2.262
59
ST13 P 0.815
ST13 S 1.235
ST09 P 1.175
ST09 S 1.725
ST02 P 1.235
```

```
ST14 P 1.775
ST11 P 2.005
ST11 S 3.305
ST03 P 1.905
ST12 P 2.425
ST12 S 3.825
60
ST12 P 0.978
ST12 S 1.318
ST13 P 2.148
ST13 S 3.268
ST11 P 2.458
ST11 S 3.788
ST02 P 2.788
ST02 S 4.618
ST07 P 2.668
ST07 S 4.108
ST09 P 3.228
ST09 S 5.048
ST14 P 3.228
ST14 S 4.928
ST03 P 4.178
ST03 S 6.848
ST08 P 5.138
ST08 S 8.328
ST05 P 5.608
ST05 S 8.938
61
ST03 P 2.378
ST03 S 3.468
ST08 P 2.328
ST08 S 3.438
ST09 P 2.608
```

```
ST09 S 3.898
ST05 P 2.498
ST05 S 3.738
ST01 P 2.768
ST01 S 4.138
ST02 P 2.938
ST02 S 4.558
ST13 P 3.558
ST04 P 3.168
ST04 S 4.948
ST14 P 4.068
ST14 S 6.218
ST07 P 5.218
62
ST09 P 1.014
ST09 S 1.524
ST13 P 1.094
ST13 S 2.334
ST02 P 1.274
ST02 S 2.434
ST03 P 1.594
ST14 P 1.774
ST14 S 2.934
63
ST13 P 0.72
ST13 S 1.03
ST09 P 1.29
ST09 S 1.95
ST02 P 1.32
ST02 S 1.95
ST14 P 1.65
ST14 S 2.53
ST03 P 1.99
```

ST03 S 2.5

64

ST13 P 0.857

ST13 S 1.207

ST02 P 1.607

ST02 S 2.407

ST09 P 1.797

ST09 S 2.857

ST11 P 1.997

ST11 S 3.147

ST12 P 1.817

ST12 S 2.747

ST14 P 1.957

ST14 S 2.897

ST03 P 2.577

ST03 S 4.087

ST01 P 3.127

ST07 P 3.267

ST07 S 5.187

ST15 P 3.357

ST15 S 5.287

ST08 P 3.837

ST08 S 6.227

ST04 P 4.157

ST05 P 4.057

ST05 S 6.547

65

ST13 P 0.808

ST13 S 1.188

ST02 P 1.568

ST02 S 2.368

ST09 P 1.738

ST09 S 2.688

```
ST12 P 1.748
ST12 S 2.678
ST14 P 2.168
ST14 S 2.858
66
ST12 P 0.933
ST12 S 1.193
ST13 P 2.263
ST09 P 2.613
ST09 S 3.473
ST07 P 2.813
ST07 S 4.433
ST14 P 3.713
ST14 S 5.023
67
ST13 P 1.101
ST13 S 1.611
ST11 P 0.901
ST11 S 2.991
ST12 P 1.371
ST12 S 2.121
ST09 P 2.091
ST09 S 3.341
ST07 P 2.851
ST07 S 4.641
68
ST13 P 0.823
ST13 S 1.213
ST09 P 1.753
ST09 S 2.733
ST14 P 1.943
ST14 S 2.853
ST12 P 1.783
```

```
ST03 P 2.633
ST03 S 4.093
69
ST01 S 3.233
ST03 P 2.173
ST03 S 3.173
ST05 P 2.203
ST05 S 3.273
ST04 P 2.453
ST04 S 3.713
ST09 S 4.233
70
ST13 P 0.944
ST13 S 1.404
ST09 P 1.244
ST09 S 1.824
ST14 P 1.784
ST14 S 2.664
ST03 P 1.904
ST11 P 2.204
ST11 S 3.494
71
ST12 P 0.674
ST12 S 0.854
ST11 P 2.534
ST11 S 3.854
ST13 P 2.184
ST13 S 2.914
ST07 P 2.724
ST07 S 4.334
ST09 P 3.314
ST09 S 3.464
72
```

```
ST13 P 1.096
ST13 S 1.606
ST09 P 1.166
ST09 S 1.706
ST14 P 1.766
ST14 S 2.496
ST03 P 1.776
ST03 S 2.806
ST12 P 2.646
ST12 S 3.926
73
ST13 P 1.201
ST13 S 1.821
ST12 P 1.091
ST12 S 1.621
ST11 P 1.961
ST11 S 3.081
ST09 P 2.351
ST09 S 3.511
ST14 P 2.401
ST07 P 2.901
ST07 S 4.531
ST03 P 3.331
ST05 S 7.751
74
ST13 P 1.23
ST13 S 1.86
ST12 P 1.12
ST12 S 1.64
ST11 P 2.04
ST11 S 3.15
ST14 P 2.42
ST09 P 2.37
```

ST07 P 2.93

ST03 P 3.32

ST03 S 4.14

75

ST13 P 1.2

ST13 S 1.84

ST12 P 1.1

ST12 S 1.63

ST11 P 1.97

ST11 S 3.08

ST09 P 2.35

ST09 S 3.49

ST14 P 2.4

ST07 P 2.89

ST07 S 4.54

ST01 P 3.78

ST01 S 6.56

76

ST13 P 1.097

ST13 S 1.577

ST12 P 1.537

ST12 S 2.287

ST09 P 2.057

ST09 S 3.387

ST11 P 1.907

ST11 S 2.997

ST03 P 2.887

ST03 S 4.847

ST05 P 4.367

ST05 S 7.297

77

ST13 P 0.726

ST13 S 1.026

ST09 P 1.396

ST09 S 2.236

ST11 P 1.626

ST11 S 2.516

ST12 P 1.946

ST12 S 2.936

ST03 P 2.346

ST03 S 4.176

ST07 P 3.106

78

ST15 P 1.922

ST15 S 4.302

ST01 P 2.092

ST01 S 3.282

ST03 P 2.022

ST03 S 3.112

ST04 P 2.192

ST04 S 3.382

ST09 P 2.772

ST09 S 4.212

79

ST03 P 2.178

ST03 S 3.168

ST05 P 1.918

ST05 S 2.808

ST08 P 2.378

ST08 S 3.488

ST09 P 2.758

ST09 S 4.158

ST14 P 3.958

ST14 S 5.678

80

ST02 P 3.169

```
ST02 S 3.689
ST03 P 3.759
ST03 S 4.179
ST08 P 2.479
ST08 S 2.579
ST09 P 2.969
ST09 S 3.369
ST13 P 3.239
ST13 S 3.829
81
ST02 P 1.12
ST02 S 1.64
ST09 P 1
ST09 S 1.46
ST13 P 1.11
ST13 S 1.6
82
ST02 P 1.305
ST02 S 1.925
ST03 P 1.845
ST03 S 2.785
ST09 P 1.125
ST09 S 1.635
ST13 P 1.035
ST13 S 1.505
83
ST13 P 0.783
ST13 S 1.123
ST02 P 1.173
ST02 S 1.793
ST09 P 1.483
ST09 S 2.223
ST12 P 1.853
```

```
84
ST05 P 1.873
ST05 S 2.823
ST06 P 2.513
ST06 S 2.913
ST03 P 2.413
ST03 S 3.653
ST04 P 2.413
ST04 S 3.693
ST09 P 2.983
ST09 S 4.603
85
ST02 P 1.808
ST02 S 2.708
ST11 P 1.818
ST11 S 2.858
ST10 P 1.848
ST10 S 2.878
ST09 P 1.998
ST09 S 3.078
ST13 P 2.568
ST13 S 3.778
ST08 P 2.728
ST08 S 4.258
ST03 P 2.698
ST03 S 4.248
ST12 P 3.258
ST12 S 5.008
ST07 P 3.138
ST07 S 5.068
ST01 P 3.458
ST14 P 3.618
ST14 S 5.638
```

ST05 P 3.628

ST05 S 5.638

ST04 P 4.238

ST04 S 6.698

ST15 P 4.568

86

ST13 P 1.01

ST02 P 1.65

ST02 S 2.53

ST11 P 2.4

ST11 S 3.08

ST09 P 1.89

ST09 S 2.93

ST12 P 1.68

ST03 P 2.87

ST07 P 3.13

ST07 S 4.99

ST05 P 4.17

ST05 S 6.73

87

ST13 P 1.042

ST13 S 1.562

ST12 P 1.352

ST12 S 1.892

ST02 P 1.622

ST02 S 2.492

ST09 P 2.052

ST09 S 3.142

ST14 P 2.502

88

ST12 P 1.374

ST12 S 1.974

ST11 P 2.324

```
ST11 S 3.574
ST02 P 2.414
ST02 S 3.794
ST09 P 2.704
ST09 S 4.194
ST14 P 2.734
ST07 P 3.024
ST07 S 4.714
ST03 P 3.544
ST08 P 4.344
89
ST13 P 0.54
ST13 S 0.86
ST02 P 1.05
ST02 S 1.58
ST09 P 1.33
ST09 S 2.13
90
ST13 P 0.604
ST13 S 0.904
ST02 P 1.064
ST02 S 1.574
ST09 P 1.364
ST09 S 2.124
91
ST05 P 4.784
ST04 P 5.524
ST04 S 6.764
ST09 P 7.074
ST12 P 5.974
92
ST13 P 0.899
ST13 S 1.349
```

ST02 P 0.959

ST02 S 1.389

ST09 P 0.969

ST09 S 1.449

93

ST13 P 0.937

ST13 S 1.387

ST02 P 1.147

ST02 S 1.687

ST09 P 1.137

ST09 S 1.687

ST11 P 1.827

ST11 S 2.897

ST03 P 1.997

ST03 S 3.537

94

ST13 P 0.841

ST13 S 1.191

ST02 P 1.141

ST02 S 1.701

ST09 P 1.431

ST09 S 2.161

95

ST02 P 1.1

ST02 S 1.49

ST09 P 1.08

ST09 S 1.54

ST13 P 1.14

96

ST02 P 0.897

ST02 S 1.297

ST09 P 1.017

ST09 S 1.597

```
ST13 P 0.737
97
ST09 P 2.035
ST09 S 2.815
ST08 P 1.185
ST08 S 3.125
ST02 P 2.095
ST02 S 2.745
ST13 P 1.545
ST14 P 2.515
98
ST02 P 0.942
ST02 S 1.412
ST13 P 0.802
ST13 S 1.162
ST09 P 1.342
ST09 S 2.012
99
ST05 P 2.11
ST05 S 2.94
ST06 S 3.15
ST03 P 2.52
ST03 S 3.61
ST04 P 2.65
ST04 S 3.88
ST09 P 3.14
ST09 S 4.7
ST02 P 3.67
ST02 S 5.6
100
ST13 P 1.421
ST02 P 1.221
ST02 S 2.011
```

```
ST09 P 1.441
ST09 S 2.321
ST12 P 2.041
ST12 S 3.161
ST03 P 2.241
ST03 S 3.601
ST04 P 2.981
ST04 S 6.351
101
ST13 P 0.822
ST13 S 1.112
ST09 P 1.342
ST09 S 2.072
ST02 P 1.372
ST02 S 1.992
ST14 P 1.772
ST14 S 2.672
102
ST09 P 1.512
ST09 S 2.152
ST03 P 1.632
ST03 S 2.332
ST02 P 1.282
ST02 S 1.932
ST14 P 2.552
ST05 P 2.242
ST05 S 4.482
103
ST13 P 0.728
ST13 S 1.078
ST02 P 1.018
ST02 S 1.518
ST09 P 1.258
```

```
ST09 S 1.858
104
ST13 P 0.538
ST13 S 0.728
ST02 P 1.378
ST02 S 2.038
ST09 P 1.478
ST09 S 2.208
ST14 P 1.778
ST14 S 2.648
ST11 P 2.068
ST12 P 1.988
ST12 S 3.218
ST03 P 2.378
ST10 P 3.008
ST10 S 4.928
ST07 P 3.458
ST05 P 3.808
ST05 S 6.218
105
ST09 P 8.189
ST12 P 3.319
ST12 S 4.309
ST07 P 4.499
ST07 S 6.339
ST04 P 2.139
106
ST05 S 7.232
ST06 P 1.722
ST06 S 2.412
ST12 P 1.662
107
ST03 P 1.574
```

```
ST03 S 2.474
ST05 P 1.514
ST05 S 2.424
ST06 P 0.444
ST06 S 2.424
ST04 P 2.044
ST04 S 3.284
ST09 P 2.094
ST09 S 3.484
108
ST05 P 2.051
ST05 S 3.011
ST01 P 2.371
ST01 S 3.501
ST03 P 2.461
ST03 S 3.601
ST06 P 2.171
ST06 S 3.231
ST04 P 2.311
ST04 S 3.391
ST08 P 2.871
ST08 S 4.381
ST09 P 3.201
ST09 S 4.881
ST15 P 3.211
ST02 P 3.751
ST02 S 5.781
ST14 P 4.131
ST14 S 6.281
ST10 P 3.881
ST10 S 6.061
ST11 P 4.591
109
```

```
ST02 P 1.497
ST02 S 2.187
ST03 P 2.827
ST06 P 5.387
ST06 S 6.177
ST09 P 1.537
ST09 S 2.307
ST11 P 0.147
ST11 S 2.057
ST13 P 0.947
ST13 S 1.387
110
ST03 P 1.739
ST03 S 2.899
ST14 P 1.589
ST14 S 2.409
ST09 P 1.519
ST09 S 2.319
ST10 P 3.139
ST10 S 5.299
ST02 P 1.759
ST02 S 2.859
111
ST13 P 1.381
ST13 S 2.061
ST12 P 1.081
ST12 S 1.581
ST11 P 2.101
ST11 S 3.411
ST02 P 2.151
ST09 P 2.511
ST14 P 2.481
ST07 P 2.891
```

ST07 S 4.611

ST03 P 3.441

ST10 P 3.671

ST15 P 4.161

ST08 P 4.561

ST08 S 7.331

ST05 P 4.881

ST05 S 7.841

ST06 P 4.961

ST06 S 8.231

112

ST12 P 0.218

ST12 S 0.618

ST13 P 1.328

ST13 S 2.418

ST09 P 3.038

ST09 S 4.128

ST08 P 0.908

113

ST12 P 0.93

ST12 S 1.32

ST13 P 1.47

ST13 S 2.23

ST14 P 2.72

ST14 S 3.85

ST02 P 2.21

ST09 P 2.61

ST03 P 3.54

114

ST12 P 0.687

ST12 S 1.067

ST07 P 2.437

ST07 S 3.987

```
ST09 P 2.187
ST09 S 4.167
115
ST09 P 0.826
ST09 S 1.226
ST02 P 1.176
ST02 S 1.886
ST03 P 1.456
ST03 S 2.286
116
ST04 S 8.892
ST06 S 8.402
ST03 P 2.922
ST03 S 3.982
ST09 P 2.142
ST09 S 2.852
ST14 P 2.552
ST13 P 1.532
ST13 S 1.842
117
ST09 P 1.523
ST09 S 2.373
ST03 P 1.973
ST03 S 3.063
ST14 P 2.143
ST14 S 3.323
ST10 P 2.823
ST10 S 4.633
ST05 P 3.303
ST05 S 5.293
ST06 P 3.293
ST06 S 5.473
118
```

```
ST09 P 0.876
ST09 S 1.266
ST03 P 1.516
ST03 S 2.316
ST14 P 1.876
ST14 S 2.836
ST01 P 2.206
ST15 P 2.836
ST15 S 4.396
ST10 P 2.686
ST10 S 4.656
ST08 P 2.866
ST08 S 5.086
ST05 P 3.036
ST05 S 4.916
ST06 P 3.156
ST06 S 5.066
119
ST13 P 1.08
ST13 S 1.55
ST09 P 1.95
ST09 S 3.06
ST14 P 2.15
ST11 P 1.98
ST11 S 3.14
ST12 P 1.79
ST12 S 2.71
ST03 P 2.69
ST03 S 3.77
ST10 P 3.26
ST10 S 5.39
ST07 P 3.21
ST05 P 4.22
```

```
ST05 S 6.77
ST06 P 4.31
ST06 S 6.98
120
ST13 P 0.947
ST13 S 1.527
ST12 P 1.027
ST12 S 1.627
ST09 P 2.077
121
ST03 P 2.444
ST03 S 3.414
ST06 P 2.454
ST06 S 3.574
ST05 P 2.464
ST01 P 2.784
ST01 S 4.024
ST09 P 2.674
ST04 P 3.074
ST04 S 4.784
122
ST05 P 1.244
ST05 S 2.134
ST03 P 1.474
ST03 S 2.504
ST06 P 1.234
ST06 S 2.214
ST04 P 1.854
ST04 S 3.104
ST09 P 2.594
ST09 S 3.454
123
ST13 P 1.073
```

ST13 S 1.593

ST09 P 1.653

ST09 S 2.613

ST11 P 2.023

ST11 S 3.073

ST03 P 2.353

ST03 S 3.753

ST12 P 2.133

ST10 P 3.053

ST10 S 5.073

ST05 P 3.893

ST05 S 6.153

124

ST09 P 1.044

ST09 S 1.564

ST03 P 1.754

ST14 P 1.794

ST10 P 2.594

ST10 S 4.804

ST12 P 2.604

ST05 P 3.264

ST05 S 5.474

125

ST09 P 5.037

ST09 S 5.757

ST03 P 2.937

ST03 S 4.087

ST12 P 2.507

ST04 P 4.487

ST05 P 2.287

126

ST05 P 1.921

ST05 S 2.881

```
ST01 P 2.121
ST01 S 3.131
ST06 P 2.301
ST06 S 3.111
ST03 P 2.191
ST03 S 3.251
ST04 P 2.131
ST04 S 3.161
ST08 P 2.721
ST08 S 4.251
ST09 P 2.961
ST09 S 4.541
ST15 P 3.201
ST15 S 4.741
ST14 P 3.771
ST14 S 6.001
ST11 P 4.331
ST11 S 6.751
127
ST09 P 1.229
ST09 S 1.729
ST13 P 1.319
ST13 S 1.859
ST03 P 1.889
ST14 P 2.009
ST14 S 2.939
ST01 P 0.029
ST01 S 0.429
128
ST01 P 1.947
ST01 S 2.877
ST03 P 1.557
ST03 S 2.517
```

```
ST05 P 1.567
ST05 S 2.537
ST06 P 2.587
ST04 P 2.057
ST09 P 2.087
ST09 S 3.407
129
ST13 P 0.761
ST13 S 1.101
ST09 P 1.311
ST09 S 1.981
ST14 P 1.771
ST14 S 2.711
ST03 P 2.061
ST11 P 2.011
ST12 P 2.261
130
ST09 P 1.055
ST09 S 1.545
ST13 P 1.295
ST13 S 1.945
ST03 P 1.525
ST03 S 2.095
ST14 P 1.995
ST14 S 2.745
131
ST05 P 2.326
ST05 S 3.216
ST06 P 2.366
ST06 S 3.676
ST03 P 2.636
ST03 S 3.686
ST04 P 2.916
```

ST04 S 4.206

ST09 P 3.216

ST09 S 4.716

132

ST12 P 1.031

ST12 S 1.521

ST13 P 1.281

ST13 S 1.931

ST11 P 2.031

ST09 P 2.441

ST09 S 3.691

ST07 P 2.451

ST07 S 4.501

ST14 P 2.431

133

ST12 P 1.039

ST12 S 1.419

ST11 P 2.589

ST07 P 2.739

ST07 S 4.269

ST14 P 2.479

134

ST01 P 1.775

ST03 P 1.795

ST03 S 2.875

ST05 P 1.525

ST05 S 2.475

ST04 P 1.845

ST04 S 2.985

ST06 P 2.215

ST09 P 2.475

ST09 S 4.025

135

```
ST13 P 0.858
ST13 S 1.308
ST09 P 1.108
ST09 S 1.658
ST14 P 1.788
ST14 S 2.698
ST03 P 1.848
ST11 P 1.988
ST11 S 3.118
ST01 P 2.488
ST12 P 2.438
ST12 S 3.908
ST10 P 2.748
ST10 S 4.728
ST15 P 3.028
ST05 P 3.388
ST05 S 5.498
ST04 P 3.578
ST06 P 3.478
ST06 S 5.678
ST07 P 3.688
136
ST09 P 1.481
ST09 S 2.281
ST03 P 1.711
ST03 S 2.661
ST13 P 1.941
ST13 S 3.221
ST01 P 2.261
ST01 S 3.581
ST14 P 2.401
ST14 S 3.781
ST11 P 2.501
```

ST11 S 3.891

ST10 P 2.601

ST10 S 4.291

ST08 P 2.771

ST08 S 4.551

ST05 P 2.901

ST05 S 4.631

ST06 P 2.991

ST06 S 4.731

ST15 P 3.101

ST15 S 5.071

ST04 P 3.171

ST04 S 5.071

ST12 P 3.231

ST12 S 5.041

ST07 P 4.081

ST07 S 6.481

137

ST06 P 1.221

ST06 S 1.591

ST03 P 1.191

ST03 S 1.471

ST09 P 1.541

ST09 S 2.121

138

ST05 P 2.02

ST05 S 2.88

ST06 P 2.33

ST06 S 3.43

ST01 P 2.5

ST01 S 3.64

ST04 P 2.27

ST04 S 3.25

ST03 P 2.64

ST03 S 3.89

ST09 P 3.44

ST09 S 5.22

ST14 P 4.32

139

ST12 P 1.412

ST12 S 2.082

ST09 P 2.132

ST09 S 3.202

ST10 P 3.092

ST10 S 5.572

140

ST13 P 0.849

ST13 S 1.229

ST09 P 1.799

ST09 S 2.959

ST11 P 1.969

ST11 S 3.139

ST14 P 1.949

ST14 S 2.889

ST12 P 1.789

ST12 S 2.729

ST03 P 2.599

ST10 P 3.179

ST10 S 5.519

ST01 P 3.369

ST07 P 3.239

ST07 S 5.179

ST08 P 3.809

ST08 S 6.019

ST04 P 4.139

ST05 P 4.139

ST05 S 6.549

ST06 P 4.149

ST06 S 6.749

141

ST13 P 0.662

ST13 S 0.952

ST09 P 1.372

ST09 S 2.062

ST12 P 1.952

ST12 S 2.952

142

ST09 P 0.833

ST09 S 1.203

ST13 P 1.143

ST13 S 1.713

ST03 P 1.603

ST03 S 2.433

ST14 P 2.023

ST14 S 3.053

ST10 P 2.543

ST10 S 4.323

ST05 P 3.083

ST05 S 4.993

ST06 P 3.173

ST06 S 5.133

143

ST05 P 2.153

ST05 S 3.103

ST06 P 2.223

ST06 S 3.553

ST03 P 2.683

ST03 S 3.913

ST01 P 2.683

ST08 P 2.833

ST08 S 4.133

ST04 P 2.643

ST04 S 3.863

ST09 P 3.353

ST09 S 5.033

ST15 P 3.853

ST10 P 3.813

ST10 S 5.823

ST14 P 4.383

ST14 S 6.553

ST11 P 4.573

ST11 S 7.133

144

ST13 P 0.74

ST13 S 1.07

ST09 P 1.28

ST09 S 1.9

ST12 P 2.23

145

ST08 P 0.896

ST08 S 1.466

ST09 P 1.106

ST09 S 1.576

ST03 P 1.466

ST03 S 2.096

146

ST09 P 1.067

ST09 S 1.517

ST03 P 1.587

ST14 P 1.847

ST14 S 2.667

147

ST06 P 2.708

ST06 S 3.808

ST05 P 2.808

ST05 S 3.988

ST03 P 3.138

ST03 S 4.478

ST01 P 3.348

ST01 S 5.028

ST09 P 3.468

ST09 S 5.058

ST10 P 3.448

ST10 S 5.098

ST04 P 3.638

ST04 S 5.338

148

ST05 P 1.565

ST05 S 2.345

ST03 P 2.005

ST03 S 3.115

ST04 P 2.085

ST04 S 3.235

ST09 P 2.665

ST09 S 4.245

149

ST13 P 1.071

ST13 S 1.561

ST09 P 1.921

ST09 S 2.941

ST11 P 2.021

ST11 S 3.131

ST12 P 1.831

ST03 P 2.681

ST03 S 4.411

```
ST07 P 3.241
ST07 S 5.501
ST08 P 3.871
ST08 S 6.291
ST05 P 4.161
ST05 S 6.731
ST06 P 4.251
ST06 S 6.901
150
ST03 P 2.576
ST03 S 3.686
ST05 P 2.356
ST05 S 3.406
ST06 P 2.386
ST06 S 3.836
ST09 P 3.116
ST09 S 4.566
ST04 P 2.936
ST04 S 4.366
ST15 P 4.256
ST10 P 3.476
151
ST03 P 2.684
ST03 S 3.884
ST05 P 2.594
ST05 S 3.814
ST06 P 2.554
ST06 S 3.684
ST09 P 3.024
ST09 S 4.484
ST04 P 3.274
ST04 S 4.944
152
```

ST13 P 0.768

ST13 S 1.118

ST09 P 1.648

ST09 S 2.498

ST12 P 1.738

ST12 S 2.548

ST14 P 2.228

153

ST13 P 0.745

ST13 S 1.205

ST09 P 1.305

ST09 S 2.105

ST11 P 1.745

ST12 P 1.955

ST12 S 2.955

ST03 P 2.075

154

ST05 P 1.211

ST05 S 2.011

ST01 P 2.491

ST01 S 2.891

ST03 P 1.251

ST03 S 2.321

ST04 P 1.421

ST04 S 2.731

ST08 P 2.491

ST09 P 3.271

ST09 S 3.601

155

ST09 P 1.37

ST09 S 2.1

ST03 P 2.03

ST03 S 2.94

ST14 P 1.95

ST14 S 3.02

ST10 P 2.81

ST10 S 4.72

ST06 P 3.44

ST06 S 5.52

156

ST05 P 2.04

ST05 S 2.46

ST01 P 2.08

ST01 S 3.13

ST04 P 1.69

ST04 S 2.62

ST06 P 1.73

ST06 S 2.73

ST03 P 2.17

ST03 S 3.39

157

ST13 P 0.628

ST13 S 0.958

ST09 P 1.478

ST09 S 2.578

ST12 P 1.638

ST12 S 2.528

158

ST09 P 1.133

ST09 S 1.753

ST03 P 1.723

ST03 S 2.733

ST14 P 1.913

ST14 S 2.943

ST10 P 2.693

ST10 S 4.623

```
159
ST09 P 0.929
ST09 S 1.359
ST03 P 1.179
ST03 S 1.939
ST14 P 1.989
ST14 S 3.069
ST06 P 3.009
ST06 S 4.719
160
ST13 P 0.758
ST13 S 1.088
ST09 P 1.478
ST09 S 2.288
ST14 P 1.828
ST14 S 2.718
ST11 P 1.948
ST11 S 3.018
ST12 P 2.038
ST12 S 3.098
ST03 P 2.288
ST03 S 3.688
ST10 P 2.948
ST10 S 4.978
ST05 P 3.778
ST05 S 6.068
ST06 P 4.028
ST06 S 6.258
161
ST09 P 1.625
ST09 S 2.455
ST11 P 2.215
ST11 S 3.475
```

```
ST03 P 2.325
ST03 S 3.355
ST12 P 2.505
ST12 S 3.735
162
ST05 P 1.658
ST05 S 2.648
ST06 P 1.718
ST06 S 2.698
ST03 P 2.048
ST03 S 3.248
ST04 P 2.208
ST04 S 3.548
ST09 P 2.618
ST09 S 4.238
163
ST09 P 1.391
ST09 S 2.011
ST13 P 1.341
ST13 S 1.961
ST03 P 1.721
ST03 S 2.041
ST14 P 1.641
164
ST09 P 1.571
ST09 S 2.431
ST14 P 2.041
ST14 S 3.161
ST03 P 2.131
ST03 S 3.301
ST05 P 4.351
ST05 S 5.691
ST06 P 4.051
```

```
ST06 S 5.431
165
ST13 P 1.084
ST13 S 1.744
ST09 P 1.344
ST09 S 2.204
ST14 P 1.944
ST03 P 2.054
ST03 S 3.084
166
ST13 P 1.346
ST13 S 1.986
ST09 P 1.606
ST09 S 2.426
ST14 P 1.996
ST14 S 3.176
ST11 P 2.186
ST03 P 2.166
ST03 S 3.306
ST12 P 2.466
ST12 S 3.766
ST01 P 2.766
ST01 S 4.346
ST10 P 2.996
ST10 S 4.856
ST15 P 3.156
ST15 S 5.316
ST08 P 3.416
ST08 S 5.496
ST05 P 3.616
ST05 S 5.746
ST06 P 3.666
ST06 S 5.896
```

```
ST07 P 3.626
167
ST03 P 2.521
ST03 S 3.491
ST05 P 2.591
ST05 S 3.641
ST06 P 2.611
ST06 S 3.661
ST01 P 2.351
ST01 S 4.001
ST09 P 2.941
ST09 S 4.521
168
ST12 P 0.695
ST12 S 0.955
ST13 P 1.905
ST13 S 2.885
ST11 P 2.435
ST11 S 3.665
ST14 P 2.915
ST09 P 3.055
ST09 S 4.695
ST10 P 4.115
ST03 P 4.005
ST01 P 4.615
ST15 P 4.615
ST15 S 5.385
ST08 P 5.045
ST08 S 8.185
ST05 P 5.475
ST05 S 8.765
ST06 P 5.565
ST06 S 9.165
```

```
169
ST08 P 4.783
ST03 P 5.123
ST03 S 6.933
ST09 P 4.853
ST09 S 6.603
ST06 P 4.863
ST06 S 7.333
ST05 P 4.853
ST01 P 5.303
ST14 P 5.703
ST15 P 5.813
ST15 S 8.933
170
ST03 P 2.175
ST03 S 3.255
ST06 P 2.115
ST06 S 3.505
ST05 P 2.035
ST05 S 3.105
ST01 P 2.485
ST01 S 3.575
ST09 P 2.695
ST09 S 4.095
ST14 P 3.865
171
ST09 P 0.849
ST09 S 1.179
ST03 P 1.439
ST03 S 2.189
ST10 P 2.579
ST10 S 4.449
ST08 P 2.869
```

ST12 P 2.869

ST12 S 4.579

ST05 P 2.939

ST05 S 4.739

ST06 P 3.069

ST06 S 4.929

172

ST05 P 2.105

ST05 S 2.965

ST06 P 2.045

ST06 S 3.025

ST03 P 2.505

ST03 S 3.715